Optical Observations of Gravity Waves in the High-Latitude Thermosphere

M.A. de Deuge, B.Sc.(Hons)

A thesis for the degree of Master of Science

awarded 26.10.90

The Mawson Institute for Antarctic Research
University of Adelaide

June 1990

This thesis contains no material which has been accepted for the award of any other degree or diploma in any University. To the best of the author's knowledge and belief, it contains no material previously published or written by another person, except when due reference is made in the text. I consent to this thesis being made available for photocopying and loan by the librarian of the University of Adelaide, upon acceptance of the degree.

(M. A. de Deuge)

Acknowledgements

I would like to thank Dr. F. Jacka, Director of the Mawson Institute, for his ideas and guidance offered in the supervision of this work. D. Creighton provided valuable support and training on the operation and maintenance of equipment. Thanks are due also to Dr. B. Briggs, Dr. R. Vincent, and Dr. W. Hocking, of the Atmospheric Physics group, for their advice and constructive criticism of sections of this thesis. I am indebted to my fellow students of the Mawson Institute and Atmospheric Physics group for their many discussions and advice. Data were collected by B. Jarvis (1982), P. Wardill (1983), M. Conde (1984,1986), G. Price (1985), C. Evis (1988), and J. French (1989). Analysis providing gravity wave parameters from 1982-1986 and 1988 data was carried out by Dr. D.Y. Wang and Dr. P. Greet.

The assistance of the University of Adelaide in providing a short term scholarship for the latter part of this project is gratefully acknowledged.

I would like to thank the Australian Antarctic Division, which provided logistic support for this project. Thanks also to Dr. G. Burns, Upper Atmosphere Physics group, for his comments on sections of this thesis, and also for his dedication to the task of managing four Antarctic research laboratories.

Finally, special thanks to my dad, who has always given me unquestioning support.

Abstract

A three-field photometer was used to measure nighttime intensity variations in the $O(^1D)$ λ630 nm and $O(^1S)$ λ558 nm thermospheric emissions above Mawson, Antarctica (67.6°N, 62.9°E). Observations were made by the author in 1987; data from 1982 to 1989 were also examined.

Programs were developed to carry out cross-spectral analysis of the data in order to extract the frequency and horizontal trace velocity of periodic structures. Those satisfying certain criteria were attributed to propagating gravity waves. The parameters calculated for disturbances in the λ630 nm emission were characteristic of large-scale waves, and those for λ558 nm emission were characteristic of medium-scale waves. The results show distinct polarisation of the propagation azimuths. Waves in the λ630 nm emission propagated approximately north-westward throughout the period from 1982 to 1989. Those in the λ558 nm emission propagated approximately north-westward and south-eastward during 1982, 1983, 1988, and 1989, and approximately eastward during 1985, 1986, and 1987; in 1984 waves were polarised towards the northwest and northeast.

These results indicate that the observed propagation azimuths of waves in the λ558 nm emission may have a solar-cycle dependency which is not present in the λ630 nm observations. Directional wind filtering is found to be inadequate in accounting for the observations. It is suggested that waves observed in the λ630 nm emission were of predominantly auroral electrojet origin, whilst those observed in the λ558 nm emission were of both auroral and tropospheric origin. A tentative explanation of the changes in propagation azimuths is given in terms of variation in the height of the λ558 nm emission layer and the auroral electrojet region, with solar and geomagnetic activity.

Contents

Symbols

Chapter 2 symbols:

$\mathbf{B}$	=	magnetic field strength
c	=	speed of sound
$\mathbf{E}$	=	electric field strength
f	=	inertial frequency
g	=	acceleration due to gravity
h	=	Planck's constant
H	=	pressure scale height
H_c	=	pressure scale height of minor constituent
IBC	=	International Brightness Coefficient
$\mathbf{J}$	=	electric current density
k	=	Boltzmann's constant
$\mathbf{k}$	=	wave vector
$\hat{\mathbf{k}}$	=	unit wave vector
k_x, k_z	=	real wavenumbers, horizontal and vertical components
K_x, K_z	=	complex wavenumbers, horizontal and vertical components
m	=	mean molecular mass
MS, LS	=	medium-scale, large-scale
p	=	pressure
P, R, X, Z	=	complex polarisation amplitudes
R_i	=	Richardson number
$\mathbf{S}$	=	stress tensor
t	=	time
T	=	temperature
T_E	=	rotation period of earth
TID	=	travelling ionospheric disturbance
U	=	mean wind speed
$\mathbf{U}$	=	(u, v, w) = mean wind velocity, also written $\bar{u}$
v_{px}, v_{pz}	=	horizontal and vertical trace velocities
$\mathbf{v}$	=	velocity
$\mathbf{v_p}$	=	phase velocity
x, z	=	horizontal and vertical cartesian components

When symbols are dashed, a perturbation value is implied; when subscript 0 is used, background values are implied.

Chapter 2 symbols continued...

α	=	temperature lapse rate
α^*	=	adiabatic temperature lapse rate
γ	=	ratio of specific heat capacities, C_p/C_v
λ	=	true wavelength
λ_x, λ_z	=	horizontal and vertical trace wavelength
μ	=	coefficient of molecular viscosity
η	=	kinematic viscosity, $\frac{\mu}{\rho}$
ν_{ni}	=	neutral-ion collision frequency
ν_{558}	=	frequency of electromagnetic radiation
ρ	=	density
τ	=	wave period
τ_a	=	acoustic cutoff period
τ_b	=	Brunt-Väisälä period
τ_i	=	inertial period
ω	=	ground-based angular frequency
ω_a	=	acoustic cutoff frequency
ω_b	=	Brunt-Väisälä frequency
Ω	=	intrinsic frequency
ϕ	=	latitude
ψ	=	angle between mean wind and horizontal wave vector
Φ	=	elevation angle of energy propagation

Chapter 3 symbols:

$A(m)$	=	Airy function
d	=	diameter of field stops
D	=	diameter of fields at emission height
l	=	focal length of telecentric lens
L	=	emission height
m	=	order of interference
r	=	distance between centre of field stop and optical axis
$\mathcal{R}$	=	reflectance at plate surface
S	=	separation of fields at emission height
$\mathcal{T}$	=	transmittance at plate surface
t	=	geometric separation of reflecting surfaces
t_e	=	effective thickness of spacer
θ	=	angle of incidence of rays between etalon plates
θ'	=	angle of incidence of rays at filter surface; tilt angle
Θ	=	zenith angle of centre of field stop
λ	=	vacuum wavelength
λ_m	=	wavelength transmitted at order m
ϕ	=	phase change upon reflection at plate surfaces
Φ	=	field of view
μ	=	refractive index of spacer medium
μ_e	=	effective refractive index from air to spacer medium

Chapter 4 symbols:

$G_{mn}(f)$	=	cross-power spectrum
$C_{mn}(f)$	=	cospectrum spectrum
$Q_{mn}(f)$	=	quadrature spectrum
$A_{mn}(f)$	=	cross-amplitude spectrum
$\Phi_{mn}(f)$	=	phase spectrum
$K_{mn}(f)$	=	coherency spectrum
$\tau_{mn}(f_i)$	=	time difference between fields
$v_{mn}(f_i)$	=	apparent speed from field m to n
a, b	=	coefficients defining line of best fit
f	=	frequency
f_i	=	discrete frequency components
S	=	separation of fields at emission height
t	=	time
T	=	record length
$\mathbf{v}$	=	horizontal trace velocity
v	=	horizontal trace speed
$x_m(t)$	=	continuous finite time series, m
$X_m(f)$	=	$a_m(f) - ib_m(f)$ = Fourier transform of $x_m(t)$
θ	=	azimuth of wave propagation
ν	=	degrees of freedom
$\sigma^2()$	=	variance of a parameter
τ	=	time lag

Chapter 1

Introduction

In order to put the subject of this work in context, a very brief discussion is given on the structure of the atmosphere and the role of gravity waves within it. The atmosphere may be studied in terms of its composition, dynamics, or energetics, which are coupled through the conservation laws of mass, momentum, and energy. Although these conservation laws apply throughout the atmosphere, there is large variation in the processes occurring at different altitudes. The atmosphere may be classified into regions - the troposphere, stratosphere, mesosphere, thermosphere, and exosphere - defined according to the vertical temperature gradient (figure 1.1). The major energy source for the atmosphere is absorption of solar radiation. In the upper atmosphere the UV component produces a range of photoionisation, photodissociation, and photoexcitation reactions. A consequence of photoionisation is the presence of an ionosphere above about 60 km, which is the maximum depth of penetration of most ionising radiation.

Adjacent regions of the atmosphere interact energetically, dynamically, and chemically. Energy and momentum is redistributed both vertically and latitudinally. One of the important means of redistribution is through the generation, propagation, dissipation, and breaking of atmospheric waves. Waves occur at all altitudes and range (for example) from acoustic waves (with periods 50 μs - 1 min), gravity waves (5 min - 24 h), tides (8, 12, 24 h), to planetary waves (periods >1 day). This study concentrates on gravity waves, in which gravity (or more correctly, buoyancy) is the restoring force of the wave motion.

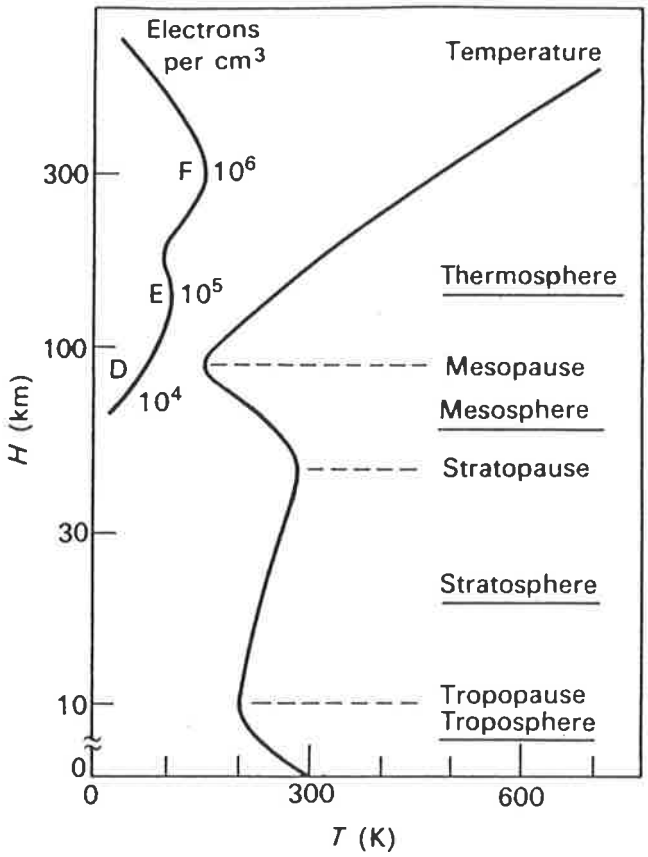

Figure 1.1. Vertical profile of the atmosphere showing regions classified according to temperature gradient and ionisation density (from McEwan and Phillips, 1975).

At mid and low latitudes, gravity-wave morphology has been well documented, and work is ongoing in the area of energy and momentum transport by waves in the lower and middle atmosphere. Measurements from high latitudes, especially high southern latitudes, are less common due to the scarcity of observing sites. High-latitude observations are of great interest because of the energy generated in the auroral zones through Joule heating in the auroral electrojet and particle precipitation. Although this is a localised source, during times of high solar activity its energy input may equal that due to solar heating in the upper atmosphere. Far-propagating thermospheric gravity waves act to transport some of this energy to lower latitudes.

The aim of this study is to carry out statistical analyses of wave characteristics near this source region, at Mawson, Antarctica (67.6°S, 62.9°E). Two particular properties of the thermosphere can be exploited in order to observe thermospheric waves. The first is the presence of the ionosphere; the ion and electron density perturbations produced by wave motion can be detected in radio waves reflected from the ionosphere. The second

property, used in this study, is the emission of visible electromagnetic radiation by atmospheric atoms and molecules, resulting in the phenomena of airglow and aurora. A gravity wave propagating through an emission layer perturbs the density of the emitting species and hence the emission intensity. Certain wave parameters can be determined from measurements of these perturbations. Atmospheric emissions have also been used as a means of remotely studying temperature, winds and composition.

This presentation has the following structure. Chapter 2 outlines the history and theory of gravity waves in a realistic atmosphere, with some discussion on gravity-wave sources and propagation effects. The last section in this chapter deals with atmospheric emissions, particularly the atomic oxygen λ630 nm and λ558 nm lines observed in this study. The influence of gravity waves on these emissions is discussed. Chapter 3 presents the photometer system used to measure emission intensities. General layout, observing procedure, and calibration technique and results are discussed. Chapter 4 describes the analysis applied to the photometer data. Cross-spectral analysis was used to analyse frequency components of the gravity-wave field. In chapter 5 the results of these analyses are presented, with discussion on possible interpretations of the results in Chapter 6. Chapter 7 summarises the results and conclusions drawn from the study, and suggests possible extensions of the work.

Chapter 2

Atmospheric Gravity Waves

2.1 History of Theory and Observations

Gravity waves in the lower atmosphere were first recognised as such from observations of banded cloud formations in the lee of mountain ranges and later from pressure fluctuations associated with weather fronts, squall lines, land-sea breeze reversals and local convective activity. Wave processes at ionospheric levels were observed as periodically fading signals by early radio communicators. This was attributed to 'travelling ionospheric disturbances' (TIDs) by Munro (1948, 1950) and Beynon (1948) who measured TIDs in the F region of the ionosphere, with periods of 10 to 60 min, horizontal speeds of 80 to 170 ms^{-1} and apparent downward vertical speeds of around half the horizontal speeds. Munro (1958) reported diurnal and seasonal variations in the speed, direction, and frequency of occurrence of TIDs. From around 80 to 115 km, vertical wind profiles obtained from photographs and radio echo observations of meteor trails showed irregularities with a vertical scale of about 6 km and a horizontal scale of 150 km (Liller and Whipple, 1954; Greenhow and Neufeld, 1959). Wind shears of up to 50 ms^{-1} km^{-1} were observed.

To explain observations of travelling disturbances, Martyn (1950) proposed a theory based on rotational cellular waves in the atmosphere. Later, Hines (1955) explained some characteristics of TIDs in terms of hydromagnetic resonance. However, these were found to be unsatisfactory and it was not until 1960 that a comprehensive theory ac-

counting for most of the small-scale periodic motions in the atmosphere was proposed by Hines (1959, 1960). He described the features observed in meteor trails and TIDs as manifestations of internal atmospheric waves governed by gravitational and compressional forces. Hines suggested that gravity waves are produced in the troposphere and propagate their energy obliquely upwards. He described how wave amplitude grows exponentially with height and how propagation of gravity waves is affected by reflection, intermodulation, and dissipation. This results in a progressively-filtered wave spectrum, producing different wave characteristics at different heights. The effects of dissipation through viscous damping and thermal conduction were discussed further by Pitteway and Hines (1963).

Throughout the late 1950's and beyond, new techniques were developed to study atmospheric wave motions. For example, Witt (1962) analysed photographs of noctilucent clouds at altitudes around 85 km which showed systems of waves with wavelengths of 50 km, displacement amplitudes of 4 km and propagation velocities between 10 and 20 ms^{-1}. Visible gas trails released from rockets at 70-200 km altitude were studied in order to separate gravity-wave motions from mean and tidal motions (Manring et al., 1959; Kochanski, 1964; Rosenberg and Edwards, 1964). Zimmermann and Champion (1963) used chemical clouds to study turbulent motion at around 100 km. A CW Doppler sounder was used by Georges (1967a) to measure vertical ionospheric motions and to determine their frequency spectra. He found that a narrow band of frequencies occurred at each height and the dominant period increased with height, which implied that shorter-period waves were more severely attenuated. Using ionosonde traces, Heisler (1958) measured large disturbances in ion density which he attributed to TIDs. Combining data from an array of stations around Australia, Heisler measured wave fronts with horizontal extent of up to 1000 km, travelling distances of at least 3000 km. Investigations by Davis and daRosa (1969) using satellite signals to detect fluctuations in columnar electron content suggested that large-scale TIDs are generated by polar substorms.

During this time, studies were made into the effect of gravity waves on the energy transport and large-scale circulation in the atmosphere. Gossard (1962) analysed tro-

pospheric waves to determine energy density spectra and vertical energy flux into the lower ionosphere. He found significant energy flux due to waves of periods 10 min to 2 h.

Theoretical studies investigated the limiting effects of reflection and viscous dissipation on wave-amplitude growth (eg. Midgley and Liemohn, 1966). Bretherton (1966) and Booker and Bretherton (1967) described another growth-limiting mechanism. They showed that if a wave propagates into a region where the local mean wind velocity is equal to the horizontal phase trace velocity of a wave, the intrinsic wave frequency is Doppler shifted to zero, the wave breaks and its momentum is transferred to the mean flow. The height at which this occurs is called a critical level. Some consequences of critical levels were discussed by Hines (1968). A further major mechanism limiting gravity-wave growth was discussed by Hodges (1967). He described how density and temperature fluctuations caused by a wave may become large enough to produce convective instabilities, which results in breaking of the wave and turbulence.

Although these mechanisms of wave dissipation had been investigated and modelled by the 1970's, it was almost a decade later that their importance in the dynamics and thermal structure of the middle atmosphere was fully realized. Wave breaking and energy-momentum transport are still under detailed investigation.

Another active area of gravity-wave research is the identification of generation mechanisms and source regions, especially with respect to high-latitude sources. These topics, and the basic gravity-wave theory on which they are based, will now be discussed in more detail.

2.2 Gravity Wave Theory

The following mathematical theory for describing gravity waves is based on hydrodynamic equations for a flat stationary atmosphere. Strictly speaking, a general theory for

atmospheric waves using spherical coordinates in a rotating frame of reference should be used, and gravity waves considered as a limiting case. However, this method involves considerable difficulty in solving the equations of motion, and as the simpler model has been successfully used to account for many observed motions, it is adopted for this discussion. An outline is given below, based on more detailed descriptions in Gossard and Hooke (1975) and Hines et al. (1974).

2.2.1 Structure of the atmosphere

In the absence of wave motion, the structure of the atmosphere is determined by a balance between the vertical pressure-gradient force and gravity, as expressed in the hydrostatic equation. The steady-state solution gives the following pressure and density profiles:

$$p(z) = p_0 \exp\left(-\int_0^z \frac{1}{H} dz\right) \tag{2.1}$$

$$\rho(z) = \rho_0 \exp\left(-\int_0^z \frac{1+H'}{H} dz\right) \tag{2.2}$$

where z = height

p_0, ρ_0 = pressure and density at $z = 0$

H = pressure scale height $= kT/mg = c^2/\gamma g$

H' = $\partial H/\partial z$

k = Boltzmann's constant

T = temperature

m = mean molecular mass

c = speed of sound

γ = ratio of specific heat capacities, C_p/C_v

= 1.4 for diatomic gas

= 1.67 for monatomic gas

$$g = \text{acceleration due to gravity}$$

In an isothermal atmosphere $H' = 0$ and equations (2.1) and (2.2) become

$$p(z) = p_0 \exp\left(-\frac{z}{H}\right) \tag{2.3}$$

$$\rho(z) = \rho_0 \exp\left(-\frac{z}{H}\right) \tag{2.4}$$

In general the atmosphere is non-isothermal and a constant temperature gradient will be assumed, ie. $T(z) = T_0 - \alpha z$, where T_0 is the temperature at $z = 0$ and α is the temperature lapse rate, $-\frac{dT}{dz}$. A well-mixed adiabatic atmosphere has a lapse rate of $\alpha^* = 9.8$ K km^{-1}. In an atmosphere with a lapse rate less than 9.8 K km^{-1}, an air parcel which is upwardly displaced will expand adiabatically, becoming colder and denser than the surrounding air, and then sink back to its original position. Therefore the atmosphere is stable to such small disturbances. In an atmosphere with a temperature gradient of more than 9.8 K km^{-1}, the parcel will continue to rise, and the atmosphere is unstable. The natural oscillation of such an air parcel in a stable atmosphere is governed by a balance between the buoyancy and the inertial forces acting on the parcel. It can be shown that a harmonic oscillation is set up at the Brunt-Väisälä (or buoyancy) frequency

$$\omega_b^2 = \frac{g}{T}(\alpha^* - \alpha) \tag{2.5}$$

$$= (\gamma - 1)\frac{g^2}{c^2} + \frac{g}{T}\frac{\partial T}{\partial z}$$

2.2.2 Equations of atmospheric fluid motion

Having established the conditions of the local stationary atmosphere, a fluid dynamical approach is used to describe motions of the atmosphere in terms of fluid velocity $\mathbf{v}$, temperature T, pressure p, and density ρ. Fluid motion is governed by the conservation of mass, momentum and energy, as expressed in the equations of continuity, force, and energy, as follows,

Equation of continuity:

$$\frac{D\rho}{Dt} + \rho\nabla\cdot\mathbf{v} = 0 \tag{2.6}$$

where $\frac{D}{Dt} = \frac{\partial}{\partial t} + \mathbf{v}\cdot\nabla$ is the Stokes derivative, the time derivative following the motion of the fluid.

Equation of force:

$$\frac{D\mathbf{v}}{Dt} = -\frac{1}{\rho}\nabla p + \mathbf{g} + \mathbf{F} \tag{2.7}$$

where $-\frac{1}{\rho}\nabla p$ = force due to pressure gradient

$\mathbf{g}$ = force due to gravity, plus centripetal force

$\mathbf{F}(\mathbf{r},t)$ = source terms representing force per unit mass

$\mathbf{F}(\mathbf{r},t)$ may include terms for the Coriolis force, molecular viscosity forces, and Lorentz forces. The relative importance of each of these terms is dependent on the frequency and dimensions of the waves under consideration.

Equation of energy:

$$C_v \frac{DT}{Dt} + p \frac{D}{Dt}\left(\frac{1}{\rho}\right) = Q(\mathbf{r},t) \tag{2.8}$$

where $C_v \frac{DT}{Dt}$ = rate of internal heating

$p \frac{D}{Dt}\left(\frac{1}{\rho}\right)$ = work done by pressure

$Q(\mathbf{r},t)$ = source term representing heating rate per unit mass

$Q(\mathbf{r},t)$ may include terms for radiative heat gain or loss, viscous heat dissipation, heat loss due to thermal conduction, and Joule heating.

Volland (1969) incorporated the various source terms in his derivation of the equations governing gravity waves; however, the simplified atmospheric model of Hines (1960) is adopted here. This assumes an isothermal atmosphere of uniform composition and constant gravitational field. It also assumes the atmosphere to be non-viscous, to have no thermal conduction and to be electrically neutral. The effects of introducing a mean wind flow, a temperature gradient and viscous dissipation will be discussed later. An inertial frame of reference is assumed; a rotating frame introduces a Coriolis force ($-2\rho\mathbf{w}\times\mathbf{v}$, where $\mathbf{w}$ is the angular velocity of rotation) which acts at right angles to

the motion of the gas, but becomes significant only for long periods and distances, as in tides and planetary waves. Under these assumptions, the equations of motion become somewhat simpler. Using the perfect gas equation, the energy equation is rewritten as the adiabatic equation of state. Equations (2.6), (2.7), and (2.8) become,

Equation of continuity:

$$\frac{D\rho}{Dt} + \rho\nabla\cdot\mathbf{v} = 0 \tag{2.9}$$

Equation of force:

$$\rho\frac{D\mathbf{v}}{Dt} + \nabla p - \rho\mathbf{g} = 0 \tag{2.10}$$

Equation of energy:

$$\frac{Dp}{Dt} - c^2\frac{D\rho}{Dt} = 0 \tag{2.11}$$

The equations of motion are non-linear in ρ, p and $\mathbf{v}$, and difficult to solve analytically. They can be linearized by writing the parameters as a zeroth order (background) term plus a small first order (perturbation) term, ie. $\rho = \rho_0 + \rho'$, $p = p_0 + p'$, $\mathbf{v} = \mathbf{v_0} + \mathbf{v}'$. When substituted into the equations of motion the zeroth order terms describe the movements of the background atmosphere, the first order (dashed) terms describe the perturbation motions and higher order terms may be neglected. It is assumed the perturbation parameters vary sinusoidally, ie.

$$\frac{p'}{p_0 P} = \frac{\rho'}{\rho_0 R} = \frac{v_x'}{X} = \frac{v_z'}{Z} = A \exp\, i(\omega t - K_x x - K_z z) \tag{2.12}$$

where x, z are cartesian coordinates (z is vertical and x is measured in any horizontal direction), K_x, K_z are (theoretically) complex wavenumbers and P, R, X, Z are the complex polarisation amplitudes which define the phase relationships between the parameters.

Substituting (2.12) into the linearized forms of equations (2.9), (2.10), and (2.11) gives four linear equations in the four variables, $\frac{p'}{p_0}$, $\frac{\rho'}{\rho_0}$, v_x' and v_z'. These are written in matrix form, and a nontrivial solution can be found, providing the determinant of the coefficient matrix is zero. This condition defines a relationship between K_x, K_z, and ω, in which it is impossible for both K_x and K_z to be purely real. A simple and realistic possibility is to choose K_x to be real, which implies no exponential growth or decay

of the wave in the horizontal direction. In this case, either K_z is purely imaginary or $K_z = k_z + \frac{i}{2H}$. If K_z is purely imaginary the wave can have no vertical phase progression, but has vertical exponential growth or decay. This is the case for surface waves or evanescent waves. If K_z is complex, the wave has vertical phase progression and exponential growth with height. This is the case for internal waves, which are to be considered further. Exponential growth of the wave results from the exponential decrease in atmospheric density with height; for the wave to maintain a constant energy flux, there must be a corresponding increase in the amplitude of wave fluctuations.

With $K_x = k_x$ and $K_z = k_z + \frac{i}{2H}$, the relationship between k_x, k_z, and ω is described by the dispersion equation,

$$k_z^2 = k_x^2 \frac{(\omega_b^2 - \omega^2)}{\omega^2} - \frac{(\omega_a^2 - \omega^2)}{c^2} \tag{2.13}$$

where ω_b is the Brunt-Väisälä frequency, ω_a is a constant called the acoustic cutoff frequency, and $\omega_b < \omega_a$. There is no real solution to the dispersion equation if ω is in the interval $\omega_b < \omega < \omega_a$, so that no internal waves propagate at these frequencies. Waves will propagate when $\omega < \omega_b$ which is the gravity wave region, and when $\omega > \omega_a$ which is the acoustic wave region. If the term for the Coriolis effect had been retained in the equation of force then the dispersion relation would show a low frequency limit for the gravity wave region, given by the inertial frequency, f. Expressions for these limiting frequencies and their corresponding periods are given by

$$\begin{aligned} \omega_a^2 &= \left(\tfrac{\gamma g}{2c}\right)^2 + \tfrac{\gamma g}{2T}\tfrac{\partial T}{\partial z} && \tau_a < 5 \text{ min} \\ \omega_b^2 &= (\gamma - 1)\tfrac{g^2}{c^2} + \tfrac{g}{T}\tfrac{\partial T}{\partial z} && \tau_b \sim 5 - 15 \text{ min} \\ f &= \tfrac{4\pi \sin\phi}{T_E} && \tau_i \sim 13 \text{ h} \end{aligned} \tag{2.14}$$

where ϕ is the latitude, T_E is the rotation period of the earth, and τ_i is given for latitude $\phi = 67°$.

The relationship (2.13) can be represented on a dispersion diagram showing contours of constant frequency in the k_x, k_z domain (figure 2.1). The elliptical contours represent the acoustic branch and the hyperbolic contours represent the gravity wave branch. A large range of horizontal and vertical scales are possible. Reid (1986) collated 408 optical and radar observations of gravity wave characteristics in the 60-110 km altitude

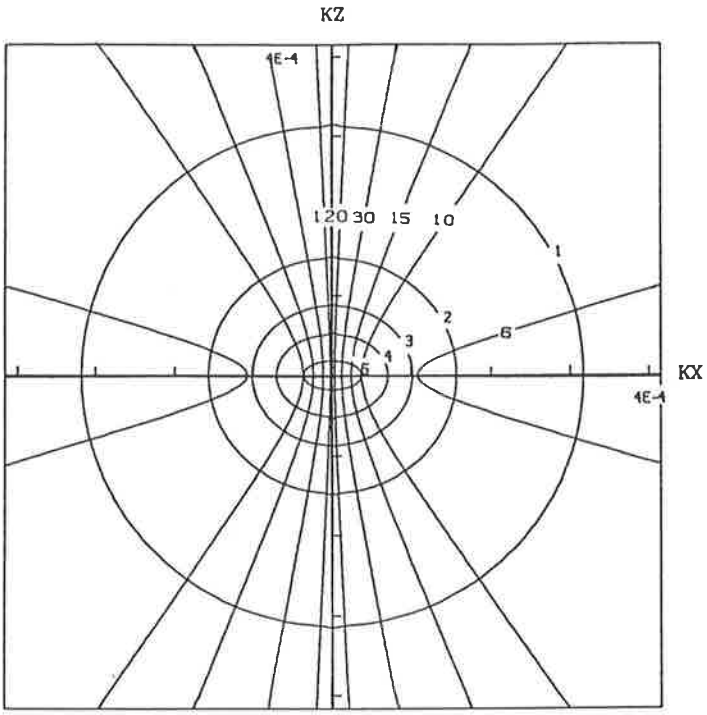

Figure 2.1. Dispersion diagram showing contours of constant frequency in the $k_x \sim k_z$ domain.
The elliptical contours represent the acoustic branch and the hyperbolic contours represent the gravity wave branch. The contours are labelled with period, in minutes. They are calculated using parameters appropriate to a height of 120 km, ie. τ_b=5.8 min, τ_a=5.2 min, c=329 ms^{-1}.

range. Observed periods ranged from 8 min to 10 h, with horizontal wavelengths of 10-6000 km, and phase speeds of 5-380 ms^{-1}. Equation (2.13) indicates that a particular period may correspond to a range of possible horizontal wavelengths; data collated by Reid (1986) shows, in broad features, a power law relationship, $\lambda_x = 3.6\ T^{1.06}$ ie. a general increase in horizontal wavelength with period.

2.2.3 Propagation velocities of a wave

The phase velocity of a wave, in the (x, z) plane, is given by

$$\mathbf{v_p} = \frac{\omega}{(k_x^2 + k_z^2)^{\frac{1}{2}}}\ \hat{\mathbf{k}} \tag{2.15}$$

where the unit vector $\hat{\mathbf{k}}$ is in the direction of phase progression. The cartesian components of $\mathbf{v_p}$ are not measured by observation; the observed quantities are the phase trace speeds, which are the speeds with which wavefronts appear to move in the x and

z directions. The horizontal and vertical phase trace speeds are

$$v_{px} = \frac{\omega}{k_x}, \qquad v_{pz} = \frac{\omega}{k_z} \qquad \text{where} \quad \frac{1}{|\mathbf{v_p}|^2} = \frac{1}{v_{px}^2} + \frac{1}{v_{pz}^2} \tag{2.16}$$

Similarly, the true wavelength as measured in the (x, z) plane is

$$\lambda = \frac{2\pi}{(k_x^2 + k_z^2)^{\frac{1}{2}}} \tag{2.17}$$

The observed quantities are

$$\lambda_x = \frac{2\pi}{k_x}, \qquad \lambda_z = \frac{2\pi}{k_z} \qquad \text{where} \quad \frac{1}{\lambda^2} = \frac{1}{\lambda_x^2} + \frac{1}{\lambda_z^2} \tag{2.18}$$

Strictly monochromatic waves do not occur in the atmosphere; a superposition of waves having a range of frequencies and wave vectors about central values, is always present. These form a wave packet which travels with x and z group velocity components given by

$$\left(\frac{\partial \omega}{\partial k_x}\right)_{k_z} \qquad \text{and} \qquad \left(\frac{\partial \omega}{\partial k_z}\right)_{k_x} \tag{2.19}$$

Therefore the motion of the wave packet, and hence energy propagation, is at an elevation angle given by

$$\tan \Phi = \left(\frac{\partial \omega}{\partial k_z}\right)_{k_x} \Big/ \left(\frac{\partial \omega}{\partial k_x}\right)_{k_z} = -\left(\frac{\partial k_x}{\partial k_z}\right)_{\omega} \tag{2.20}$$

which is normal to the ω contour. The locus of the wave packet is referred to as the ray path.

Propagation properties of both branches of internal atmospheric waves can be deduced from figure 2.1. This shows that for acoustic waves, $\mathbf{k}$ can take any direction at any frequency, and the direction of energy propagation is approximately in the same direction as that of phase progression. When $\omega >> \omega_a$ equation (2.13) becomes the wave equation for sound, ie. $\omega^2 = c^2(k_x^2 + k_z^2)$. Propagation of gravity waves however, is highly anisotropic which is to be expected as the gravitational restoring force acts only in the vertical direction. Consideration of figure 2.1 shows that the directions of phase progression and energy propagation are up to 90° apart in the (x, z) plane; although the horizontal components are in the same direction, the vertical components are always oppositely directed. Therefore if the energy of a gravity wave is propagating upwards,

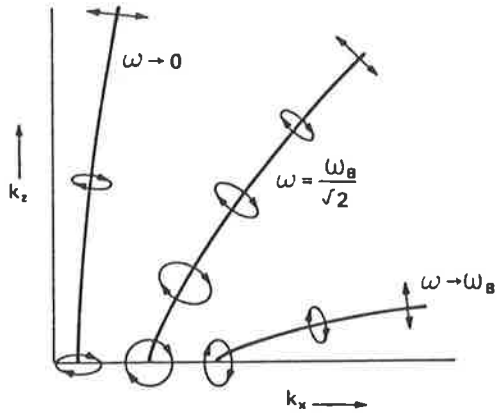

Figure 2.2. Air parcel orbits produced by gravity waves. The orbits are elliptical, tending to linear oscillations for large values of **k**, ie. for short wavelengths (from Georges, 1967b, referred to in Beer, 1974).

the observed phase progression is downwards. Figure 2.1 shows that as $\omega \rightarrow 0$, phase progression is predominantly vertical and energy propagation horizontal. As $\omega \rightarrow \omega_b$, phase progression tends towards horizontal whilst energy propagation tends towards vertical.

The magnitude of phase and group velocities is also dependent on frequency. For waves in the acoustic branch, phase speed is always equal to or greater than c, the speed of sound, increasing hyperbolically as ω approaches ω_a. For waves in the gravity wave branch, phase speed is always less than c. The group speed of waves in both branches is always less than c.

2.2.4 Perturbation velocities

Motion of an individual air parcel can be described using the polarisation amplitudes, X and Z, which define the phase relationship between the perturbation velocity components, v_x' and v_z', and hence the displacement of the air parcel. Figure 2.2 shows the orbits of air parcels as ellipses at gravity wave frequencies. For large **k** (ie. short wavelengths) the motion becomes purely linear. As $\omega \rightarrow 0$ the major axis of the orbit

tends towards horizontal; as $\omega \rightarrow \omega_b$ it tends towards vertical.

2.3 Effects of a Real Atmosphere

The discussion so far has concentrated on gravity waves in an idealised fluid. In a realistic atmosphere the presence of a background wind, temperature gradients, viscosity, thermal conduction, ions, and the process of wave breaking all affect gravity wave characteristics.

2.3.1 Effects of mean wind and critical layers

The assumption of a stationary atmosphere is dropped and a mean wind, $\mathbf{U} = (u, v, w)$, is included in the equations of motion. When applied to the general wave solution as before, the Stokes derivative becomes

$$\frac{D}{Dt} = \frac{\partial}{\partial t} + u\frac{\partial}{\partial x} + v\frac{\partial}{\partial y} + w\frac{\partial}{\partial z} \tag{2.21}$$

Using this operator, solution of the perturbation matrix gives rise to a dispersion relation as before, but ω is replaced by the intrinsic frequency, $\Omega = \omega - \mathbf{U} \cdot \mathbf{k}$,

$$k_z^2 = k_x^2\frac{(\omega_b^2 - \Omega^2)}{\Omega^2} - \frac{(\omega_a^2 - \Omega^2)}{c^2} \tag{2.22}$$

The frequency as seen by a fixed observer is ω, whereas Ω is the Doppler shifted frequency as seen in the frame moving with the wind. Ω is the quantity which applies to the physical behaviour of the wave. Generally the magnitude of the vertical component of the mean wind is negligible compared with that of the horizontal component, so that the intrinsic frequency becomes

$$\Omega = \omega - U\ k_x\ \cos\psi \tag{2.23}$$

where U is the mean wind speed and ψ is the angle between the wind direction and the horizontal wave vector. The intrinsic phase trace speed is

$$\frac{\Omega}{k_x} = v_{px} - U \cos\psi \tag{2.24}$$

If $\psi > 90°$, the intrinsic frequency is Doppler shifted to a higher frequency. As the wave continues to propagate upwards into regions of increasing mean wind, Ω increases and the ray path is refracted towards the vertical (Cowling et al., 1971). The wave is reflected when Ω becomes equal to the Brunt-Väisälä frequency.

If $\psi < 90°$, the intrinsic frequency is Doppler shifted to a lower frequency. As the wave propagates through regions of increasing mean wind, Ω tends to zero, and the ray path is refracted towards the horizontal. Equation (2.24) shows that if the component of the mean wind in the direction of phase progression is equal to the horizontal trace speed, then $\Omega = 0$. In this case the wave becomes unstable, begins breaking, and wave energy is transferred to the background mean wind. This coupling between gravity waves and the mean wind is the critical level effect mentioned in section 2.1. It has two effects on the dynamics of the atmosphere. The first is the filtering out of waves with low phase speed (ie. short horizontal wavelengths). Since most critical level filtering occurs in a direction parallel (or close) to the mean wind, the observed effect is a predominance of waves perpendicular to the mean wind (reflection reduces the number of waves propagating antiparallel to the mean wind). The second effect is transport of energy and momentum in the middle atmosphere, through dissipation of gravity waves.

The mechanisms of critical coupling and reflection were clearly illustrated by the laboratory studies of Koop (1981) and Koop and McGee (1986) who obtained shadowgraph images of internal waves propagating in stratified fluids.

2.3.2 Temperature gradients and reflection

Hines' (1960) model assumes an isothermal atmosphere; the real atmosphere contains temperature gradients and wind shears which have a significant effect on wave propa-

gation (Pitteway and Hines,1965). Vertical gradients in temperature and wind change the Brunt-Väisälä frequency and intrinsic wave frequency, which causes refraction of the wave ray path. It can be shown (eg. Lighthill, 1978, p334) that the elevation angle of the ray path is given by

$$\sin\Phi = \frac{\omega - k_x\, U(z)\, \cos\psi}{\omega_b(z)} = \frac{\Omega(z)}{\omega_b(z)} \tag{2.25}$$

where $\omega_b(z)$ = height-dependent Brunt-Väisälä frequency

$\Omega(z)$ = height-dependent intrinsic frequency

$U(z)$ = height-dependent mean wind speed

The previous section described the refraction effects of wind shears. Temperature gradients cause changes in the speed of sound and hence ω_b. If ω_b decreases with height, the ray path is refracted towards the vertical, until the wave is reflected when $\Omega = \omega_b$.

In general, reflection occurs when a wave propagates from a height where $k_z^2 > 0$ to a height where $k_z^2 \leq 0$. If this condition persists for more than half a wavelength the wave is reflected. From the dispersion equation (2.22), $k_z^2 \leq 0$ when $k_x^2 \leq \frac{\Omega^2}{c^2}\left(\frac{\omega_a^2-\Omega^2}{\omega_b^2-\Omega^2}\right)$. At low frequencies this is equivalent to the condition $\frac{\Omega}{k_x} \geq \frac{c\omega_b}{\omega_a}$. Hines (1960) applied this condition to the height range of 50-80 km, being a region of large temperature gradient in the middle atmosphere. He quoted from Minzer et al. (1959) the minimum value of $\frac{c\omega_b}{\omega_a}$ to be 170 ms^{-1} at 79 km altitude. A more recent global atmospheric model by Groves (1985, 1987) was used to calculate the minimum value appropriate to the latitude of Mawson, and averaged over the observing months, March to October. This was approximately 230 ms^{-1} at 85 km. Therefore low frequency waves with horizontal trace velocities greater than 230 ms^{-1}, propagating upwards from the troposphere, will theoretically be reflected at this level. In practise, this depends on the vertical extent of the strong temperature gradient relative to the scale of the wave. The limit imposed by reflection on upwardly propagating gravity waves is shown as a dotted curve on the dispersion diagram of figure 2.3. Permitted gravity wave modes (of tropospheric origin) lie above this curve.

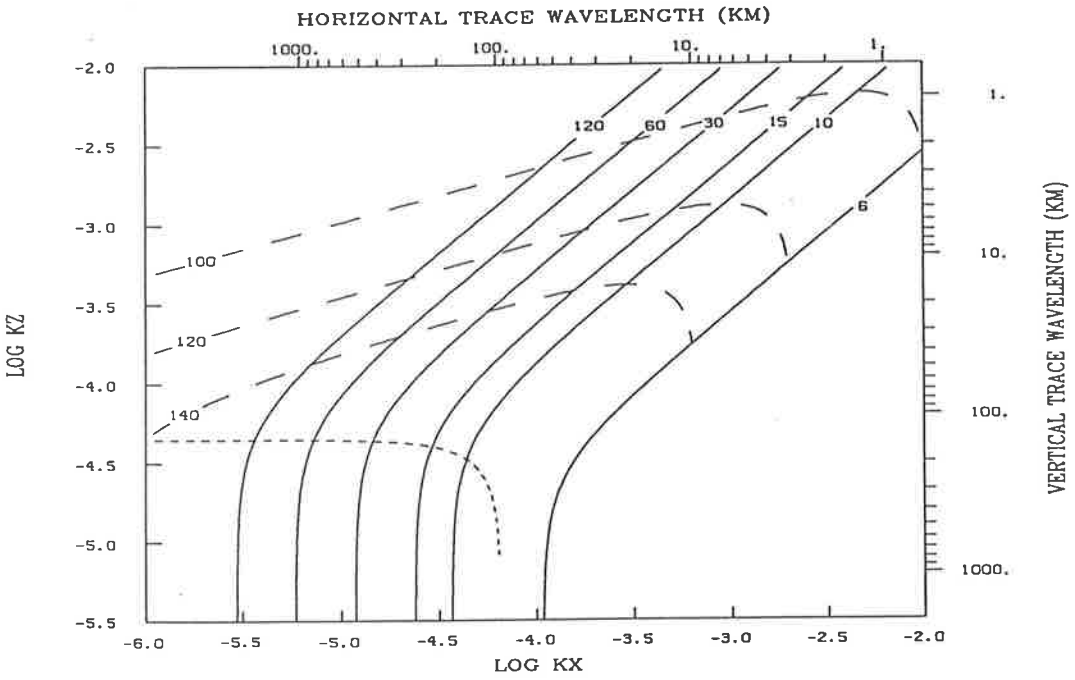

Figure 2.3. Dispersion diagram showing the reflection limit (dotted line) and dissipation limits (dashed lines) using a logarithmic scale. Permitted wave modes fall between these limits. Solid lines are contours of constant period, marked in minutes. The reflection limit defines upwardly propagating waves which are reflected in the mesosphere. Viscous dissipation limits define waves which are significantly dissipated in the thermosphere; these are shown for a range of altitudes near the λ558 nm emission. Horizontal and vertical trace wavelengths are marked.

2.3.3 Viscosity and thermal conduction

In the model described, an upwardly-propagating wave which suffers no critical layer absorption or reflection will grow exponentially. Various phenomena act to limit this growth, including viscous and thermal dissipation of momentum and heat.

For a fluid with non-constant velocity and velocity shears, the drag force per unit volume due to molecular viscosity is given by $\nabla \cdot \mathbf{S} = \frac{\mu}{3}\nabla(\nabla \cdot \mathbf{v}) + \mu\nabla^2\mathbf{v}$ where $\mathbf{S}$ is the stress tensor and μ is the (constant) molecular coefficient of viscosity. This term can be included in the equation of motion, and a corresponding term, $\nabla \cdot (\mathbf{S} \cdot \mathbf{v}) - \mathbf{v} \cdot (\nabla \cdot \mathbf{S})$, in the equation of energy, but the solution of the equations becomes complicated (Pitteway and Hines, 1963). An estimate of the damping effect of viscosity can be obtained by equating the mean energy content in one cycle of undamped wave motion with the amount of energy the atmosphere can absorb through viscous dissipation. This condition occurs when

$$\bar{E} = \bar{R}\tau \tag{2.26}$$

where $\bar{E}$ = mean energy content in one cycle of wave motion

$\bar{R}$ = rate of viscous energy dissipation

τ = wave period

Hines (1960) used the expression for $\bar{R}$ given by Lamb (1945) and the asymptotic approximation $k_z^2 >> (\omega_a/c)^2$, to obtain an equivalent expression,

$$2\pi\eta k_z^2 = \Omega\left(1 - \frac{\Omega^2}{\omega_b^2}\right) \tag{2.27}$$

where $\eta = \mu/\rho$ is the kinematic viscosity. This condition defines a maximum value of k_z (and hence a minimum vertical wavelength) for a given frequency, beyond which a wave is totally attenuated by viscous dissipation. Dissipation limits were calculated from height profiles of η given in Gossard and Hooke (1975, p220) and represented as dashed curves in figure 2.3. Permitted wave modes lie below the dissipation limit. The minimum vertical wavelength increases with height as molecular viscosity increases. As a result larger-scale waves predominate at greater heights.

The expression (2.27) applies to a model based on a non-dissipative atmosphere. Hickey and Cole (1988) compared dissipation rates in a model (A) which included in the wave equations, viscosity and thermal conduction terms appropriate to a dissipative atmosphere, with a basic model (B) which used a non-dissipative atmosphere, as in Hines (1960). Comparisons with a full-wave model showed that model B underestimated dissipation rates in the lower thermosphere, grossly overestimated rates in the middle thermosphere, and underestimated above 350 km.

The importance of molecular viscosity decreases rapidly below the turbopause ($\sim$110 km) where turbulent eddy viscosity predominates. As observations in this study were made above the turbopause, eddy viscosity will not be considered here.

Thermal conduction has dissipative effects similar to viscosity, since both are transport processes caused by molecular diffusion. Although the mechanisms are different, their dissipative effects may be combined to give an effective viscosity, $\eta' = (1 + \frac{f}{\gamma})\eta$, where $\frac{f}{\gamma} \simeq 1.4$ to 1.5, depending on the nature of the gas (Hines et al., 1974, p381).

2.3.4 Ion drag

The presence of ionization in the atmosphere has several effects on wave motion. If the gyrofrequency of an ionised particle is much greater than its collision frequency, it is constrained to move along a magnetic field line. At mid-latitudes, this occurs above about 90 km for electrons and above about 140 km for ions. One effect of this is that the response of the ionised medium to gravity waves is quite different in character and magnitude from the response of the neutral atmosphere. Another effect in regions of large ionisation is the modification of wave propagation and introduction of new wave modes (Gossard and Hooke, 1975, p239; Hines and Hooke, 1970). However, the effect on waves in the neutral component is collisional damping of any motion perpendicular to the magnetic field lines, called ion drag. Therefore the degree of damping is dependent on the direction of wave propagation. It is also dependent on the ratio of neutral-ion

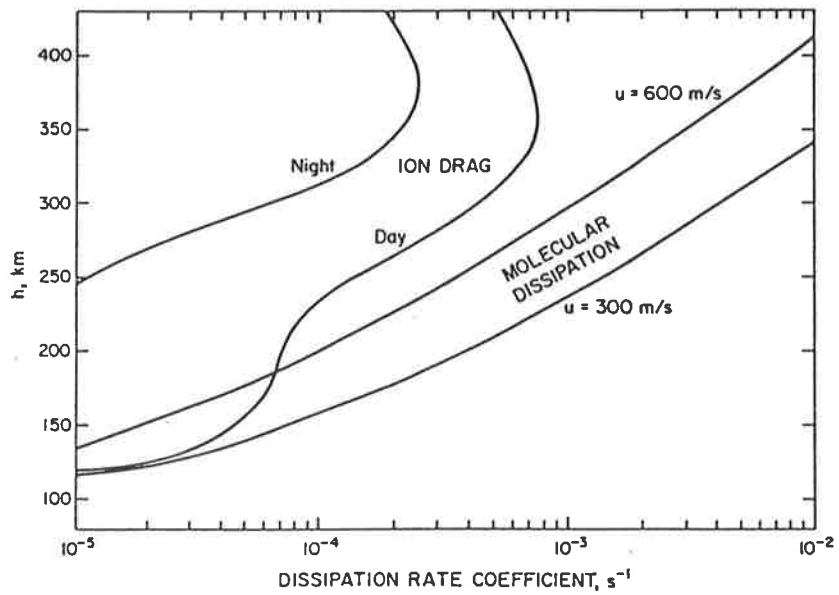

Figure 2.4. Comparison between energy-dissipation rate coefficients for molecular dissipation (viscosity and thermal conduction) and Joule dissipation due to ion drag. The molecular dissipation coefficient is shown for two horizontal wave velocities; the Joule dissipation coefficient is shown for typical day and night conditions (from Richmond, 1978b).

collision frequency to wave frequency, (ν_{ni}/Ω), so that damping effects are greatest in the F region where ν_{ni} maximises. At night, ν_{ni} decreases and only waves of period greater than several hours are significantly damped by ion drag (Gossard and Hooke, 1975, p241). Figure 2.4 illustrates the relative importance of molecular effects and ion drag as a function of altitude, and with time of day.

The combined effects of viscosity, heat conduction and ion drag on wave propagation were calculated by Richmond (1978b) in terms of wave phase speed and period. He found that slower moving and shorter period waves are most heavily damped, and are progressively filtered out as the distance from the source increases. For example, a wave generated at 110 km altitude, of period 2 h and horizontal speed of 300 ms^{-1} may travel 2500 km before being severely dissipated; a wave of half this period and speed may travel less than 1000 km. Therefore the fast-moving long-period waves are most important in global propagation.

2.3.5 Wave saturation

In contrast to the various dissipation mechanisms described, which act on waves of all dimensions, wave saturation refers to processes in which the growth limiting action is dependent on (large) wave amplitude. Hodges (1967, 1969) recognised that instabilities created by large oscillations may produce turbulence. This limits further growth of the wave, and transfers energy and momentum of the wave to the mean wind through eddy transport of heat and viscous stress (eg. Vincent and Reid, 1983). The mean wind is accelerated towards the phase speed of the wave. If the mean wind and phase speed are oppositely directed, wave breaking may bring about reversal of the mean wind direction. The effect of wave saturation on the middle atmosphere was parameterised by Lindzen (1981), showing that gravity-wave breaking provided the momentum transfer required to bring about the observed reversal of the mean zonal wind above the mesopause, and the warm winter and colder summer mesopause. These features of the atmosphere had long been observed (eg. Kellogg and Schilling, 1951) but until that time had not been adequately explained.

Wave saturation may occur through the linear processes of convective or dynamical instabilities, or through non-linear wave-wave or wave-vortical mode interactions.

Linear saturation theory is based on the creation of convective or dynamic instabilities by large amplitude oscillations of a wave (Fritts, 1984). Convective instability occurs when temperature oscillations cause the adiabatic lapse rate to be exceeded, ie. $\frac{\partial T}{\partial z} < -\alpha^*$. For a monochromatic wave, this is equivalent to the condition $\mid u' \mid > \mid c - \bar{u} \mid$ where u'=perturbation velocity, c=phase velocity, $\bar{u}$=mean wind velocity, in the notation of Fritts. This condition may occur either as a result of growth of wave amplitude with height (ie. an increase in $\mid u' \mid$) or as a wave approaches a critical level (ie. a decrease in $\mid c - \bar{u} \mid$). In both situations the wave begins breaking when the condition is fulfilled.

Dynamic stability is measured by comparing the stabilising influence of gravity and

temperature gradients with the destabilising influence of wind shears. It is measured by the Richardson number, $R_i = \omega_b^2 / \left(\frac{\partial \bar{u}}{\partial z}\right)^2$. A region becomes unstable when $R_i < \frac{1}{4}$.

Observations of dynamical and convective instabilities were reviewed by Fritts (1989) and Fritts and Rastogi (1985). Observations suggest that dynamical instabilities are common in the middle and lower atmosphere and associated with low frequency gravity waves. Convective instabilities have been less frequently studied, and appear to be associated with higher-frequency waves.

Atmospheric observations have shown that saturation occurs in waves of amplitudes less than those required by the linear theory outlined above. To account for this, Weinstock (1976, 1982) proposed a theory of non-linear interactions among a spectrum of waves. Such interactions give rise to energy transfer between waves, formation of new waves, and wave breaking. The theory predicted that wave breaking may occur when the individual waves are below saturation amplitude. However, Fritts (1985) supported the linear theory; he maintained that a spectrum of waves saturates mainly by convective instability created by superposition of the waves.

2.4 Sources of Gravity Waves

Thermospheric gravity waves can generally be classified into two categories: large-scale (LS) disturbances and medium-scale (MS) disturbances. Large-scale waves have horizontal wavelengths of the order of 1000 km, speeds of 400-1000 ms^{-1}, and periods of around 30 min to 3 h or more. They are generated in the high-latitude thermosphere by magnetic substorms, and propagate equatorward to mid-latitudes and further (Hajkowicz and Hunsucker, 1987). They may also occur following energetic events such as nuclear explosions and earthquakes. (Davies and Baker, 1965). Francis (1975) associated LS gravity waves with the ducted surface modes supported by the steep temperature gradient at the base of the thermosphere. Richmond (1978a), however, explained the ducting as total reflection of long-period freely-propagating waves in the

lower thermosphere, and weak reflection in the upper thermosphere through viscosity and heat conduction effects. He suggested that the resulting wave guide is too weak to be significant in general.

Medium-scale waves have horizontal wavelengths of the order of 100 km, speeds of 100-250 ms^{-1}, and periods ranging from the Brunt-Väisälä period (about 5-15 min in the thermosphere) to about 60 min. Theory predicts that they are more heavily attenuated than LS waves, but nevertheless have been observed to travel large distances (Chandra et al., 1979). MS waves are more easily generated than LS waves by natural sources, and therefore are more numerous. These sources exist over a range of latitudes and altitudes, so that sources of specific MS wave observations are difficult to identify. Satellite observations show that thermospheric gravity waves occur more frequently at higher latitudes (Potter et al., 1976; Newton et al., 1969) suggesting the importance of auroral sources. A study by Crowley et al. (1987) of MS TIDs over the Antarctic peninsula showed marked differences in the morphology of waves generated during magnetically quiet and active periods. During quiet times, waves were observed with low speeds and an anticlockwise diurnal rotation in propagation direction; during active times, some very high-speed waves were observed with no simple propagation trends.

Mid-latitude observations of MS TIDs propagating east-west during equinox and propagating poleward in summer (Davies and Jones, 1971) and winter (Munro, 1958) cannot be attributed to auroral sources. Other upper-atmosphere sources have been proposed, namely the equatorial electrojet (Knudsen, 1969), nonlinear breaking of tides, solar eclipses and supersonic motion of the terminator (Davis and DaRosa, 1970; Somsikov, 1987) and mid-latitude particle precipitation. Tropospheric sources of gravity waves include wind flow over topography (Blumen and Hart, 1988), the meteorological jet stream (Gavrilov and Shved, 1982; Waldock and Jones, 1987) and tropospheric storms and weather fronts (Freund and Jacka, 1979; Taylor and Hapgood, 1988).

2.4.1 Auroral sources

Theory and observations of high latitude sources were reviewed by Hunsucker (1982). He discussed two most likely mechanisms for gravity-wave generation, 1) Lorentz forces and Joule heating related to surges in the auroral electrojet current, and 2) intense heating by precipitating charged particles. He also discussed conditions under which gravity waves may be generated by supersonic motion of electron density irregularities.

Auroral electrojet currents act to produce gravity waves through two mechanisms. The first is the Lorentz force per unit mass, acting on charged particles $\mathbf{J} \times \mathbf{B}/\rho$, which is transferred to the neutral atmosphere through collisions, and the second is Joule heating of the atmosphere, $\mathbf{J} \cdot \mathbf{E}$ per unit volume (where $\mathbf{B}$ is the magnetic field strength, E is the electric field strength and $\mathbf{J}$ is the electric current density which includes terms related to the direct, Pederson, and Hall conductivities). The relative importance of these mechanisms in generating gravity waves is dependent on the height of the current source, the electric field strength, and the horizontal velocity of the wave. Based on a model by Chimonas and Hines (1970), Hunsucker (1977) estimated the relative contributions of Lorentz forces and Joule heating (L/J). He found L/J to be around 2.4 for an average electric field of 43 $\mathrm{mVm^{-1}}$. However, theoretical calculations by Brekke (1979) showed L/J decreased significantly with source height and increasing field strength, such that Joule heating dominates for sources at or above 120 km, when the electric field strength is greater than about 40 $\mathrm{mV\ m^{-1}}$.

The effects of particle precipitation are difficult to isolate from those of auroral currents. Electrojet current density is proportional to electron concentration, which may be increased by an order of magnitude or more during periods of strong particle precipitation. Crowley and Williams (1987) used profiles of electron concentration and measurements of plasma velocities to determine heating due to precipitating particles, and Joule heating by the electrojet current. They found that on average, the height integrated Joule heating was more than 10 times that of particle heating.

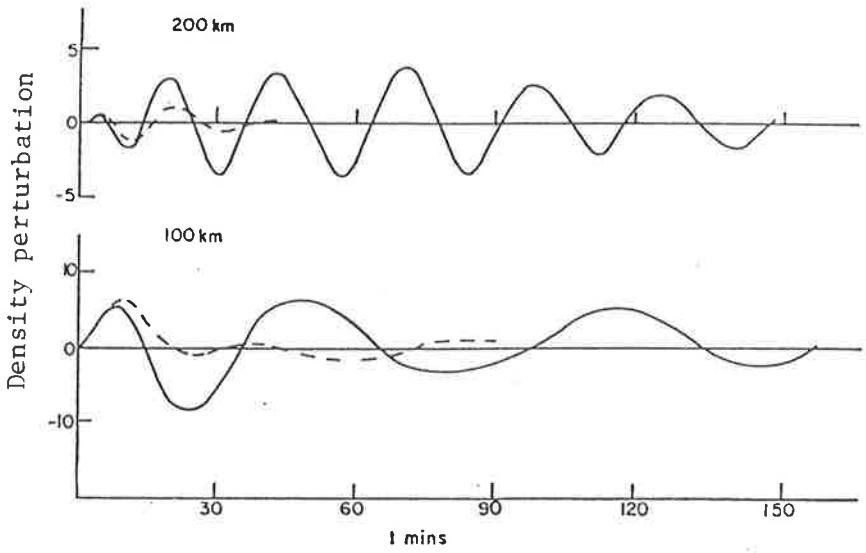

Figure 2.5. Gravity-wave-induced pressure perturbations, as a function of time, at a horizontal distance of 1000 km and heights of 100 and 200 km above the source. The dotted lines show the reduced amplitude caused by increasing the depth of the source by a factor of 5 (adapted from Chimonas and Hines, 1970).

Many workers have modelled the atmospheric response to surges in the auroral electrojet current. Richmond and Matsushita (1975) calculated the atmospheric wind and temperature variations caused by a disturbance in the auroral current, which was modelled as a 2-dimensional line source. The results showed a pulselike disturbance propagating equatorward at 750 ms^{-1}. Chimonas and Hines (1970) calculated the pressure response of the atmosphere, and the effect of increasing the dimensions of the source. Increasing the depth of the source by a factor of five significantly reduced the amplitude of the tail of the wave train, through interference (figure 2.5). Near field density and horizontal velocity perturbations were modelled by Luhmann (1980). The magnitude of perturbations in the very near field was found to be considerably reduced with the inclusion of an earth-reflected disturbance in the model.

Many observed characteristics of thermospheric gravity waves support the models of aurorally generated waves. Early observations concentrated on large-scale travelling ionospheric disturbances at mid-latitudes. Their correlation with magnetic activity was confirmed by Davis and daRosa (1969) who used columnar electron content records to measure LS TIDs travelling with speeds of 200-1000 ms^{-1}. Many observations have been made of their equatorward propagation from the winter pole (eg. Munro, 1958; Testud, 1970). More recently, Hajkowicz and Hunsucker (1987) presented data from a

network of ionosonde stations, showing LS TIDs generated simultaneously in the northern and southern auroral regions, and suggested particle precipitation as the source. The TIDs propagated equatorward at around 800 ms^{-1} with wavefronts of transverse length of 1600 and 7000 km in the southern and northern hemispheres respectively. Characteristics of auroral MS gravity waves were obtained by Chandra et al. (1979) from satellite measurements of kinetic temperature and neutral composition. They found that, in contrast to LS waves, MS waves showed little correlation with K_p index (which is derived from stations at geomagnetic latitudes 48°-63°). Rather they were usually observed to be preceded by major peaks in AE, which is a measure of electrojet activity derived from stations in the auroral zone. The waves propagated to mid-latitudes on the night side, and a corresponding distance over the polar cap to auroral regions on the day side.

2.5 Wave Generation and Propagation

The spectrum of waves observed at a particular location depends on the nature of the source, the horizontal and vertical distance from the source, and the effect of the dissipation mechanisms over the propagation path of the waves. The following discussion is based on the theory of propagation of medium-scale waves described by Francis (1974), and the propagation of large-scale thermospheric waves described by Richmond (1978b).

A source generates a spectrum of waves which is dependent on the spatial and temporal characteristics of the source. In a source region of Gaussian cross-section with vertical half width Δz, destructive interference reduces the amplitude of short-wavelength modes for which $k_z \Delta z > 1$ (Francis, 1974). A similar condition applies to sources with finite horizontal dimensions. A source in which the force acts over a period Δt, will not effectively produces waves for which $\Omega \Delta t > 1$. Results from the WAGS (Worldwide Atmospheric Gravity-wave Study) (Williams et al., 1988) indicate a direct correspon-

dence between periodicities in the sources and gravity-wave periods. They measured 33 min and 17 min periodicities in the auroral electric field using the EISCAT network; the same periods were measured 1 h later in gravity waves propagating over the UK.

The geometry of a source also affects the range dependence of the gravity-wave response. This may vary from an r^{-3} dependence for a vertical impulse point source to an r^0 (no) dependence for a switch-on horizontal line source (Francis, 1975). In general, geometrical spreading causes a decrease in response with range. This may be offset as a result of the anisotropic propagation of gravity waves, as follows. The energy of a low frequency wave propagates at any elevation angle up to Φ, given by $\sin\Phi = \frac{\Omega}{\omega_b}$. Therefore, low frequency waves propagate at small elevation angles and over large horizontal distances (for example, waves generated by a nuclear blast, Hines, 1967). Thus if a source excites mainly low frequency waves and its propagation is observed at fixed (ionospheric) heights by a series of stations, the disturbance appears to grow with horizontal distance as the low frequency component reaches observing heights. This may offset the effects of geometrical spreading and dissipation so that the wave is observed as a TID propagating unattenuated over large horizontal distances.

Another explanation for the long-distance propagation of medium-scale gravity waves was put forward by Mayr et al. (1984). They obtained a numerical model of the transfer function of the atmosphere to describe the wave response to a source representing Joule heating. One component of the response corresponded to a propagating wave generated in the thermosphere, then entering a duct formed by the earth's surface and the temperature minimum at the mesopause. Here the wave travels with little dissipation, while some energy leaks back into the thermosphere to be observed as medium-scale TIDs.

Because of the anisotropic propagation of atmospheric waves, the wave train arriving at a fixed observation point varies in frequency and amplitude. The arrival sequence of waves generated by an impulsive source is dependent on their group velocity. Figure 2.6 illustrates the relationship between elevation angle of energy propagation, period, and horizontal group velocity. Waves arriving at a fixed observation point all travel at

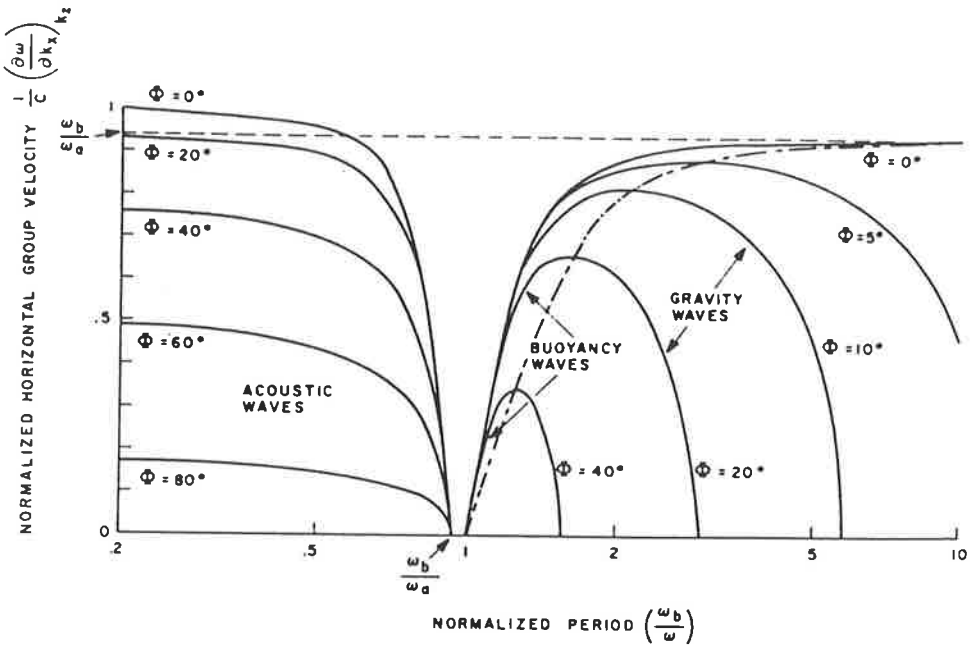

Figure 2.6. Contours of constant elevation angle of energy propagation, Φ as a function of normalised horizontal group velocity and period (from Francis, 1974).

elevation angle Φ. Following this contour and assuming the waves arrive in order of decreasing group speed, three distinct wave trains are observed. The first to arrive is the high-frequency acoustic wave, travelling at the speed of sound, c. Behind this are lower-frequency waves, asymptotically decreasing in frequency to the acoustic cutoff, ω_a. Shortly after the initial acoustic pulse another wavefront arrives and immediately splits into two wave trains, one approaching the Brunt-Väisälä frequency ω_b, and the other approaching the limiting low frequency $\omega_c = \omega_b \sin\Phi$, which decreases with increasing horizontal distance from the source (ie. with decreasing Φ). This change in frequency of the wave train with time is accompanied by a change in wavelength.

Francis (1974) modelled wave trains generated by a line source at 120 km altitude (as an approximation to the auroral electrojet). He considered the propagation of both direct waves and those reflected from the earth, in a dissipative atmosphere. At a fixed observation point, fluctuations due to the direct wave were seen as a pulselike disturbance with the waves which arrive later being significantly damped. Figure 2.7a shows modelled electron density fluctuations produced by a TID at 200 km altitude and at various ground ranges. The earth-reflected waves have a more common oscillatory form (figure 2.7b). Francis attributed the difference in form to dispersion of the reflected waves to such an extent that they appear monochromatic, whereas direct waves contain

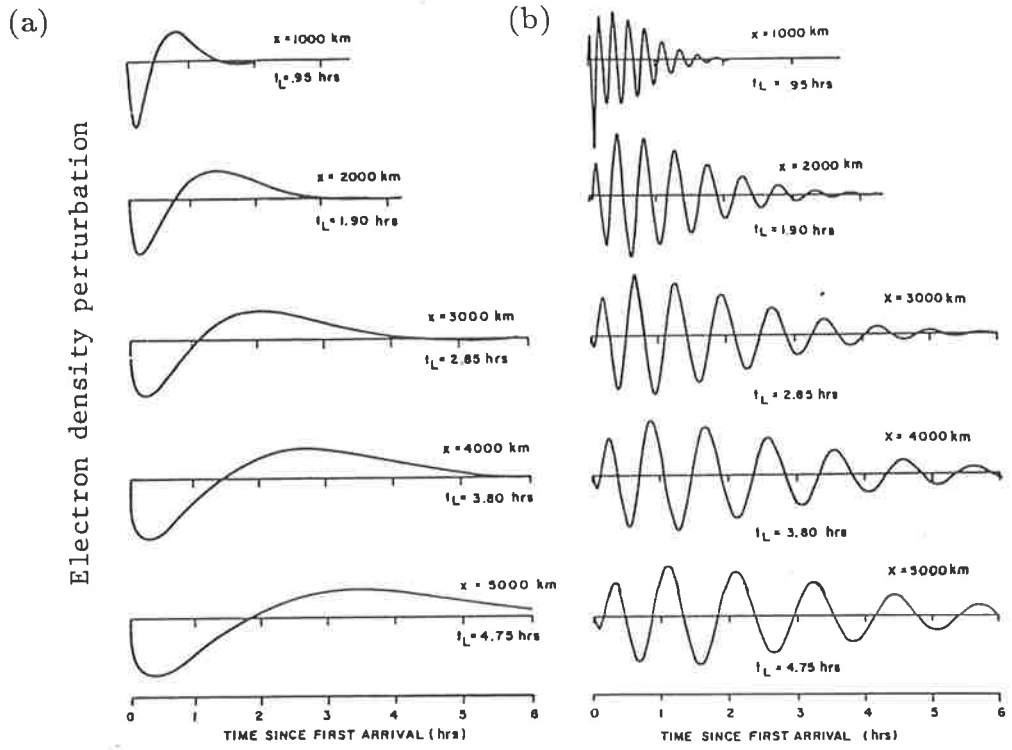

Figure 2.7. Modelled electron density fluctuations as a function of time, produced by a TID at 200 km altitude and various distances, x, from the source. t_L is the time raken to reach the field point. (a) direct wave (b) earth reflected wave (adapted from Francis, 1974).

many superposed frequencies.

2.6 Airglow and Auroral Emissions

In this study, gravity wave activity is measured through observations of intensity variations in several nighttime atmospheric emissions. These may be attributed to airglow, which is a continuous, extremely weak emission occurring at all latitudes, and at high latitudes, to both airglow and auroral emissions. The aurora can be formless and quiescent, but during moderate activity, becomes more intense and structured. The fundamental difference in the two forms of emission lies in the excitation mechanism. Airglow is the result of chemical reactions between atmospheric constituents and auroral emission is excited by precipitating solar particles. Emissions under consideration here are the λ630 nm and λ558 nm lines of atomic oxygen, which occur in both airglow

and aurorae. Excitation mechanisms for both emissions are discussed individually, and the theory and observations of gravity-wave interaction with atmospheric emissions is outlined. Vallance Jones et al. (1985) and Torr and Torr (1982) reviewed the major atmospheric emissions; Forsyth and Wraight (1987) reviewed periodic variations in the nighttime emissions.

2.6.1 The λ630 nm oxygen emission

The 'forbidden' λ630 nm red line is produced as part of a doublet by the transition from an excited state to the ground state of oxygen

$$O(^1D) \longrightarrow O(^3P) + h\nu_{630,\ 636}$$

and has a radiative lifetime of around 110 sec. Nighttime λ630 nm airglow emanates from a broad layer near 200-250 km altitude (Gulledge et al., 1968; Hays et al., 1978). $O(^1D)$ nightglow is excited predominantly by dissociative recombination of O_2^+, and also by hot thermal electron impact.

At high latitudes the λ630 nm emission is due mainly to auroral excitation. A typical λ630 nm nightglow intensity is 50-100 R (Chamberlain, 1961) compared with an IBC1 λ630 nm auroral intensity of around 600 R (Sharp et al., 1979). The excitation processes of auroral $O(^1D)$ are not completely understood. Research on possible mechanisms is summarised by Meier (1987). Mechanisms thought to contribute to the production of nighttime auroral $O(^1D)$ are (Rees and Roble, 1986; Solomon et al., 1988):

$$O_2^+ + e \longrightarrow O(^1D) + O \qquad \text{dissociative recombination} \qquad (2.1)$$

$$O + e \longrightarrow O(^1D) + e \qquad \text{auroral electron impact} \qquad (2.2)$$

$$O + e_t \longrightarrow O(^1D) + e \qquad \text{thermal electron impact} \qquad (2.3)$$

$$O_2 + e \longrightarrow O(^1D) + O \qquad \text{impact dissociation of } O_2 \qquad (2.4)$$

$$O(^1S) \longrightarrow O(^1D) + h\nu_{557.7} \qquad \text{cascading} \qquad (2.5)$$

$$N(^2D) + O_2 \longrightarrow O(^1D) + NO \qquad \text{atom interchange} \qquad (2.6)$$

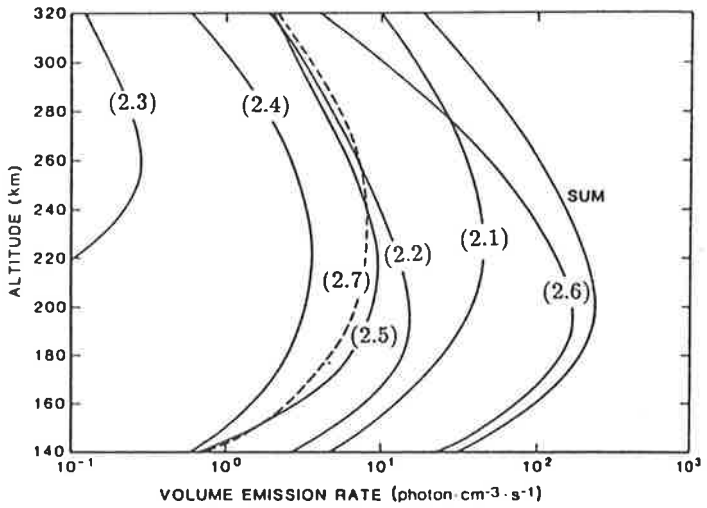

Figure 2.8. Modelled height profiles of λ630 nm volume emission rates for an integrated λ630 nm intensity of 2 kR. Contributions from the various possible mechanisms are labelled as in the text (adapted from Rees and Roble, 1986).

$$N^+ + O_2 \longrightarrow O(^1D) + NO^+ \qquad \text{ion-atom interchange} \qquad (2.7)$$

$$N(^2P) + O \longrightarrow O(^1D) + N(^4S) \qquad \text{quenching of } N^* \qquad (2.8)$$

$O(^1D)$ is removed through quenching by N_2 and O_2 at similar reaction rates, but N_2 has the dominant effect because of its higher concentration (Hays et al., 1978). There is some uncertainty about the quenching effect of $O(^3P)$ (Abreu et al., 1986).

Analysis of satellite and rocket data by Sharp et al. (1979, 1983) showed that dissociative recombination of O_2^+ and auroral electron impact accounted for only 10% of the observed λ630 nm intensity below 250 km. Rees and Roble (1986) discussed $N(^2D)$ atom interchange as the main excitation mechanism, with dissociative recombination and auroral electron impact contributing around 10% each. Figure 2.8 shows their computed height profiles of volume emission rates for the mechanisms (2.1) to (2.7). Intensity peaks occur at different altitudes for most mechanisms, resulting in a broad total peak which ranges from 180-240 km altitude for the softest to hardest electron spectra. More recent modelling (Solomon et al., 1988) suggests that dissociative recombination of O_2^+ and auroral electron impact on O are the major contributors and the remaining mechanisms contribute to varying minor degrees. Solomon et al. found reasonable agreement between their models and measurements of λ630 nm volume emission rates from the Atmospheric Explorer Visible Airlow experiment.

2.6.2 The λ558 nm oxygen emission

The 'forbidden' λ558 nm green line is produced in the transition between two excited states of oxygen

$$O(^1S) \longrightarrow O(^1D) + h\nu_{558}$$

which is accompanied by the weaker transition

$$O(^1S) \longrightarrow O(^3P) + h\nu_{297}$$

The radiative lifetime of $O(^1S)$ is about 0.8 sec. λ558 nm nightglow emission emanates from a layer of width 6-10 km at 97 km altitude, and a much wider layer in the F region (Gulledge et al., 1968; Thomas, 1981). The F region emission is produced through dissociative recombination of O_2^+, and at mid-latitudes is about 1/10 the intensity of the lower layer. For many years the layer at 97 km was thought to be produced via the association energy of O_2 in the Chapman mechanism,

$$O + O + O \longrightarrow O(^1S) + O_2$$

where O denotes the ground state of atomic oxygen, $O(^3P)$. However, arguments based on reaction rates (as reviewed in Torr and Torr, 1982), suggested that the following two step Barth mechanism is responsible

$$O + O + M \longrightarrow O_2^* + M$$

followed by collisional energy transfer

$$O_2^* + O \longrightarrow O_2 + O(^1S)$$

where M is the neutral species O_2 or N_2, and O_2^* is a vibrationally excited state. The reaction rate of the Barth mechanism is reduced by the de-excitation of O_2^* through radiation or quenching by O_2 or N_2. The λ558 nm emission rate is reduced through quenching of $O(^1S)$ by O and, predominantly, O_2 (Witt et al., 1979; Thomas et al., 1979).

The λ558 nm line is the strongest visible emission in the aurora, and at auroral latitudes is far stronger than the λ558 nm airglow. An intensity of 250 R is typical for λ558 nm

airglow compared with 1000 R for an IBC1 λ558 nm auroral intensity (Chamberlain, 1961). The excitation mechanism for auroral $O(^1S)$ production has not been conclusively determined. Rees (1984) and Gattinger et al. (1985) discussed the following possible mechanisms:

$O + e$	$\longrightarrow$	$O(^1S) + e$	direct electron impact
$O_2^+ + e$	$\longrightarrow$	$O(^1S) + O$	dissociative recombination
$N^+ + O_2$	$\longrightarrow$	$O(^1S) + NO^+$	ion-atom interchange
$O_2^+ + N$	$\longrightarrow$	$O(^1S) + NO^+$	
$N_2(A^3\Sigma_\mu^+) + O$	$\longrightarrow$	$O(^1S) + N_2$	energy transfer

Current evidence suggests that energy transfer from the excited $N_2(A^3\Sigma_\mu^+)$ state is the dominant process (Gerdjikova and Shepherd, 1987; Henriksen and Egeland, 1988). Above 200 km altitude, N_2 concentration decreases significantly and the alternative mechanisms become important in $O(^1S)$ excitation. $N_2(A^3\Sigma_\mu^+)$ is excited by direct electron impact and is quenched by O and O_2 (Parkinson and Zipf, 1970), which reduces the rate of excitation of $O(^1S)$ below 100 km. Modelled contributions of these mechanisms are shown in figure 2.9.

The height and shape of the λ558 nm emission layer is dependent on the energy of precipitating particles; higher energy particles produce a narrower peak at lower altitudes. Schmidtke et al. (1985) presented λ558 nm height profiles obtained from rocket flights. They found that emission peaks occurred around 105 km and 120 km for a diffuse aurora and a stable arc, respectively. Jones and Jacka (1987) estimate a λ558 nm emission height of 100-130 km by comparing temperatures obtained from Doppler line widths with temperature-height profiles from the US Standard Atmosphere, 1976. Measurements were made at the same location (Mawson, Antarctica) as the observations used in this study and so provide an appropriate estimate of the λ558 nm emission height. An average height of 120 km is used in the current work. This estimate obviously relies on the accuracy of the atmospheric model referred to by Jones and Jacka (1987).

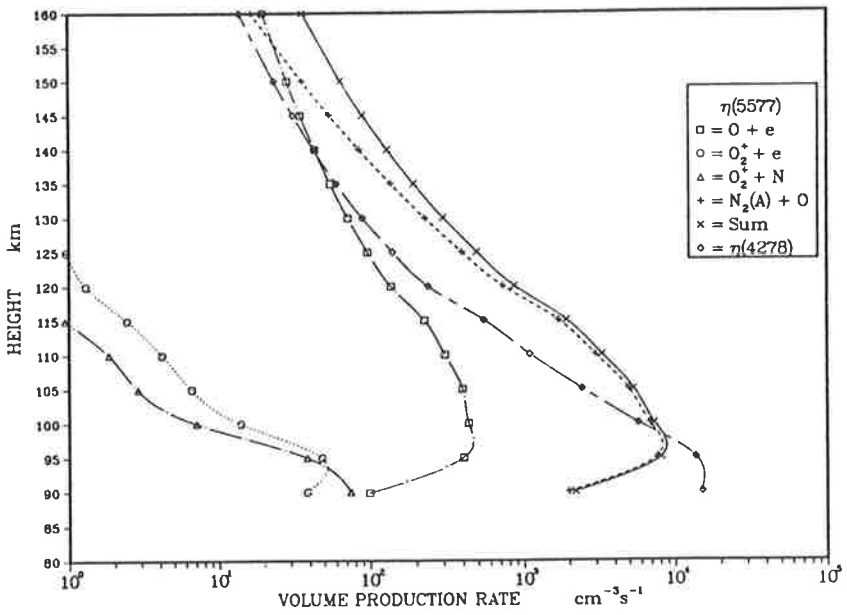

Figure 2.9. Modelled height profiles of λ558 nm volume emission rate for a type-B aurora with integrated λ428 nm intensity of 20 kR. Contributions from various possible mechanisms are shown (adapted from Gattinger et al., 1985).

2.6.3 The interaction of gravity waves with atmospheric emissions

The passage of a gravity wave perturbs the local atmospheric density and temperature and hence the intensity of atmospheric emissions. Weinstock (1978) investigated the effects of gravity waves on the density of minor atmospheric constituents, using the relationship

$$\frac{\rho_c'}{\rho_c} = \frac{1-\gamma H/H_c}{1-\gamma}\,\frac{\rho'}{\rho}$$

where the subscript c refers to the minor constituent and the dashed values refer to perturbations. He determined the relationship between density and temperature fluctuations and perturbations in O_2 and OH airglow emission intensity. This requires knowledge of the excitation mechanism and density profiles of the constituents so that, for auroral emissions, calculations become somewhat more difficult, as the excitation mechanisms are not well known and the emission height is variable. Weinstock concluded that temperature fluctuations provide a clearer, more reliable indication of gravity-wave activity than brightness fluctuations, as the latter may become very small for large wave amplitudes and/or a thin oxygen layer. However, Hines and Tarasick

(1987) derived a different relationship which does not support this preference for temperature measurements as a means of monitoring gravity waves. Measurements of the OH emission made by Viereck and Deehr (1989) showed the ratio of relative intensity perturbations to relative temperature perturbations was dependent on wave period. For shorter period waves, intensity and temperature fluctuations are of the order of 30% and 10% respectively, of the mean values; for longer period waves, the values are 50% and 10% respectively.

Observations of variability in atmospheric emissions are made commonly with photometers, or for higher spatial resolution, with imaging systems (Armstrong, 1982). Both methods measure an intensity integrated through the emission layer so that no height resolution within the layer is available. The horizontal component of wavelength and phase velocity of a wave can be obtained from measurements made with multi-field or scanning photometers. Using a four-field photometer, Freund and Jacka (1979) observed irregularities in the λ558 nm emission drifting at velocities of 50-100 ms^{-1}.

Gavrilov and Shved (1982) made observations of mid-latitude airglow at 49 points in the sky. Their work illustrated the averaging of wave parameter measurements caused by the finite thickness of the emission layer and atmospheric scattering of light. A power spectrum taken from one night showed that as the zenith angle of observation increased, the position of peaks in the power spectrum remained constant, but peak heights decreased and the peak broadened.

Simultaneous observations of emissions from two or more heights have been used to obtain information on vertical wave characteristics. Takahashi et al. (1985) carried out meridional scans of $Na\ D$ line and OH band emissions. They observed wavelike features in both emissions which was interpreted as a poleward propagating wave; similar features observed only in the NaD emission were interpreted as sodium irregularities moving with the wind. Takahashi et al., (1985) also made zenith observations of the OI λ558 nm and $Na\ D$ lines, and OH and O_2 atmospheric bands. They measured waves propagating through these adjacent emissions with vertical phase propagation speeds of about 1.7 ms^{-1}.

Because of the large vertical separation of the λ630 nm and λ558 nm emission layers, observations of correlated intensity variations in these emissions are less common. Misawa et al. (1984) investigated both emissions at mid-latitudes and found intensity covariations on 8 out of 187 nights of observations. They attributed these occurrences to intense auroral substorms using visual comparisons with magnetograms, Pi2 and AE index records.

At higher latitudes, auroral activity complicates optical observations of gravity-wave effects. Nevertheless, some observations have been made despite the presence of auroral activity. Clairemidi et al. (1985) observed OH emissions at Sodankyla, Finland, lying near the edge of the auroral oval, but observing southward, away from the oval. They photographed areas of the sky covering over 1 million km^2, in which wavelike features were visible. These often occurred at the same time as active aurorae in the north, indicating a correlation between wave activity and particle precipitation. Myrabø et al. (1987) measured intensity variations in $OH(6-2)$ band and $Na\ D$ line emissions over the polar cap. They found little correlation between wave induced intensity variations and indices of geomagnetic activity (Kp index, geomagnetic storm sudden commencement, and boundary crossing of the interplanetary magnetic field).

Observations of gravity-wave activity in the oxygen λ630 nm and λ558 nm emissions at high latitude are less common. Ismail and Cogger (1982) and Mullen et al. (1977) carried out studies of the λ558 nm emission over the polar cap, but concentrated on the diurnal and seasonal variations. This study is focussed on the short-term variations at auroral latitudes.

Chapter 3

The Three Field Photometer

3.1 Introduction

Many types of photometers, spectrometers and imaging systems have been used in studies of airglow. Photographic imaging has been used extensively and gives high spatial resolution and wide sky coverage. Clairemidi et al. (1985) used six cameras covering an azimuthal range of 240° to observe a wave field with an area of over 1 million km^2. The temporal resolution available with photographic techniques is limited by the exposure times required (typically 5-10 min) while the brightness of features and sensitivity of photographic emulsions limit the spectral range of emissions which can be recorded. The OH bands in the infrared region of the spectrum have been observed most commonly in photographic imaging (eg. Moreels and Herse, 1977). Armstrong (1985) used an image intensifier and filters fitted to a camera, to record wave activity in the OI λ558 nm emission. A significant disadvantage of photographic imaging is that for detailed analysis the records must be digitised, which is time consuming and inconvenient. Real-time testing and monitoring of observations is not straightforward. These problems may be overcome by using electronic imaging detectors, but practical low-light detectors of this sort are relatively new and have not yet been used for optical studies of gravity waves.

Alternatively, an instrument which cyclically samples sections of the sky may be used.

Photometers fitted with interference filters to select the emission of interest and single or multiple detectors, have been commonly used. If more than one emission is to be studied, a filter wheel may be used to rotate different filters into the optical path, or separate detectors and filters may be used for each emission. Filter bandwidths are typically around 1.0 nm, but range from 0.3 to 5.0 nm (Forsyth and Wraight, 1987).

Tilting-filter photometers are used to sample the continuum intensity near the emission feature, or to obtain low resolution spectra. For example, Misawa and Takeuchi (1977) measured diurnal variations in the intensity of the $O_2(0-1)$ band at λ864.5 nm. They used a filter with peak transmission at λ869.5 nm, for normally incident light. By tilting it through 15° they were able to shift the peak by up to 14.8 nm to record low-resolution spectra of the emission band. These techniques have limitations, since the filter bandwidth increases and the transmission decreases as the tilt angle increases. When better resolution and control over the observed wavelength are required, grating spectrometers or interferometers are used (as in OH rotational temperature measurements made by Meriwether, 1979).

Horizontal dimensions and propagation velocities of airglow features can be determined by sampling three or more regions of the sky. Multiple field and scanning photometers have been used for this purpose. Meek and Manson (1983) used a single photometer with an electronically-controlled mirror system to scan 30 discrete, adjacent regions of the sky. This method has the advantage of giving good spatial resolution over a large area of sky (30 fields of diameter ~2 km, located around a circle of diameter 16 km at the emission height), but a compromise is made on the frequency of scans (one circular scan per minute) and the shortest period which can be measured.

In the present study, a three-field photometer was used to measure variations in atmospheric emission intensity in three spaced regions of the sky. A rotating filter wheel held filters which isolated the emissions of interest. Two filters were selected to isolate the atomic oxygen λ630 nm and λ558 nm emissions which occur at altitudes of approximately 220 km and 120 km respectively. The N_2^+ auroral band emission at λ428 nm was also monitored to provide an indication of the energy flux of ionising particle pre-

cipitation. Data logging and automatic operation of the photometer were controlled by a Commodore Business Machines (CBM) microcomputer. The system was installed at Mawson in 1981 and has been in operation from March to October in all subsequent years. It is similar to the photometer described by Jacob (1985) which was used to measure airglow intensity fluctuations near Adelaide, Australia. Figure 3.1 shows the three-field photometer assembly. The major sections of the photometer system will be discussed individually.

3.2 The Optical System

The three channels of the photometer share a common objective lens which is mounted through the roof of the building. A glass window supported by a heated metal cylinder separates moist laboratory air from cold air above, preventing condensation on the objective lens. A telecentric lens is positioned below the objective lens (at a distance equal to its own focal length). Below this, in the image plane, is a rotating filter wheel with the facility for holding up to six interference filters. For this project, three of the six filter positions were used, spaced at angles of 120°, holding two narrow bandpass interference filters, of nominal peak wavelengths λ630 nm and λ558 nm, and a λ450 nm broad bandpass filter. The filter mounting allows adjustment of the tilt angle during calibration, but this remains fixed during observation. The filter wheel is motor driven and rotates in 120° steps, to position the filters cyclically over each field. Filter selection and observing times are software controllable. Directly below the filter wheel is an isolation shutter which protects the photomultipliers from excessive light. This may be operated manually, but in normal automatic mode is controlled by computer, with an additional photodiode sensing and protection circuit. Further protection is provided by a lockout timer which limits observing hours to nighttime. Below the shutter are collimating lenses for each field which direct light onto photomultiplier detectors of type EMI 9658B with S20 photocathodes. They are housed in a thermally insulated cooling chamber, separated from the warm optical system above by double windows.

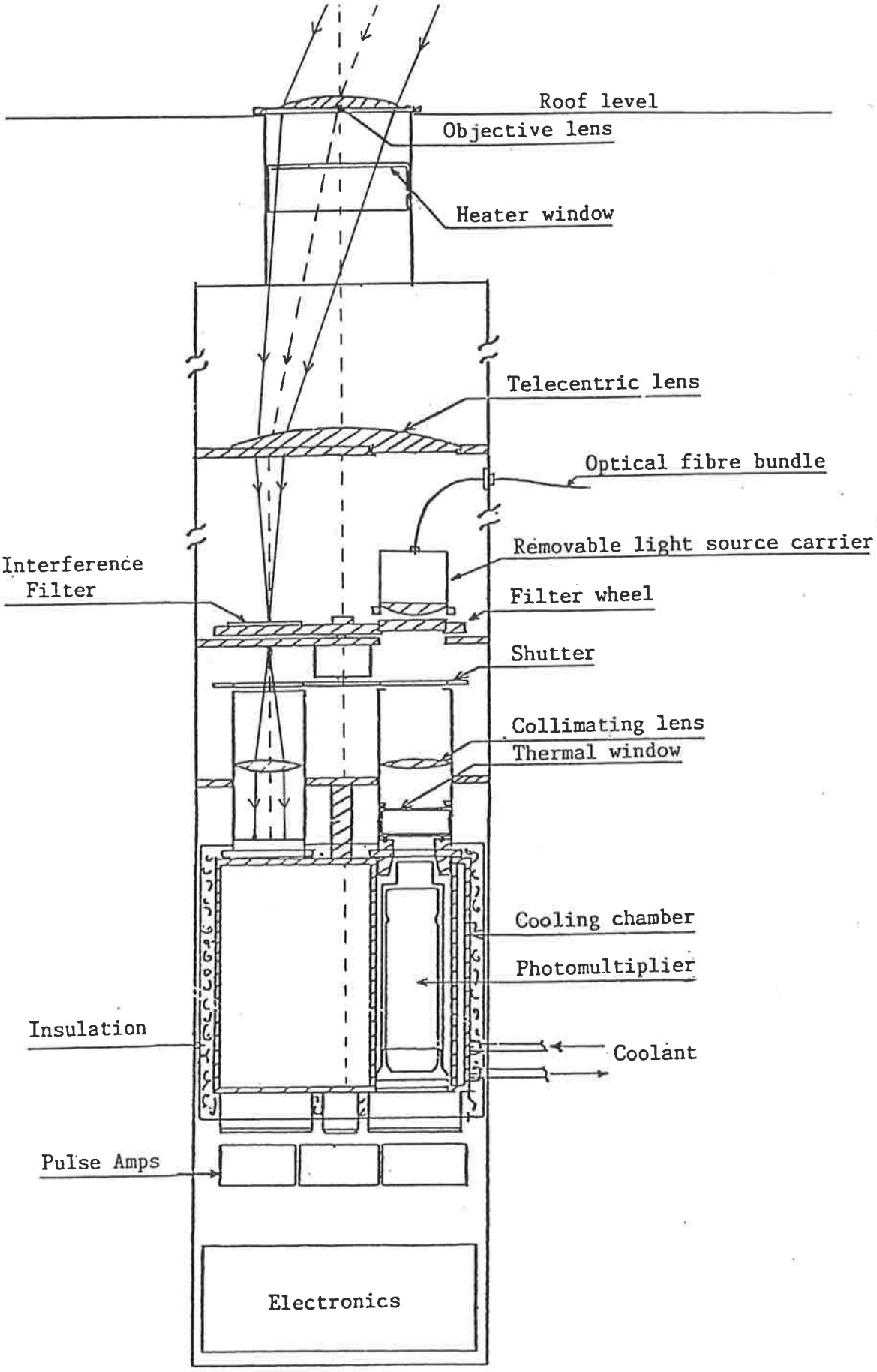

Figure 3.1. Three field photometer assembly showing the optical path of light from the centre of one observing field in the sky, to the photomultiplier cathode (adapted from Jacob, 1985).

The chamber coolant is circulated through an outside radiator so that the operating temperature of the photomultiplier tubes is close to external ambient temperatures (ie. typically -15° C). The complete instrument, including electronics, is enclosed in a light-tight metal casing with removable panels.

The size and position of the three observing fields at the emission height can be determined by tracing the optical path of light through the system, as shown for one field in figure 3.1. Parallel rays enter the objective lens, which forms the entrance pupil of the system. The emergent cone of light is focussed by the telecentric lens, such that its axis is parallel to the main optical axis. The filters are located in this image plane of the sky, and form the field stops for each field. After passing through the filters, the divergent beam is collimated onto the photocathode of the detector, which is the exit pupil. Referring to figure 3.2, the off zenith angle to the centre of each field stop is given by

$$\tan\Theta = \frac{r}{l} = \tan\ 4.68° \tag{3.1}$$

where r = distance between centre of the field stop and the optical axis = 67 mm

l = focal length of the telecentric lens = 818 mm

The distance from the centre of the field to the optical axis at the emission height L, is $R = L\tan\Theta$. The separation of the fields is then,

$$\begin{aligned} S &= 2L\ \tan\Theta\ \cos 30° \qquad (3.2)\\ &= 31.2 \text{ km} \quad \text{at 220 km altitude}\\ &= 17.0 \text{ km} \quad \text{at 120 km altitude} \end{aligned}$$

The diameter of the field stops, $d = 48$ mm, determines the field of view,

$$\Phi = 2\left[\arctan\left(\frac{r + d/2}{l}\right) - \Theta\right] = 3.33° \tag{3.3}$$

The diameter of the fields at the emission height is then

$$\begin{aligned} D &= 12.9 \text{ km} \quad \text{at 220 km altitude}\\ &= 7.0 \text{ km} \quad \text{at 120 km altitude} \end{aligned}$$

The orientation of the fields in the sky is shown in figure 3.2.

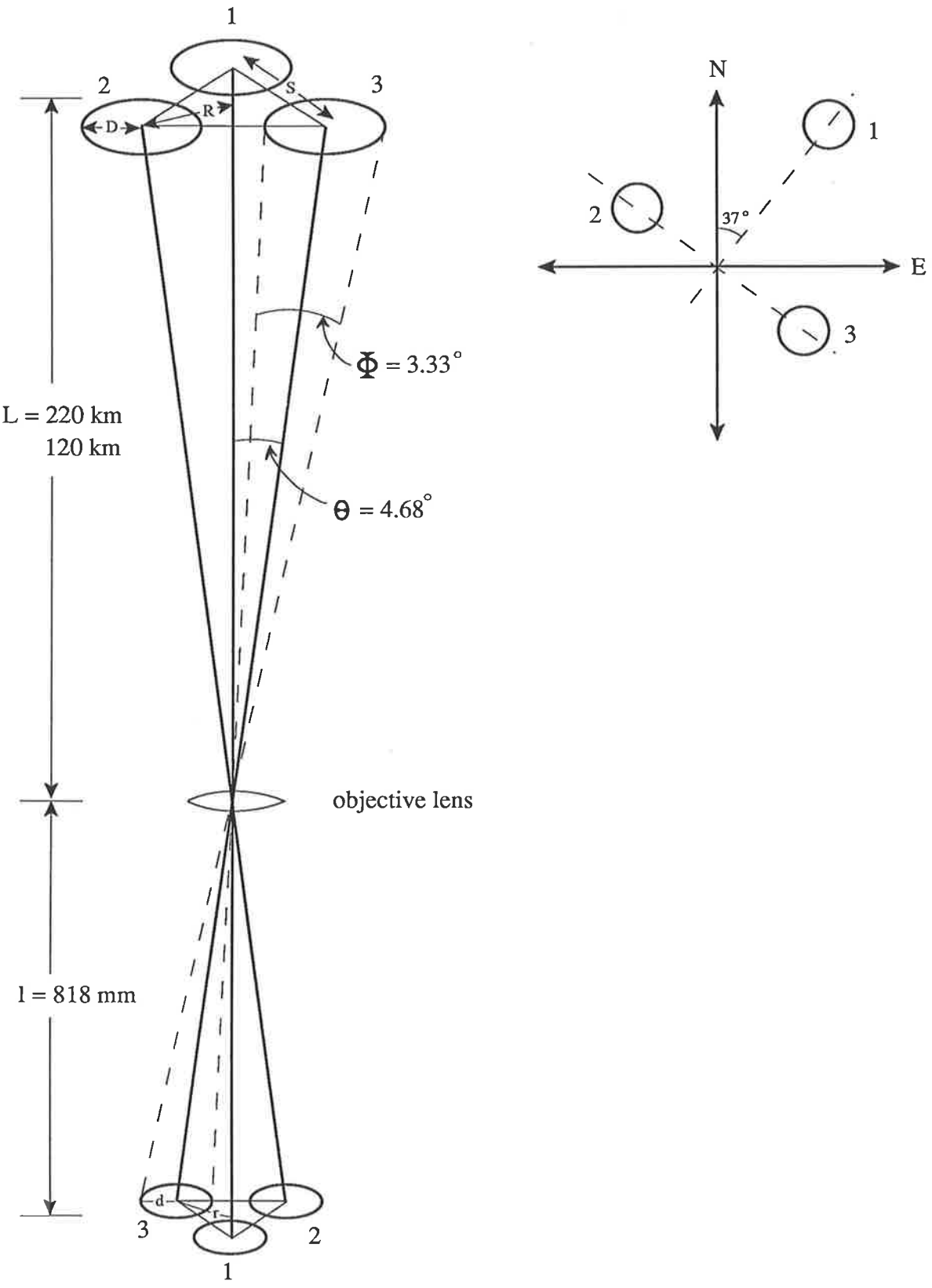

Figure 3.2. Projection of the three photometer fields onto the emission layer, and their orientation with respect to geographic north.

3.3 Electronics and Control System

The operation of the photometer is controlled by microcomputer. Start and stop times are entered before each observation run; the startup and shutdown procedure is computer initiated. During operation, the computer records data, controls filter rotation, and continuously checks photometer status. Timing is provided by the computer's internal clock. A block diagram of the photometer electronics and control system is shown in figure 3.3. The computer uses an 8 bit word transmitted serially to the photometer to control switching of photomultiplier EHTs, opening and closing of the shutter, and filter wheel positioning. These controls may be manually overridden using front panel switches. Photometer status is returned serially as two 8 bit words, containing the binary coded filter wheel position, shutter position (open/closed), light conditions from the photodiode detector (high/low), and scaling factors corresponding to each filter.

The observing sequence is controlled with one BASIC control program. During 1987 the photometer was configured to observe at three wavelengths by cyclically positioning the filters over each of the three fields. Aquisition time at each position was 3.7 s and travel time between positions was 2.3 s; the time for a 360° rotation cycle was then 18.0 s. Thus the data interval for the time series for each wavelength at each field was 18.0 s, so that it was possible to measure wave periods of less than 1 min. This is well below the shortest period expected for gravity waves.

Data is recorded as the number of pulses from the photomultiplier detectors. Pulses are standardised by amplifier-discriminators connected to the anode of each detector. During high auroral activity, pulse count rates of up to 6000 kHz are possible, that is, a total count of 20 000×10^3counts per acquisition time. Since the counting circuitry uses 16 bit counters (65×10^3counts), it is necessary first to prescale counts. Scale factors of 2^5 to 2^{11} are manually selected using front panel switches. Scaled counts and scale factors for each filter are logged by computer onto floppy disk. Data from each night are stored in individual files. These are structured such that each file can contains a maximum of 1016 records. Each record in the file contains two rotation cycles, and one

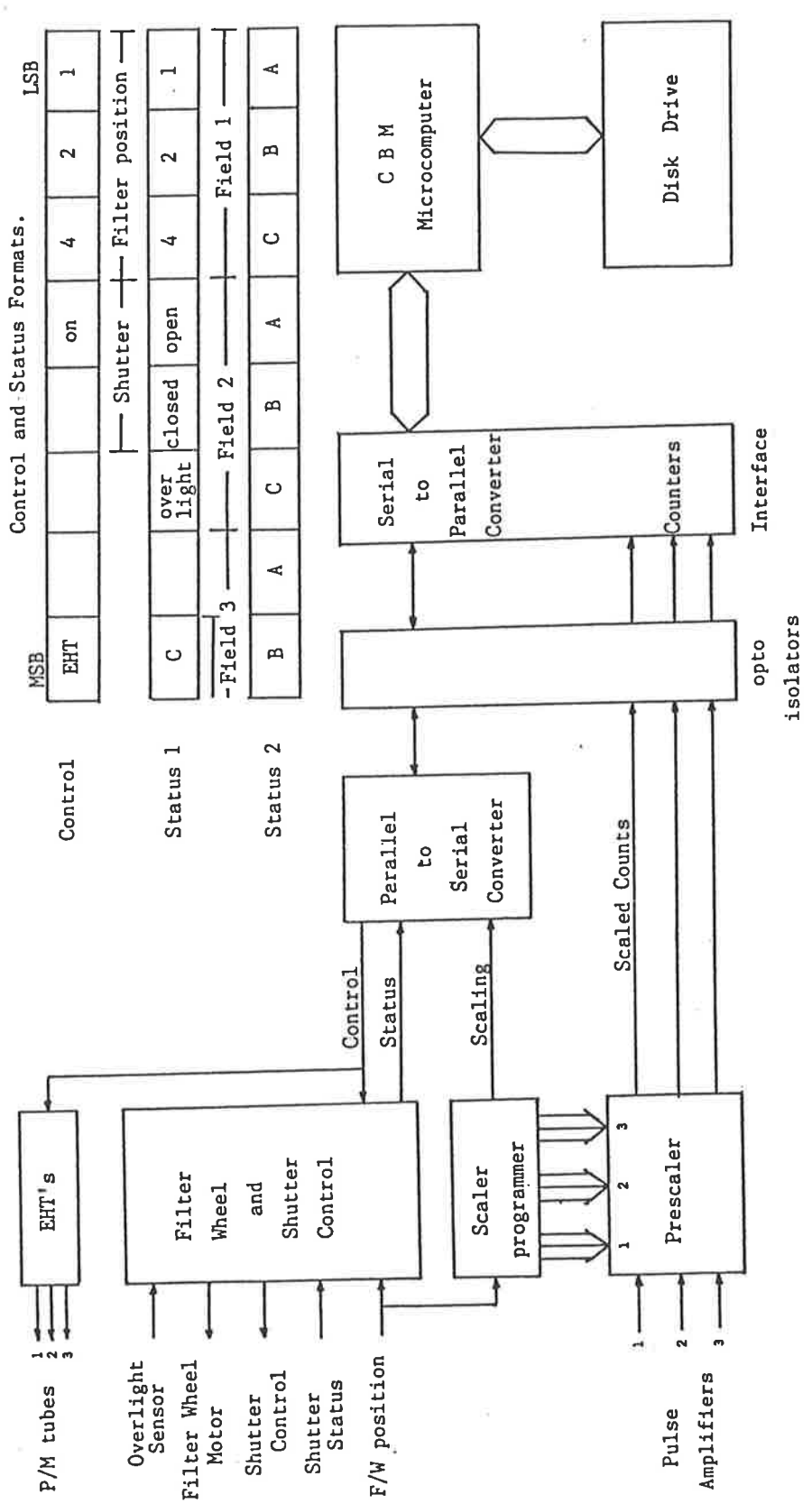

Figure 3.3. Block diagram of photometer electronics and control system (from Jacob, 1985).

rotation cycle produces 9 counts and scale factors, one for each filter over each field. In 1987, when one rotation cycle required 18 s, the maximum observation length was then 10.2 h.

3.4 Filters

3.4.1 Filter characteristics

Narrow bandpass interference filters were used to select specific atmospheric emissions. An interference filter is essentially a Fabry-Perot etalon, with a solid dielectric spacer. Texts such as Born and Wolf (1970) describe the theory of an ideal Fabry-Perot elaton; the following discussion is based on that of Jacka (1984). Consider two plane parallel plates, of which the inner surfaces are coated with reflective films. Light entering the enclosed air space undergoes multiple reflections, with some transmission at each reflection. Successive transmitted wavefronts emerge with a phase difference of $2\pi m$, where m is the order of interference, given by

$$m\frac{\lambda}{2} = \mu t \cos\theta + \frac{\lambda\phi}{2\pi} \tag{3.4}$$

where μ = refractive index of spacer medium

t = geometric separation of reflecting surfaces

θ = angle of incidence of rays between etalon plates

λ = vacuum wavelength

ϕ = phase change upon reflection at each plate surface, which is a function of λ and θ

Equivalently,

$$m\frac{\lambda}{2} = t_e \tag{3.5}$$

where $t_e = \mu t \cos\theta + \frac{\lambda\phi}{2\pi}$ is the effective thickness of the etalon spacer. Maximum transmission is achieved when m = 1,2,3... ie. complete constructive interference, and

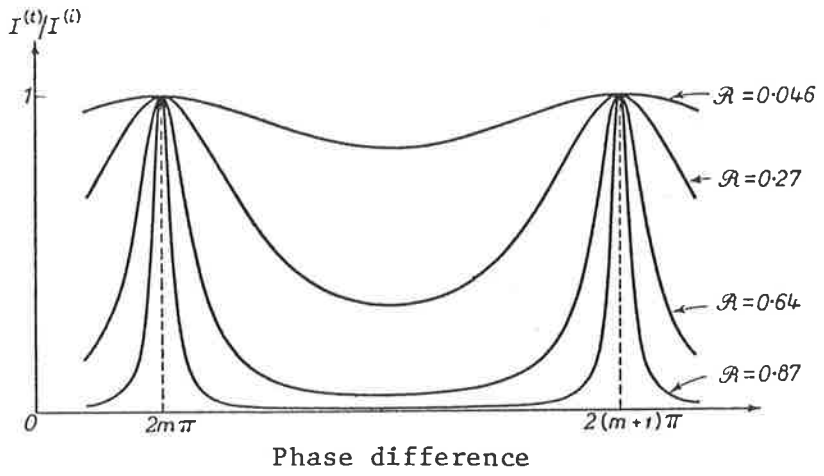

Figure 3.4. The ratio of transmitted to incident intensity as a function of phase difference, $2\pi m$ over two consecutive maxima, for a range of reflectances (adapted from Born and Wolf, 1970).

minimum transmission occurs when $m = \frac{1}{2}, \frac{3}{2}...$ ie. destructive interference. The ratio of transmitted to incident intensity as a function of m, is given by the Airy function

$$A(m) = \frac{\mathcal{T}^2}{(1-\mathcal{R})^2 + 4\mathcal{R}\sin^2(\pi m)} \tag{3.6}$$

$\mathcal{R}$ = reflectance of the plate surfaces

$\mathcal{T}$ = transmittance of the plate surfaces

$\simeq 1 - \mathcal{R}$ for small absorption and scattering

The ratio of transmitted to incident intensity, as a function of phase difference, $2\pi m$, is illustrated in figure 3.4 showing two maxima corresponding to integral m and $m+1$, for a range of reflectances.

An interference filter is a Fabry-Perot etalon in which the spacer is a solid dielectric rather than air. Reflective coatings, in the form of metal films or multiple layers of dielectric material with alternating high and low refractive index, are deposited on the optically flat spacer surfaces. For dielectric coatings, maximum reflectivity is achieved when the optical thickness of each layer is $\frac{\lambda}{4}$, for which $\phi = 0$. Therefore for normally incident light, maximum transmission occurs at wavelengths λ_m where $m\lambda_m/2 = \mu t$, $m = 1, 2, ..$ If the optical thickness μt is large, many maxima corresponding to a range of m are formed in the visible spectra. If the optical thickness is

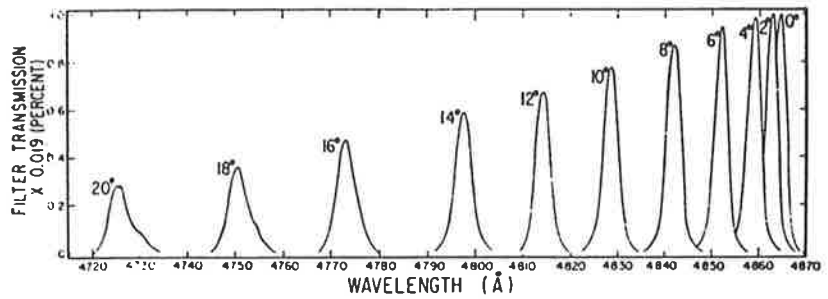

Figure 3.5. Change in filter characteristics with tilt angle θ', for a narrow bandwidth filter (λ=486.5 nm, bandwidth = 0.31 nm). As the tilt angle increases, the wavelength of peak transmission decreases, the transmitted intensity decreases, and the bandwidth increases (from Eather and Reasoner, 1969).

of the order of one wavelength, the maxima are widely separated in wavelength, and extraneous maxima can be suppressed using absorption filters.

Filter characteristics are variable; peak transmission is typically 30-80% of normally-incident intensity and bandwidths range from 3 to 50 Å. The transmission characteristics change as the filter is tilted. The shift in peak wavelength for a tilt angle of θ' is obtained using equation (3.4) and Snell's law $\mu_e \sin\theta = \sin\theta'$, where μ_e is the effective refractive index from air to the spacer medium. The shift in peak wavelength is then

$$\frac{\lambda(\theta')}{\lambda(0)} = \sqrt{1 - \frac{1}{\mu_e^2}\sin^2\theta'} \tag{3.7}$$

Therefore the shift is towards shorter wavelengths, and the relative shift is less for materials of high refractive index. The changes in transmission characteristics are illustrated in figure 3.5.

Using a filter in convergent or divergent, rather than collimated light has a similar effect on filter characteristics. The shift in wavelength of peak transmission for convergent rays is approximately half that of tilted collimated rays

ie. $\delta\,\lambda$(convergent beam, semiangle θ') $\approx \frac{1}{2}\,\delta\,\lambda$(parallel beam tilted at angle θ')

Bandwidth is increased and transmission is reduced. Beam convergence effects become significant when $\theta' > 5°$. Filters in this experiment were used in a convergent beam of semiangle $\theta' = \arctan(D/2l) = 5.1°$, which was accounted for in the original filter specification.

3.4.2 Filter calibration techniques and results

Transmission characteristics were determined with the filters in place in the instrument, as for normal observing. The equipment was set up as follows. The objective lens was completely covered and a light source introduced above one field via an optical fibre bundle (figure 3.1). The source was either white light or a neon, mercury or krypton spectral lamp, observed through a SiroSpec grating monochromator. A small coupling was used to spread the optical fibres over the exit slit of the monochromater. After passing through a light tight hole in the wall of the casing, the fibres terminated around the focal point of a lens in the light source carrier. The surface of this was depolished, so that light from the carrier was diffuse and collimated - a close approximation to an airglow source in the sky. The light source carrier was mounted over field 1, without hindering rotation of the filter wheel, so that any filter position could be used. Count rates from the detectors were monitored on a variable range analogue ratemeter and plotted on a chart recorder.

Each filter was calibrated by comparing its wavelength of peak transmission with spectral lines from a reference source having emission lines in the appropriate wavelength region. The calibration was done in a single scan of the monochromator. Scanning started at a wavelength below the reference line of shortest wavelength, with the spectral lamp illuminating the monochromator entrance slit, and no filter over field 1. After all reference lines below the filter bandpass had been traced out on the chart recording, the spectral lamp was replaced by a white light lamp, and the filter to be calibrated was moved over field 1. The filter envelope was traced out, and the original setup with the spectral lamp and no filter was returned to trace out the remaining longer wavelength reference lines. Scanning of the monochromator was uninterrupted during both changeovers. An alternative technique would be to take a separate scan of the reference lines, use this to calibrate the monochromator, and then take a scan of the filter profile. The first technique was deemed more reliable as it reduces the possibility of mechanical differences in the monochromator between scans of the reference lines and filter profile.

Scan	Nominal peak wavelength (nm)	Calibrated peak wavelength (nm)	Bandwidth (nm)	%Transmission	Reference lamp
1	630	629.9	1.37	-	neon
2	"	629.8	1.40	-	"
3	"	629.9	1.33	-	"
4	"	630.0	1.25	36	"
5	558	557.9	1.48	-	mercury
6	"	557.5	1.54	24	krypton
7	"	557.5	1.80	29	"
8	450	449	46.6	-	white

Table 3.1. Results of filter calibrations to determine wavelength of peak transmission, bandwidth, and transmitted intensity.

After obtaining a chart recording of the calibration run, filter parameters were calculated by marking the chart position of all reference peaks on an arbitrary scale. Linear regression analysis was applied to these positions and their corresponding wavelengths to obtain an expression for chart position in terms of wavelength. The peak wavelength and bandwidth of the filter envelope were then calculated from the (now calibrated) trace. The peak wavelength is the wavelength at which transmission is a maximum, and the bandwidth is the full width at half the peak height. The relative transmission of the filters was measured in selected scans. The 100% transmission level was established by including in the trace just before the filter envelope, a small section in which white light was transmitted with no filter. For calibration of the λ450 nm broadband filter, white light was used and the 0.2 nm markers of the monochromator were of sufficient accuracy to locate the peak position and width of the filter envelope.

Table 3.1 shows the results of the calibration scans. Reference lines used from each of the spectral lamps were:

Neon : 626.6, 633.4, 638.3, 640.2 nm

Mercury : 546.1, 577.0, 579.0 nm

Krypton : 549.1, 550.1, 552.0, 565.0, 567.25, 583.3, 588.0 nm

Scans 1, 2, and 5 were carried out during January 1987, before the start of the year's observations. Scans 3, 4, 6, 7 and 8 were carried out in January 1988. The state of the filters at the beginning of 1987, as determined by the calibration tests, was adequate for the experiment and no changes were necessary. Over the following year, the λ630 nm filter characteristics showed good consistency, but the λ558 nm filter drifted in peak wavelength by 0.4 nm to a shorter wavelength. However, since the drift was towards the emission wavelength (at λ557.7 nm) and the bandwidth of the filter is relatively large, the small drift of the λ558 nm filter was considered insignificant. The drift could have been due to the effects of temperature changes or ageing. The temperature shift coefficient varies with the peak wavelength of the filter; according to the manufacturer's specifications, it may vary from .015 to .040 nm $^{\circ}C^{-1}$. For this project, the operating temperature of the filters normally changed by less than 5°, so that temperature fluctuations would have only a small effect. Alternatively, filters may drift in wavelength over a time scale of years, if there are flaws in the edge seal which allow moisture penetration and hydration of the crystal lattice, and hence a change in filter characteristics.

Chapter 4

Data Analysis

4.1 Introduction

Photometer data have been recorded routinely since 1982; during 1987 data were collected by the author and are used as examples in the following discussion. Records from each emission were plotted. Most records of the λ630 nm and λ558 nm emissions showed qualitative correlation with the auroral N_2^+ emission, since the oxygen emissions are excited during auroral activity through various direct and indirect mechanisms (Gattinger et al., 1985; Rees and Roble, 1986; Solomon et al., 1988). However, the relative importance of the proposed mechanisms has not been conclusively determined, and a quantitative estimate of the auroral contribution was not possible. Instead the records were inspected for sudden, intense auroral activity which produced non-stationary data, unsuitable for further analysis. Nights which were dominated by such activity were rejected. This amounted to only about 20% of the records since the auroral activity in 1987 was relatively low, being close to the solar-cycle minimum.

Regular long-period fluctuation ($\geq$15 min) in the remaining data were tentatively interpreted as the result of gravity waves propagating through the aurorally and chemically excited λ630 nm and λ558 nm emission regions. Periodic variations in the spatial or temporal distribution of particle precipitation may sometimes produce structure in the quiet aurora which could be misinterpreted as gravity-wave activity. However, these

are not significant in the statistical analysis. The structure of pulsating auroral patches and drifting arc fragments is too short-lived and irregular to produce wavelike effects (Nakumara and Oguti, 1987).

A propagating wave induces a pattern of maxima and minima in the emission intensity which moves with the wavefronts. Therefore intensity observations measure the progression of phase fronts rather than velocity of energy propagation; these may be directed up to 90° apart in the (x, z) plane , but their projections onto the horizontal plane are coincident (Hines, 1960). The intensity records produced by the pattern of wavefronts propagating across the three fields of the photometer were decomposed into their Fourier components and the horizontal velocity of each frequency component was determined using cross-spectral analysis. Programs were developed by the author to carry out initial preparation and cross-spectral analysis of 1987 data.

4.2 Data preparation

Occasional spurious spikes were observed in the data, most likely caused by electrical interference in the photomultipliers or electronics. These were removed by interpolation between adjacent points. Each time series was then normalised by dividing by the mean of the series, to allow for the different gains of the three detectors. The mean of each series (equal to 1 after normalisation) was subtracted to remove the zero frequency, or DC component, of the spectra. A small proportion of records contained regular or irregular trends in the data, possibly due to moonlight, twilight, variations in the intensity of diffuse particle precipitation, or the passage of cloud over the field of view. Twilight effects were removed by truncating the record. Simple techniques were tested for removing trends or low frequency components from the data, in order to improve stationarity. A low order polynomial was fitted and subtracted from the data, but this method was found to be unreliable, as it introduced new frequency components in cases where a good fit was difficult. Another method was tried, using a first order

difference filter, $y_i' = y_i - y_{i-1}$, which is effectively a high-pass filter (Båth, 1974, p260). This was also found to be unsuitable as the raw data contained high-frequency auroral 'noise' which dominated the spectrum after differencing. The difference filter is more commonly used as a 'prewhitening' technique for reducing spectral leakage (Båth, 1974). Since no simple detrending method was found suitable, none was included in the data preparation. Trends in the data reduce the relative amplitude of higher frequency components, but do not change their position or phase. Therefore the presence of a trend may affect whether a frequency component is selected for analysis, but not the results of the analysis.

Next, the effect of using finite length data was considered. Each record can be regarded as an infinite record multiplied by a rectangular window of unit amplitude inside the data interval and zero amplitude outside the data interval. The Fourier transform of the record is therefore the convolution of the true spectrum (of the infinite record) and the window spectrum. The effects of this windowing are to smooth the true spectrum, and to cause spectral leakage of low frequency energy through the side lobes of the window spectrum. Smoothing the sharp edges of the rectangular window reduces the side lobes of the spectrum, and hence leakage (figure 4.1). A cosine taper was applied to the first and last 10% of data in each record for this purpose.

The Fourier transform of each record was calculated using a standard fast Fourier transform (Singleton, 1969). Because of the rotation time of the filter wheel, the observations at each wavelength, in any one of the three fields, were delayed with respect to the previous field by a time factor of $\Delta t/3$, where Δt is the sampling interval. The delay was incorporated by multiplying the Fourier transform by the appropriate phase factor given by the shift theorem (eg. Bracewell, 1978). Power spectra were calculated for the nine time series of each day.

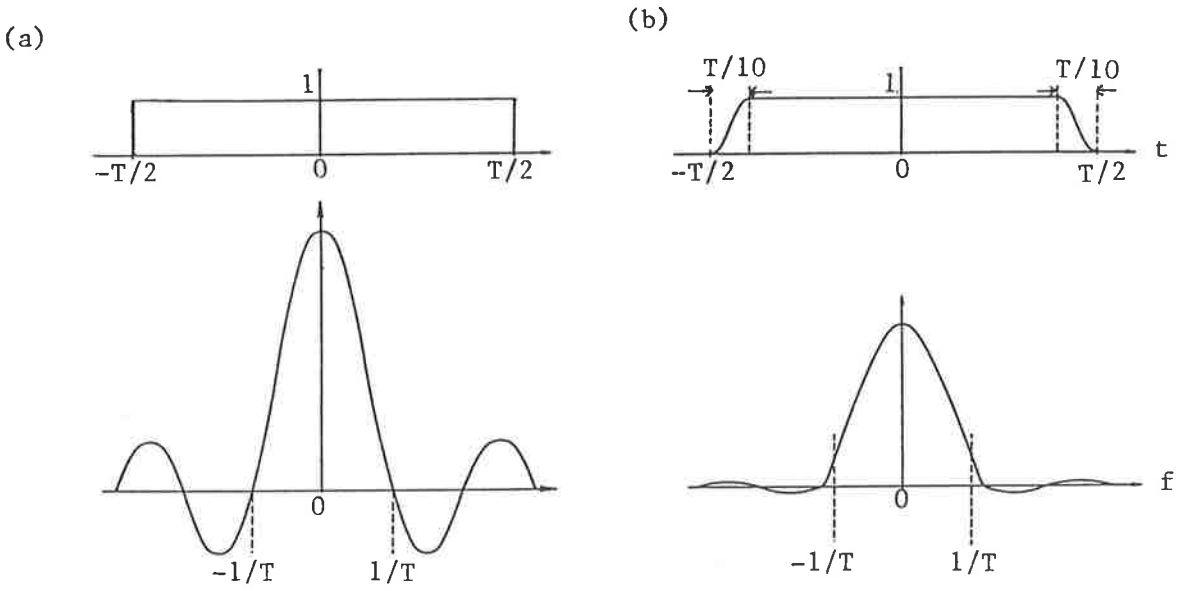

Figure 4.1. An example of the reduction in spectral leakage obtained by choosing an appropriate data window (adapted from Bendat and Piersol, 1971) .
(a) rectangular window and its Fourier transform
(b) cosine tapered window and its Fourier transform.

4.3 Cross-spectral analysis

The correlation between two continuous finite-length time series $x_m(t)$ and $x_n(t)$ as a function of time lag τ, can be examined in the time domain through the cross-covariance function defined (for record length T) as

$$ccf(\tau) = \frac{1}{T-\tau} \int_0^{T-\tau} x_m(t)\, x_n(t+\tau)\, dt \tag{4.1}$$

To investigate the correlation between time series as a function of frequency, cross-spectral analysis is used. The technique is described in Bendat and Piersol (1971, p333) and Jenkins and Watts (1969, p363). The Fourier transform of the continuous finite record $x_m(t)$ is

$$X_m(f) = \int_0^T x_m(t)\, e^{-i2\pi ft}\, dt \tag{4.2}$$

and the inverse Fourier transform is

$$x_m(t) = \int_{-\infty}^{\infty} X_m(f)\, e^{i2\pi ft}\, df \tag{4.3}$$

Using equation (4.3), the shift theorem, and assuming τ is small, equation (4.1) may be written as

$$\begin{aligned} ccf(\tau) &= \frac{1}{T}\int_0^T x_m(t)\left(\int_{-\infty}^{\infty} e^{i2\pi f\tau}\, X_n(f)\, e^{i2\pi ft}\, df\right) dt \\ &= \frac{1}{T}\int_{-\infty}^{\infty} e^{i2\pi f\tau}\, X_n(f)\left(\int_0^T x_m(t)\, e^{i2\pi ft}\, dt\right) df \\ &= \frac{1}{T}\int_{-\infty}^{\infty} e^{i2\pi f\tau}\, X_n(f)\, X_m(-f)\, df \\ &= \frac{1}{T}\int_{-\infty}^{\infty} X_m^*(f)\, X_n(f)\, e^{i2\pi f\tau}\, df \end{aligned} \tag{4.4}$$

since $X_m(-f) = X_m^*(f)$ for the Fourier transform of a real function. Therefore the function $G_{mn}(f) = X_m^*(f)X_n(f)\ /T$ is the Fourier transform of the cross-covariance function. $G_{mn}(f)$ is called the cross-power spectrum; it may be split into its real part (cospectrum) and imaginary part (quadrature spectrum).

$$G_{mn}(f) = X_m^*(f)\, X_n(f)\ /T = C_{mn}(f) - i\, Q_{mn}(f) \tag{4.5}$$

By writing $X_m(f) = a_m(f) - ib_m(f)$, and substituting into equation (4.5) it can be shown that the cospectrum,

$$C_{mn}(f) = [a_m(f)\, a_n(f) + b_m(f)\, b_n(f)]\ /T \tag{4.6}$$

and the quadrature spectrum,

$$Q_{mn}(f) = [a_m(f)\, b_n(f) - a_n(f)\, b_m(f)]\ /T \tag{4.7}$$

Alternatively, by writing $X_m(f) = |X_m(f)|e^{i\Phi_m(f)}$ and substituting into equation (4.5), the cross power spectrum can be written in complex polar form,

$$G_{mn}(f) = |X_m(f)||X_n(f)|e^{i[\Phi_n(f)-\Phi_m(f)]} = A_{mn}(f)\, e^{-i\Phi_{mn}(f)} \tag{4.8}$$

where the cross amplitude spectrum $A_{mn}(f)$, is

$$A_{mn}(f) = |X_m(f)||X_n(f)| = [C_{mn}^2(f) + Q_{mn}^2(f)]^{\frac{1}{2}} \tag{4.9}$$

and the phase spectrum, $\Phi_{mn}(f)$, is

$$\Phi_{mn}(f) = \Phi_m(f) - \Phi_n(f) = \arctan\left(\frac{Q_{mn}(f)}{C_{mn}(f)}\right) \tag{4.10}$$

The cross-amplitude spectrum measures the combined power of both records as a function of frequency. The phase spectrum measures the phase difference between the records as a function of frequency; with the definition given in equation (4.10), $\Phi_{mn}(f) > 0$ when record m leads record n.

A quantity used in estimation of uncertainties of the spectral parameters is the squared coherency spectrum, $K^2_{mn}(f)$, defined as

$$K^2_{mn}(f) = \frac{A^2_{mn}(f)}{G_{mm}(f)\ G_{nn}(f)} \tag{4.11}$$

It is a measure of the correlation between the two time series which is independent of the scale of measurement of $x_m(t)$ and $x_n(t)$ (unlike $A_{mn}(f)$). It is analogous to the correlation coefficient in cross-correlation analysis. The discussion above refers to analysis of stochastic time series using a Fourier transform approach, which necessarily implies a finite record length. In this case, raw estimates of spectral parameters are made with ν=2 degrees of freedom, and the estimate of $K^2_{mn}(f)$ is equal to 1, regardless of the magnitude of the correlation between the two time series. In the cross correlation analogy, a perfect correlation can always be obtained for any two pairs of points $[x_m(t_1), x_n(t_1)]$ and $[x_m(t_2), x_n(t_2)]$ (Bendat and Piersol, 1971, p195). Therefore, the cross spectrum must always be smoothed over some frequency interval, but at the expense of resolution in the estimate.

4.4 Estimates of horizontal phase trace speed and propagation azimuth

Cross spectral analysis was applied to the time series from the three fields of the photometer, taking pairs of fields cyclically. Spectral estimates were obtained at discrete frequency intervals, $f_i = \frac{i}{T}$, $i = 1..\frac{N}{2}$, giving a frequency resolution of $\frac{1}{T}$, where T is the data length and N is the number of data points. The estimates of co-spectrum and quadrature spectrum were smoothed over three frequency components, and the smoothed estimates used to calculate the cross amplitude and phase spectra. From the

smoothed phase spectrum, the time difference between two fields is given by

$$\tau_{mn}(f_i) = \frac{\bar{\Phi}_{mn}(f_i)}{2\pi f_i} \tag{4.12}$$

where the overbar denotes the smoothed estimate. The speed with which a wavefront appears to move from field m to n is the apparent speed, given by

$$v_{mn}(f_i) = \frac{S}{\tau_{mn}(f_i)} = \frac{2\pi f_i S}{\bar{\Phi}_{mn}(f_i)} \tag{4.13}$$

where S is the separation of the fields at the height of observation. This definition of apparents speeds is illustrated in figure 4.2a. For a wavefront travelling with velocity $\mathbf{v}$ as shown, v_{23} and v_{31} are positive but v_{12} is negative. The velocity of the wavefront in the horizontal plane is represented by the perpendicular from the origin to the line of best fit through the end points of the vectors constructed from the 3 apparent speeds (figure 4.2b). This is the horizontal phase trace velocity. If $y = a + bx$ is the line of best fit, the horizontal trace velocity of the wavefront is given by

$$\mathbf{v} = (v, \theta) = \left(\sqrt{\frac{a^2}{1+b^2}}, \arctan(-b) \right) \tag{4.14}$$

v is the horizontal phase trace speed and θ is the azimuth of phase progression (or equivalently, of energy propagation as discussed in section 2.2.3).

Horizontal trace speed and propagation azimuth were calculated for periodicities which contained significant power in all three fields, that is, greater than 10% of the maximum in the given spectrum (usually found in the fundamental component). The selected periodicities were also required to have a mean coherence over the three fields of greater than 0.8. Further points were rejected if the observed parameters did not conform to the dispersion relation for gravity waves ie. k_z^2 was calculated to be less than 0; this eliminated points for which $v_{px} > c$ and $\omega_b < \omega < \omega_a$.

4.5 Uncertainty in speed and azimuth estimates

The estimates of speed and azimuth are subject to uncertainties which arise because of the limitations of the measurement and analysis techniques. Firstly, each intensity measurement is finite and hence subject to statistical uncertainty; this is relatively small

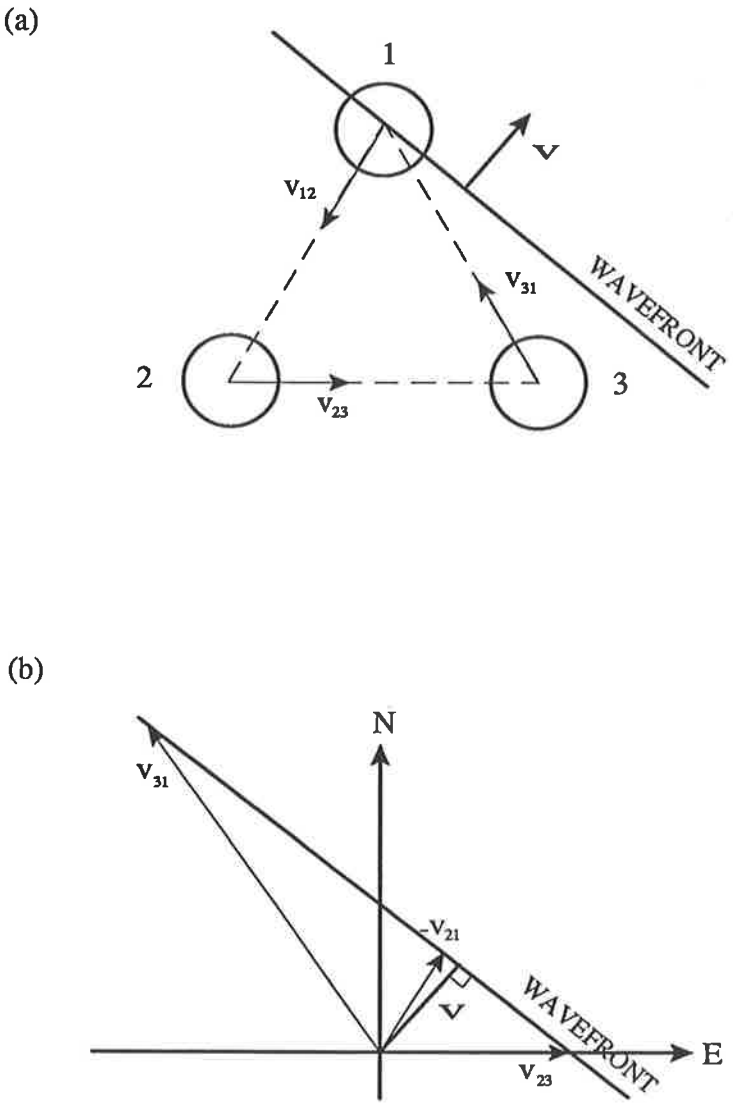

Figure 4.2.
(a) Three apparent speeds of a wavefront travelling in the direction indicated by **v**; v_{23} and v_{31} are positive, v_{12} is negative.
(b) The horizontal phase trace velocity of the wavefront, **v**, is calculated by constructing vectors from the 3 apparent speeds and obtaining the perpendicular to the line of best fit through the vector endpoints.

because of the high counts level. Secondly, the finite data length restricts the resolution with which the period of waves can be estimated. As a result, the analysis produces an unavoidable error by attempting to describe with discrete frequency components, functions composed of a continuous range of frequencies. Data simulations were used to investigate these forms of error, and were compared with uncertainties derived from an analytical expression.

4.5.1 Estimation of uncertainties using data simulations

Initially, simulated data were used to test the complete analysis routine. Three time series were generated by adding a number of sinusoidal waveforms of specified period, speed, and azimuth of propagation. Relative phase shifts between the three series were determined from the speed and azimuth of each wave. Noise was added using random numbers from a uniform distribution, to simulate irregular fluctuations - different in each field - caused, for example, by localised particle precipitation. This time-series simulation does not completely represent real data, since gravity waves occur in groups extending over a frequency range, rather than as single monochromatic waves. However the simulation allows testing of the errors introduced by the analysis procedure.

Estimated spectra have a frequency resolution of $\frac{1}{T}$ where T is the data length. Initially, simulated waves were chosen with periods corresponding exactly to frequency components, $\frac{i}{T}$, $i = 1..\frac{N}{2}$, of the estimated spectra. The differences between the speeds and azimuths used in constructing the simulations, and the estimates produced by the analysis, were evaluated as percentage errors. The accuracy of estimates varied from 1% to 20% depending on the speed and wavelength relative to the field spacing. Typically, the speed estimates were within 10% of the specified speed, and the estimates of propagation azimuth were correct to 5°. When simulated wave periods fell between frequency components of the estimated spectra, the error increased slightly, sometimes significantly at low frequencies. For example, from a data length of 480 min, spectral estimates occur at frequencies corresponding to periods of 480, 240, 160, 120, 96 min

etc. In an extreme case, the error in the speed estimate increased from 9% to 33% when the wave period was changed from 96 min to 105 min. The error in the azimuth estimate remained constant at 4°. These figures are merely illustrative, as the error is strongly dependent on wave parameters and the presence of other waves. In general, propagation azimuths were estimated more accurately than trace speeds.

A further problem (mentioned briefly in Hines, 1974) occurs if two waves of similar frequencies, but different propagation directions, are recorded in the data - the analysis is unable to identify the waves separately. Results of simulations indicate that if the wave directions are separated by less than about 90° the analysis produces an intermediate speed and azimuth value. Widely separated wave directions produce meaningless results. It is unlikely that the current data is seriously affected by this problem, as analyses of individual nights show azimuths generally confined to within approximately 90° over a range of frequencies. This behaviour would be expected for waves generated by sources within the auroral electrojet, which occur over a limited range of bearings from Mawson.

4.5.2 Analytical estimation of uncertainties

An analytical expression for the uncertainty in speed and azimuth estimates can be obtained by tracing the propagation of uncertainties through the analysis procedure. For example, Freund and Jacka (1979) determined the drift velocity of patterns in airglow using cross-correlation analysis between four observing fields. The mean uncertainty in the drift speed v, was estimated by assuming the total signal in field m was a sinusoidal variation of period T and with time shift t_m, superimposed on a mean signal N_0. The apparent velocity between two fields v_{mn}, is a function of $t_m - t_n$. Therefore, using the expression for variance σ^2, of a multivariate function $h(x_1..x_N)$ (from Bevington, 1969, p60)

$$\sigma^2(h) = \sum_{i=1}^{N} \left(\frac{\partial h}{\partial x_i} \right)^2 \sigma^2(x_i) \qquad (4.15)$$

and assuming a Poisson distribution in the noise of the signal, Freund and Jacka (1979) derived an expression for $\sigma^2(v_{mn})$, and hence $\sigma^2(v)$, in terms of N_0 and T.

Describing the uncertainties in cross spectral estimates requires a rather more sophisticated approach since the technique estimates spectrally separated parameters rather than drift parameters of the pattern as a whole. Jenkins and Watts (1969, p379) discuss the derivation of error estimates for cross-spectral parameters. The mean square error of an estimate is made up of the variance term which describes the random portion of the error, and the square of the bias term which describes the systematic portion of the error. The variance of the cross-spectrum estimate is suppressed by using a large smoothing bandwidth, but the bias error is reduced with a small bandwidth; the minimum uncertainty is obtained at a compromise in the choice of smoothing bandwidth. For the analysis described in section 4.3, a relatively small smoothing interval was used to maintain good spectral resolution, so that the largest error is expected to occur in the variance.

An expression for the variance of the smoothed phase-spectrum estimate is given by Jenkins and Watts (1969, p379) as,

$$\sigma^2(\bar{\Phi}_{mn}) \approx \frac{1}{\nu}\left(\frac{1}{\bar{K}_{mn}^{\,2}} - 1\right) \tag{4.16}$$

where ν is the number of degrees of freedom in the estimate; ν is twice the number of frequency components used in the smoothing. The frequency dependence is omitted for clarity. An expression for the variance of the apparent speed estimate is obtained by using equation (4.15) on (4.13) to give

$$\frac{\sigma^2(v_{mn})}{v_{mn}^2} = \frac{\sigma^2(\bar{\Phi}_{mn})}{\bar{\Phi}_{mn}^2} \tag{4.17}$$

When obtaining a line of best fit, $y = a + bx$, through the vectors constructed from the three apparent speeds, they are weighted according to their standard deviations (from equation 4.17). A linear regression routine from Bevington (1969, p104) was used. The variances in a and b are then

$$\sigma^2(a) \approx \frac{1}{\Delta}\sum_{i=1}^{3}\frac{x_i^2}{\sigma_i^2} \tag{4.18}$$

$$\sigma^2(b) \approx \frac{1}{\Delta} \sum_{i=1}^{3} \frac{1}{\sigma_i^2}$$

where $$\Delta = \sum_{i=1}^{3} \frac{1}{\sigma_i^2} \sum_{i=1}^{3} \frac{x_i^2}{\sigma_i^2} - \left(\sum_{i=1}^{3} \frac{x_i}{\sigma_i^2} \right)^2$$

$x_i,\ y_i$ = components of the vectors constructed from the apparent speeds

σ_i = $\sigma(v_{mn})$, the standard deviation in the apparent speed estimates

Expressions for the uncertainty in the trace speed and azimuth are obtained using equation (4.15) with (4.14),

$$\frac{\sigma^2(v)}{v^2} = \frac{1}{a^2}\,\sigma^2(a) + \frac{b^2}{(b^2+1)^2}\,\sigma^2(b) \tag{4.19}$$

$$\sigma^2(\theta) = \cos^4\theta\ \sigma^2(b)$$

Equations (4.16), (4.17), (4.18), and (4.19) were evaluated in that order to obtain an estimate of the uncertainty in the horizontal phase trace speed and propagation azimuth.

These expressions were evaluated for the simulations described in section 4.5.1. The estimated uncertainties were generally in agreement with the errors in the analysis results. Thus the analytical expression provides a good estimate of the uncertainty for simulated data where the coherency is consistently high. The uncertainty estimate may be less reliable when using real data, for the following reason. The uncertainty in the phase spectrum estimate (equation 4.16) is very sensitive to the value of K_{mn}^2. Jenkins and Watts (1969) used the theoretical value of K_{mn}^2 but since this is unknown, the estimated value (equation 4.11) is used. The estimated coherency is also subject to uncertainty, especially for small smoothing intervals, and more variable for real data. Therefore spurious uncertainty estimates are possible.

Uncertainties were estimated for all results produced by the analysis, for both emissions. Figures 4.3a and 4.3b show the distributions of percentage uncertainties in the estimated trace speeds, and figures 4.3c and 4.3d show the distribution of uncertainties

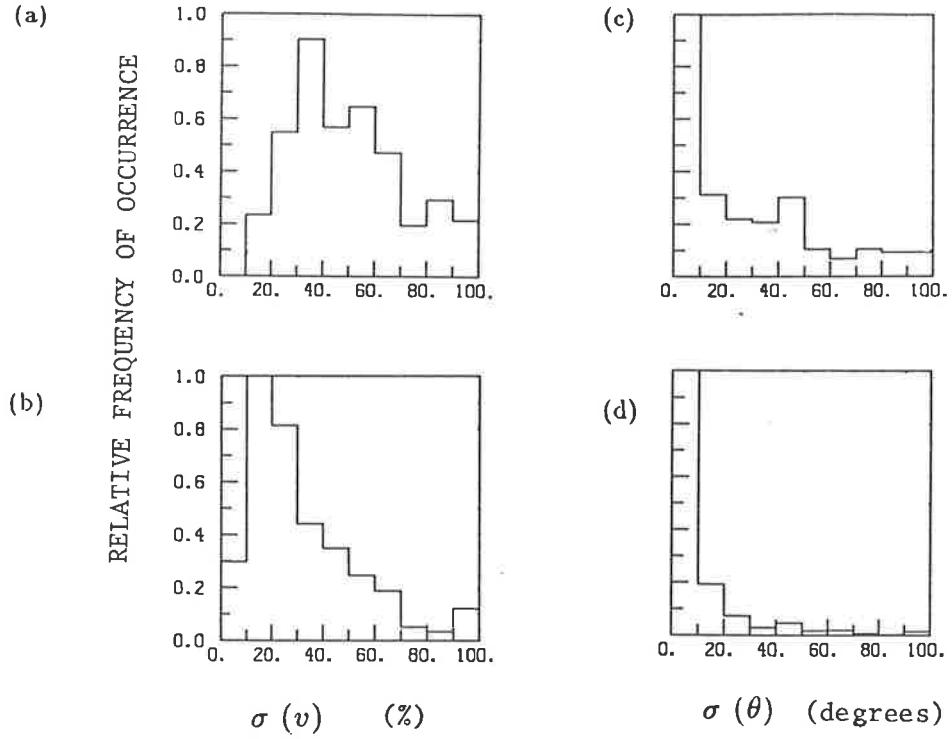

Figure 4.3. Distributions of uncertainties in the speed and azimuth estimates. Uncertainties in the speed estimates are represented as percentage errors for (a) results from the λ630 nm data (b) results from the λ558 nm data. Uncertainties in the azimuth estimates are given in degrees for (c) results from the λ630 nm data (d) results from the λ558 nm data.

in the propagation azimuths in degrees. The median uncertainties in speed estimates are around 40% and 25% for waves in the λ630 nm and λ558 nm emissions, respectively. The estimated uncertainties are not low, but adequate for their purpose in interpretation of the results - the main focus of discussion is on the propagation azimuths. The estimated uncertainties in propagation azimuths were less than about 15° for the majority of waves in both emissions.

4.5.3 The effect of auroral noise

Further uncertainty in the results may arise from a completely different source. Bursts of auroral activity, being impulsive, contain a range of frequency components, possibly including those of interest in the gravity wave range. Thus spurious high power may contaminate some frequency components. Although data with excessive activity of this sort is rejected, the majority of records contain some auroral activity. In these records,

the distinction between sporadic auroral activity and wave-induced fluctuations is not well defined, so no attempt was made to remove this contamination or to quantify the uncertainty. It is expected that the analysis rejects most results produced from auroral activity because of lack of coherence between all fields, or because of high speed estimates resulting from simultaneous signals in all fields.

Chapter 5

Results: Wave Characteristics

Data were recorded during the autumn, winter and spring months of March to October. During 1987, data were collected on a total of 129 nights, on which cloud cover was less than $\frac{2}{8}$. The hours of observation were between evening and morning twilight; around midwinter this was typically 15 to 01 UT (for reference, 00 UT = 04.2 LT, local time, and 00 UT = 01.7 MLT, magnetic local time). An example of the λ630 nm intensity variations as measured in the three fields is shown in figure 5.1; for this figure, data were prefiltered to remove frequencies higher than the Brunt-Väisälä frequency ($\tau_b \approx 12$ min at 220 km). The records show evidence of wavelike perturbations, with significant correlation between the fields.

An example of the raw power spectra obtained from the unfiltered data is shown in figure 5.2. Power is in arbitrary units of intensity^2 Hz^{-1}, where intensity is proportional to the number of counts. A number of maxima are visible in the 15 to 180 min period range.

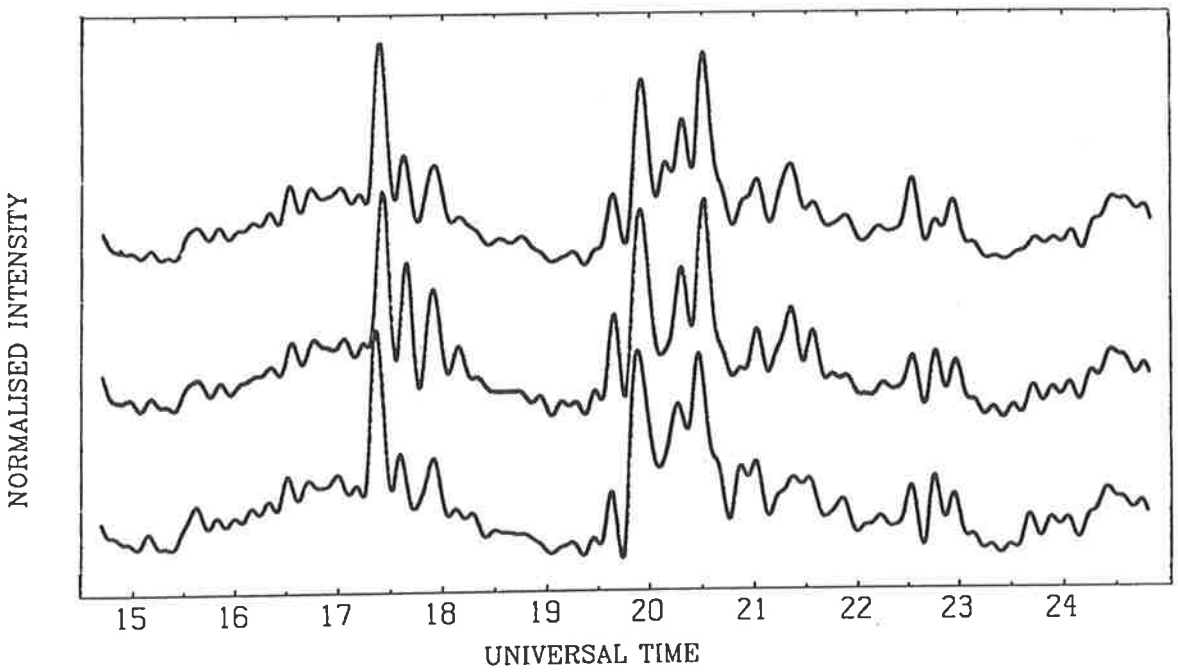

Figure 5.1. An example of normalised λ630 nm data from three fields of view. Data have been prefiltered to remove frequencies higher than the Brunt-Väisälä frequency.

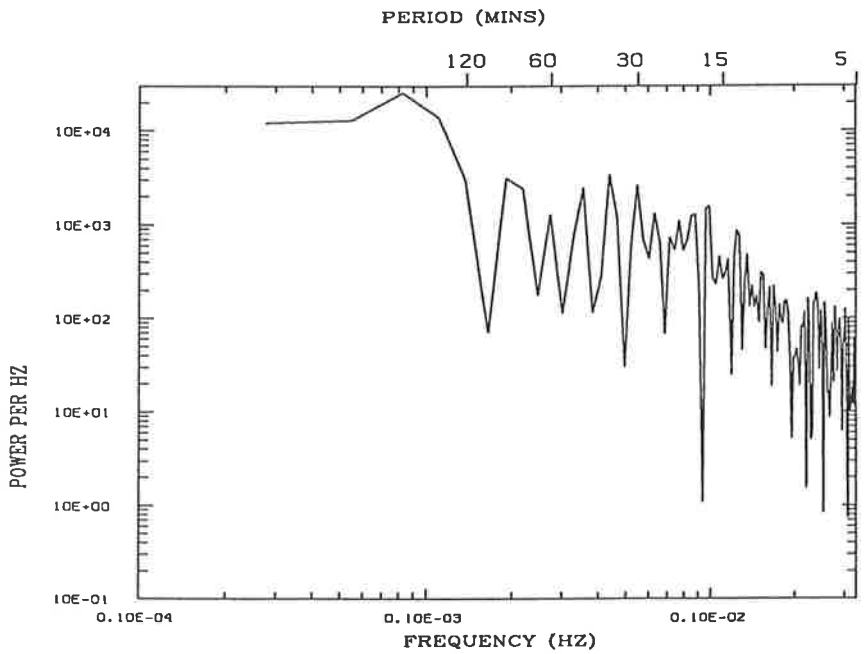

Figure 5.2. Raw power spectrum obtained from one field of the λ630 nm data shown in figure 5.1, before filtering.

5.1 Period, speed and azimuth distributions for 1987

Cross spectral analysis of the λ630 nm and λ558 nm data yielded perturbations with periods ranging from 5 min to 4 h, limited by the Brunt-Väisälä period and the length of the data set. However, few perturbations of periods less than about 20 min contained significant power. Distributions of wave parameters were evaluated for perturbations selected by the analysis. Figure 5.3 shows, for both emissions, the relative frequency distributions of wave period, horizontal phase trace speed, and propagation azimuth. These show observed rather than intrinsic parameters, as no concurrent measurement of the mean wind was made. The following points are made about the distributions for the λ630 nm emission:

1. The majority of waves fall in the period range 30 min to 3 h.
2. Trace speeds are asymmetrically distributed around a median of about 300 ms^{-1}. Around 20% of points produced by the analysis have high speed values (>700 ms^{-1}), but since they were required to satisfy the dispersion relation, those with speeds greater than the speed of sound (~690 ms^{-1} at the λ630 nm emission height) were rejected.
3. The direction of propagation of the waves is highly polarised, the predominant direction being around geographic northwest.

The main features of the λ558 nm distributions are

1. The overall number of waves is greater than that of the λ630 nm emission, and the typical period is shorter; around 75% of waves are in the period range 10-90 min.
2. Horizontal trace speeds are fairly smoothly (but asymmetrically) distributed around a lower median value of 100-150 ms^{-1} with a cutoff at ~330 ms^{-1}, the speed of sound at the λ558 nm emission height.
3. The direction of propagation of the waves is again highly polarised, the predominant direction here being around geographic east-northeast.

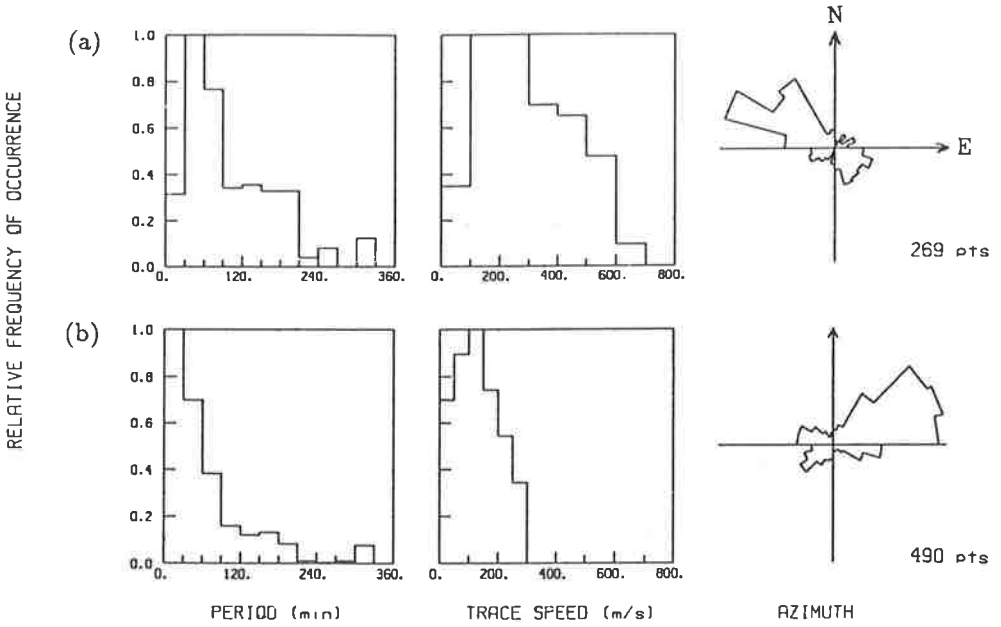

Figure 5.3. Distributions showing relative frequency of occurrence of wave period, horizontal trace speed, and propagation azimuth (in geographic coordinates) for Mawson 1987 data. (a) Waves in the λ630 nm emission. (b) Waves in the λ558 nm emission. The total number of points in each data set is shown in the bottom right corners.

The period and trace speed distributions of the waves in the λ630 nm emission suggest that most fall into the class of large-scale (LS) waves, and those in the λ558 nm emission fall into the class of medium-scale (MS) waves, as characterised by Georges (1968). Short-period (MS) waves are more easily generated than long-period (LS) waves, and hence are more numerous (Francis, 1975). The reduction in short-period low-speed waves in the λ630 nm distributions as compared with the λ558 nm distributions is consistent with dissipation due to molecular viscosity, thermal conduction, and ion drag, which increases significantly in the F region (figure 2.4). Since the λ630 nm emission is located further from a presumed source region in the auroral electrojet, dissipation effects are more pronounced. It will be shown in the following section that the period and speed distributions of waves in both emissions in 1987, are typical for the years 1982 to 1989, but that the azimuth distribution of waves in the λ558 nm emission is not. The change in azimuth distributions is investigated further in the following chapter.

As pointed out in section 2.2.3, the trace speed determined from the analysis describes the horizontal motion of the wavefront. The phase speed and wavelength in the (x, z)

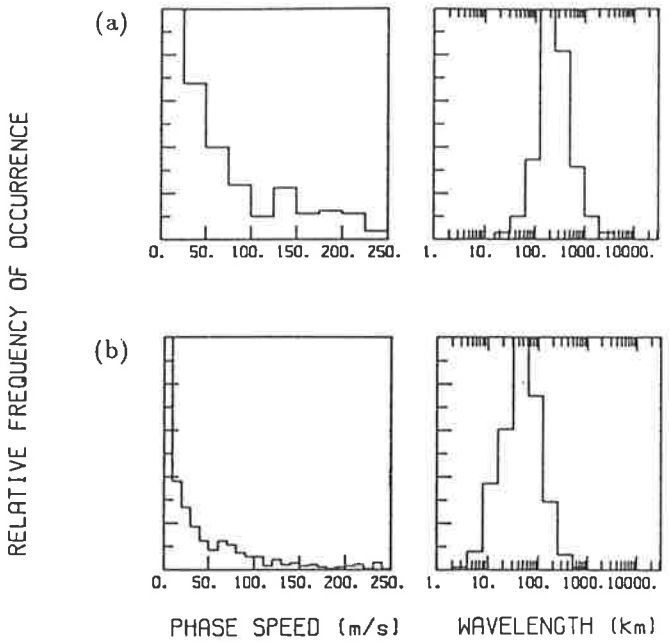

Figure 5.4. Distributions showing relative frequency of occurrence of phase speed and wavelength in the (x, z) plane, calculated for the data in figure 5.3 (Mawson, 1987). (a) Waves in the λ630 nm emission. (b) Waves in the λ558 nm emission.

plane were examined. The vertical wave number was calculated using the dispersion equation (2.22), and the phase speed $|\mathbf{v_p}|$, and wavelength λ, were derived from equations (2.15) and (2.17). Figure 5.4 shows the relative frequency distribution of phase speeds and wavelengths obtained from the data in figure 5.3. The phase speed distributions are more closely clustered about zero than the trace speed distributions. This is the result of the predominantly vertical phase progression of low frequency waves; even low-phase-speed waves will be observed with relatively high horizontal trace speeds. The wavelength distributions range from about 100 to 1000 km and 10 to 200 km for the waves in the λ630 nm and λ558 nm emissions, respectively. This supports the classification of waves in the λ630 nm and λ558 nm emissions as predominantly LS and MS waves, respectively.

5.2 Comparison of wave scales with other observations

The periods and horizontal trace speed calculated from the 1987 observations were compared with others reported in the literature (a comparison of propagation azimuths is presented later in this chapter).

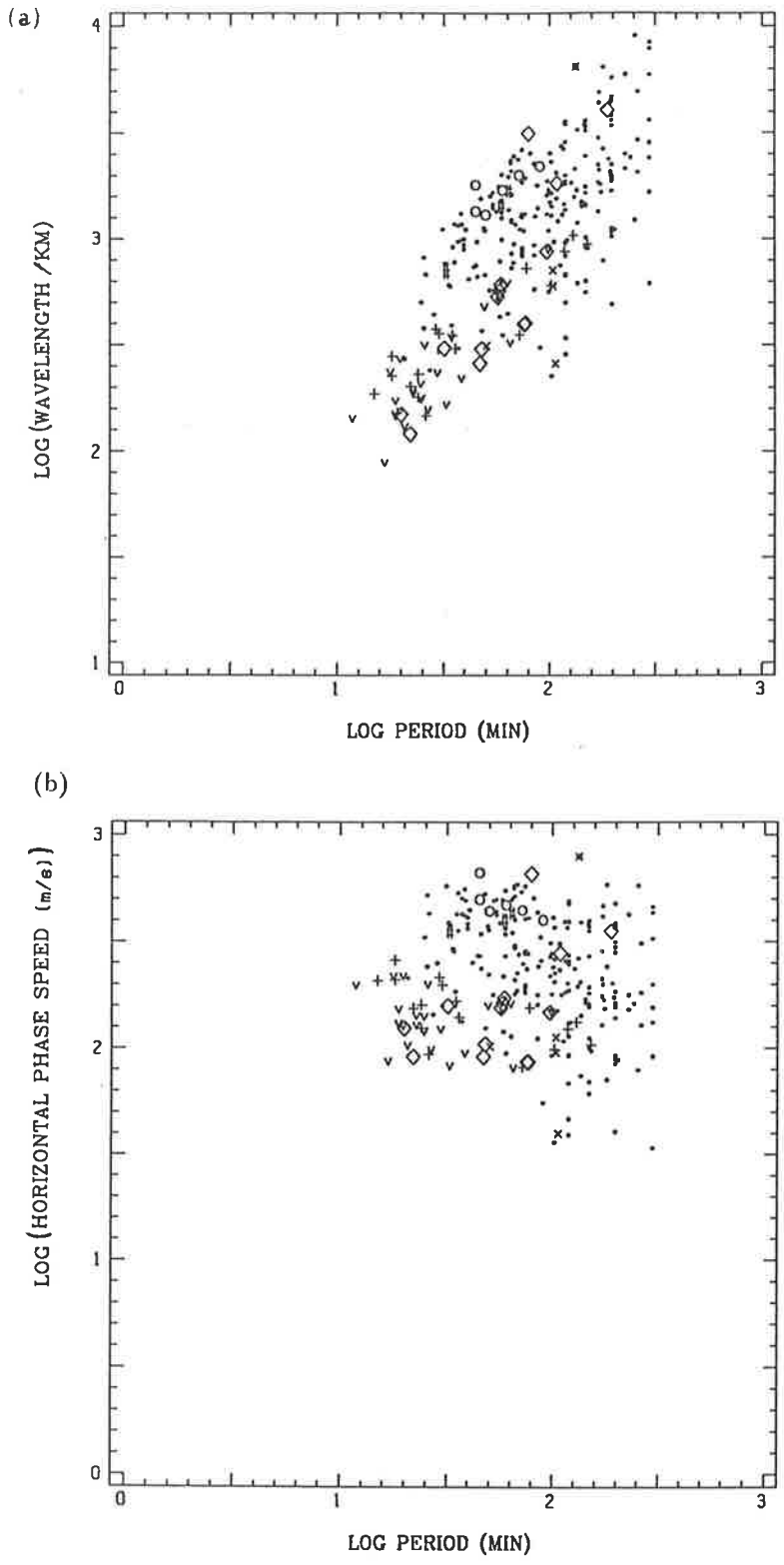

o	Chan and Villard	1962	×	Tedd and Morgan (from 220 km altitude)	1985
+	Hunsucker and Tveten	1967			
V	Davies and Jones	1971	*	Hajkowicz and Hunsucker	1987
◇	Bertin et al.	1975, 1983	#	Williams et al	1988

Figure 5.5. Collation of gravity wave parameters from TID measurements in the F region. The small dots are the Mawson 1987 data, from the λ630 nm emission. (a) Horizontal wavelength versus period (b) Horizontal trace speed versus period The axes were made equivalent to those of figure 5.6 for ease of reference.

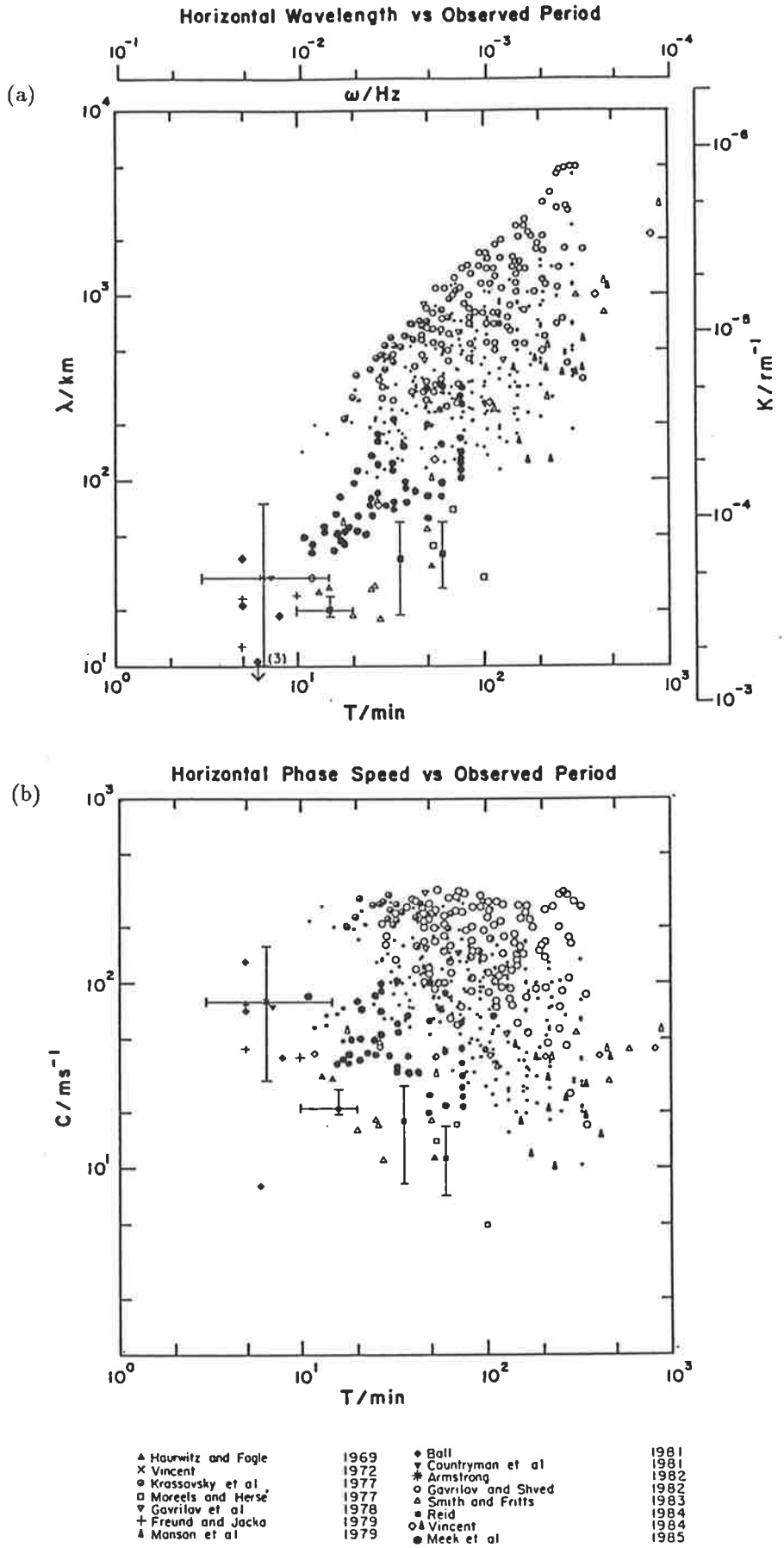

Figure 5.6. Collation of measurements of gravity wave parameters for altitudes of 60-110 km (adapted from Reid, 1986). The small dots are the superimposed Mawson 1987 data, from the λ558 nm emission.
(a) Horizontal wavelength versus period (b) Horizontal trace speed versus period

A number of F-region TID observations were collated by the author and presented with the Mawson λ630 nm data (figure 5.5). Figure 5.5a shows horizontal wavelength against observed period, and figure 5.5b shows horizontal phase (trace) speed against period. The Mawson data show a spread of values similar to that of the collated data, with a tendency towards larger periods and scales. This may be due in part to the bias of the observing technique. The integrated intensity of the emission layer is the measured parameter, so that the relative amplitude of fluctuations produced by waves with a vertical wavelength of less than the half-width of the emission layer, will be much reduced. The half-width of the λ630 nm emission layer is approximately 20 to 40 km; if this defines the minimum observed vertical wavelength, the corresponding minimum horizontal wavelength (according to the dispersion equation) for a period of, say, 100 min is about 170 to 300 km. This is approximately the lower limit of the range of observed horizontal wavelengths (figure 5.5a).

The λ558 nm results were superimposed on measurements from the 60-110 km height region, collated by Reid (1986) (figure 5.6). The Mawson 1987 data cover a range of values similar to those observed with a number of optical techniques, eg. OH airglow observations (Krassovsky et al., 1977), OI λ558 nm airglow observations (Gavrilov and Shved, 1982; Gavrilov et al, 1978), and combined OH infrared and OI λ558 nm airglow studies (Armstrong, 1982). There is some overlap with the radar observations of Manson et al. (1985), Meek et al. (1985), and Vincent (1984).

5.3 The dispersion diagram

The relationship between period and horizontal and vertical wave numbers is illustrated in the dispersion diagrams of figure 5.7, which also show the theoretical limits on gravity wave modes. The instrument limit defines waves which have a horizontal wavelength less than twice the spacing of the fields at the observing height. The dissipation and reflection limits were discussed in sections 2.3.2 and 2.3.3. The reflection region was estimated to be at approximately 85 km altitude, and the condition of re-

(a)

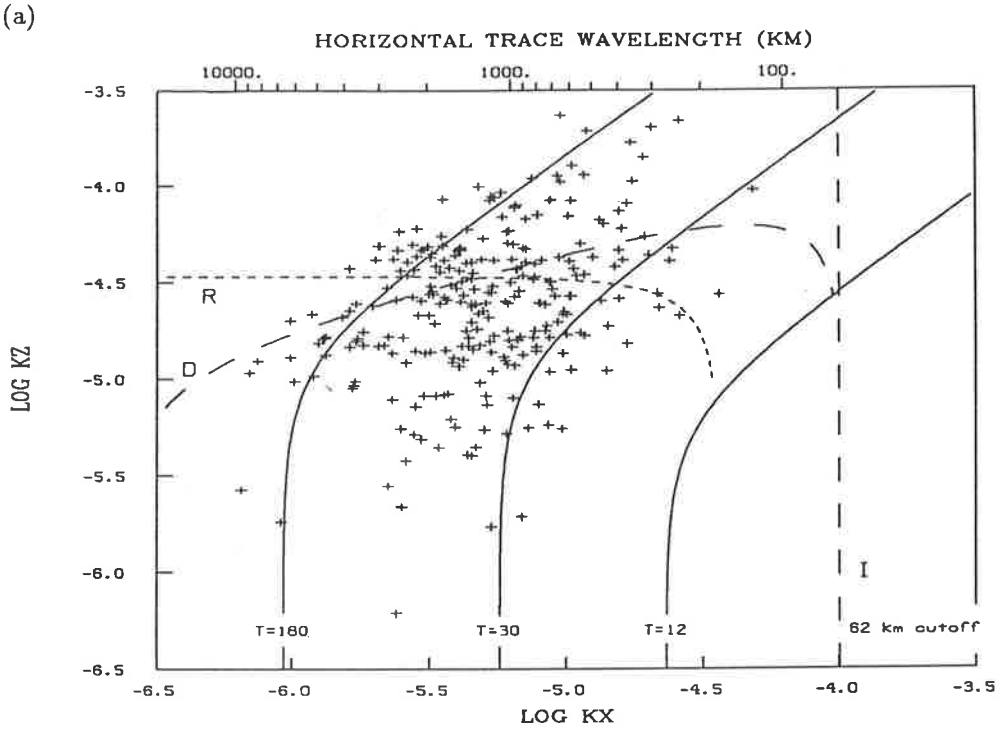

(b)

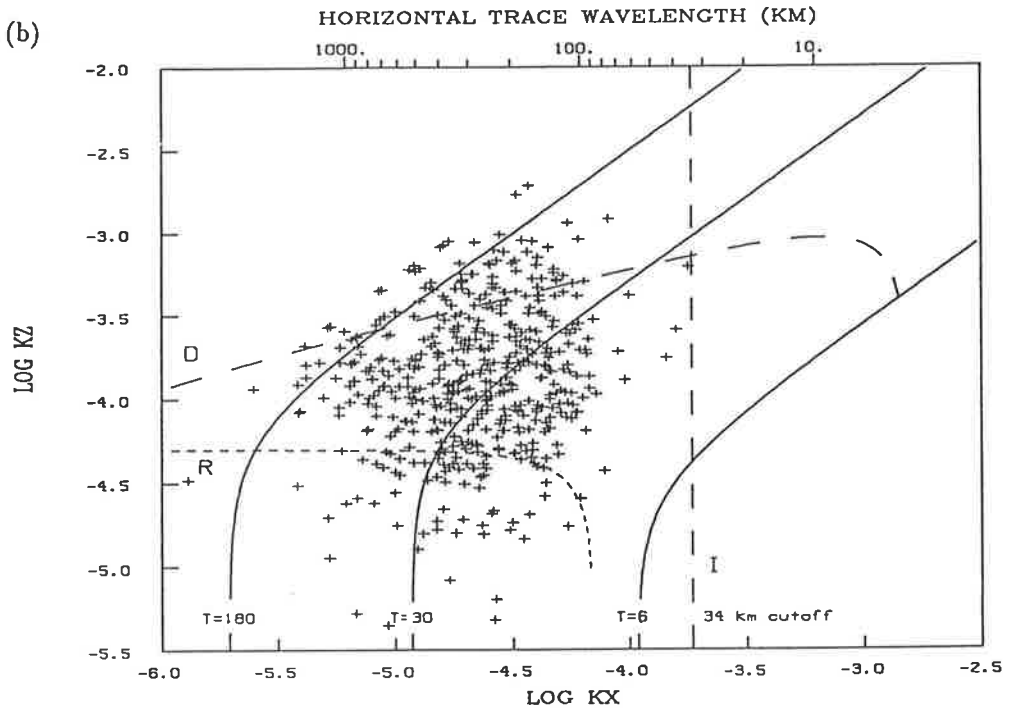

Figure 5.7. Dispersion diagram showing wave parameters derived from observed period and horizontal trace speed, for the Mawson 1987 data. Dissipation (D) and instrument (I) limits are shown as dashed lines; the reflection limit (R) is shown as a dotted line. (a) Waves in the λ630 nm emission. (b) Waves in the λ558 nm emission.

flection was shown to be equivalent to an upper limit on the horizontal trace speed of about 230 ms^{-1}, for waves propagating from the troposphere. Therefore the high speed waves in the trace speed distributions (figure 5.3) can be attributed to a thermospheric source. The dispersion diagram for the λ630 nm data shows a large proportion of points which fall into this category (below the reflection limit on the dispersion diagram, figure 5.7) as would be expected if a large proportion of waves in the λ630 nm emission are generated in the thermosphere. A smaller proportion of points in the λ558 nm data fall into this category. The points above the reflection limit were found to have true phase speeds ranging from 0 to 100 ms^{-1}, which is consistent with the magnitude of tropospheric winds which are thought to generate gravity waves.

It has been implied that all waves propagating from the troposphere which exceed the limit will be reflected. However, some waves may penetrate the reflection region if it does not persist for more than half a wavelength (section 2.3.2).

A substantial proportion of points in both diagrams lie above the dissipation limit. Observations of TIDs at mid-latitudes indicate that LS waves of this type are not uncommon in the F region (eg. Tedd and Morgan, 1985), whereas the limit shown in figure 5.7 suggests that they should be dissipated. However, as discussed in section 2.3.3, the calculations of Hickey and Cole (1988) indicate that the simplified model on which this limit is based, overestimates dissipation rates in the middle thermosphere. In addition, the position of the points on the dispersion diagram may be significantly changed if the intrinsic parameters, which correctly describe the physical behaviour of the waves, rather than the observed parameters, are used. Since the horizontal wave number k_x, is invariant, use of intrinsic values will move the points up or down on the dispersion diagram. Attempts were made to estimate intrinsic values using modelled winds, but this still yielded some points located above the dissipation limit. The model winds show significant variations with time and with geomagnetic activity (discussed in the following chapter) and it was concluded that estimation of intrinsic parameters was not useful without better temporal resolution in the analysis.

5.4 Results from 1982 to 1989

Photometer data from 1982 to 1989 were examined for similar wave characteristics. A more compact analysis was used to process this large quantity of data; only the three most dominant peaks in the power spectra (rather than all the significant peaks) were selected for cross spectral analysis. The results of analysis for both emissions are presented in figures 5.8 and 5.9 as frequency distributions of observed period, phase speed, wavelength, and propagation azimuth. There is little difference in the period, phase speed, and wavelength distributions from year to year. The propagation azimuths of waves in the λ630 nm emission exhibit a well-defined consistent polarisation towards the northwest to west, but the propagation azimuth of waves in the λ558 nm emission changes significantly.

During 1982 and 1983, the propagation azimuths of waves in the λ558 nm emission tend towards the northwest and southeast. During 1984 the distribution is somewhat different - a small proportion remain in the northwest, but the majority of waves propagate towards the northeast. From 1985 to 1987 waves propagating towards the east to northeast dominate. During 1988 and 1989 the distributions resemble those of 1982 and 1983. (The slightly rotated distribution of 1989 may be related to the limited period over which data were analysed, ie. 10 April to 24 July).

The variation in propagation azimuths of waves in the λ558 nm emission strongly suggests a solar-cycle dependency, tending to follow the recent cycle phases of maximum (1979), minimum (1986), and predicted maximum (1989/90). To illustrate the point, waves were grouped as shown in figure 5.10, according to the daily index of 10.7 cm solar flux, as a measure of solar activity, into the categories of low (0-100), medium (100-140), and high (140+). There is a marked change in propagation azimuth from eastward during low solar activity, to north-westward and south-eastward during high solar activity.

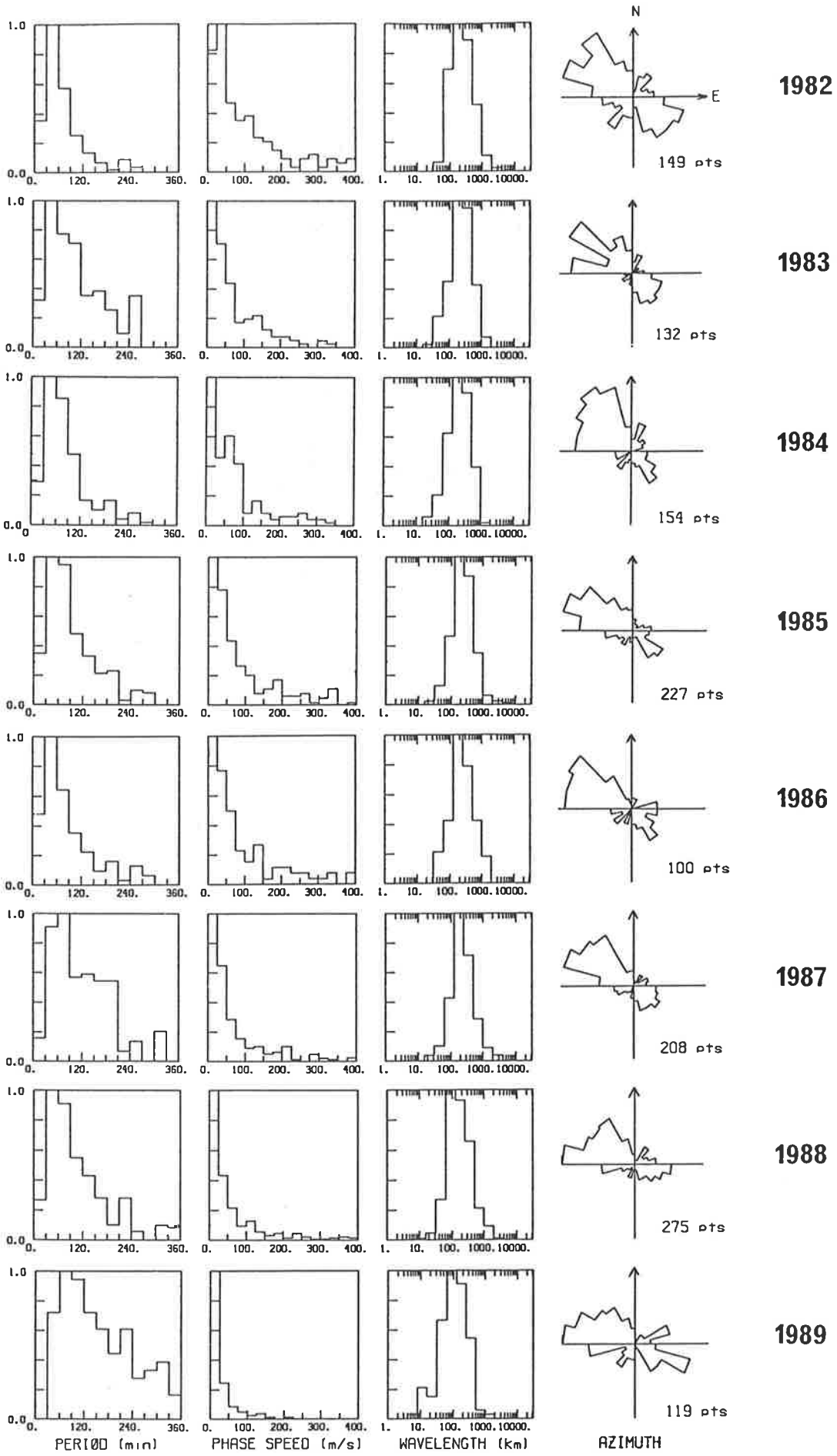

Figure 5.8. Distributions showing relative frequency of occurrence of observed period, phase speed, wavelength, and propagation azimuth, for λ630 nm Mawson data, from 1982 to 1989. The total number of points in each data set is shown in the bottom right corners.

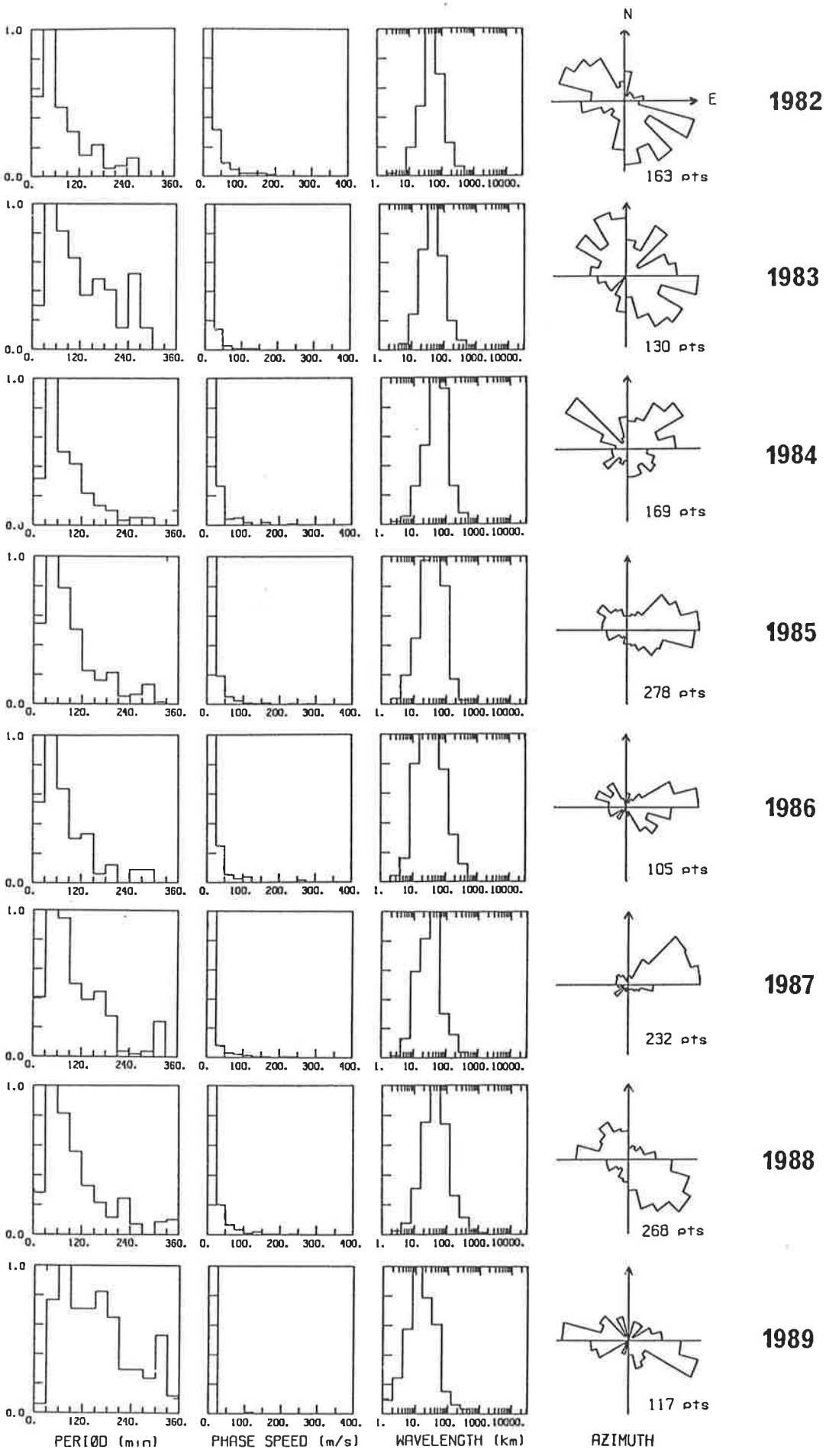

Figure 5.9. Distributions showing relative frequency of occurrence of observed period, phase speed, wavelength, and propagation azimuth, for λ558 nm Mawson data, from 1982 to 1989. The total number of points in each data set is shown in the bottom right corners.

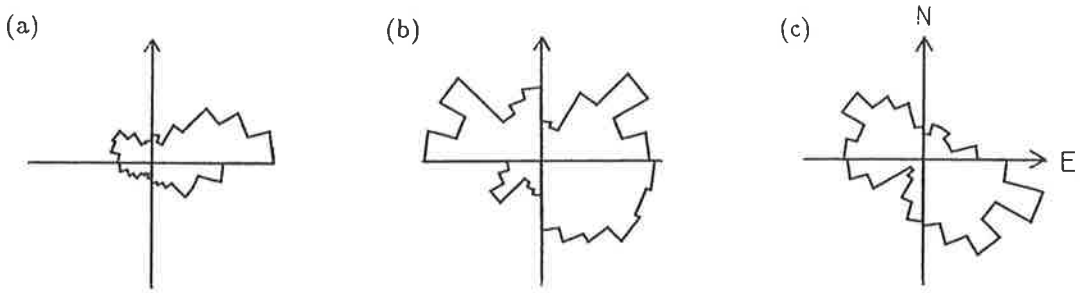

Figure 5.10. Propagation azimuths of waves in the λ558 nm emission from 1982 to 1989, grouped according to daily levels of F10.7 cm solar flux.
(a) Low flux (0-100) (b) Medium flux (100-140) (c) High flux (140+)

5.5 Combined azimuth distributions from 1982 to 1989

This section examines combined data from 1982 to 1989 for dependence of propagation azimuth on period, trace speed, and wavelength.

5.5.1 Period dependence

Waves in both emissions, from all years, were grouped according to period, in the ranges 0-60 min, 60-120 min, and 120+ min. Figure 5.11 shows there is little change in polarisation of propagation azimuths over these period ranges.

5.5.2 Speed dependence

Waves from all years were grouped according to trace speed, in the ranges 0-200 ms^{-1}, 200-400 ms^{-1}, and 400+ ms^{-1}, for those in the λ630 nm emission, and ranges 0-100 ms^{-1}, 100-200 ms^{-1}, and 200+ ms^{-1}, for those in the λ558 nm emission. Figure 5.12 shows a tendency towards stronger polarisation at low speeds, becoming more isotropic at greater speeds, for waves in both emissions.

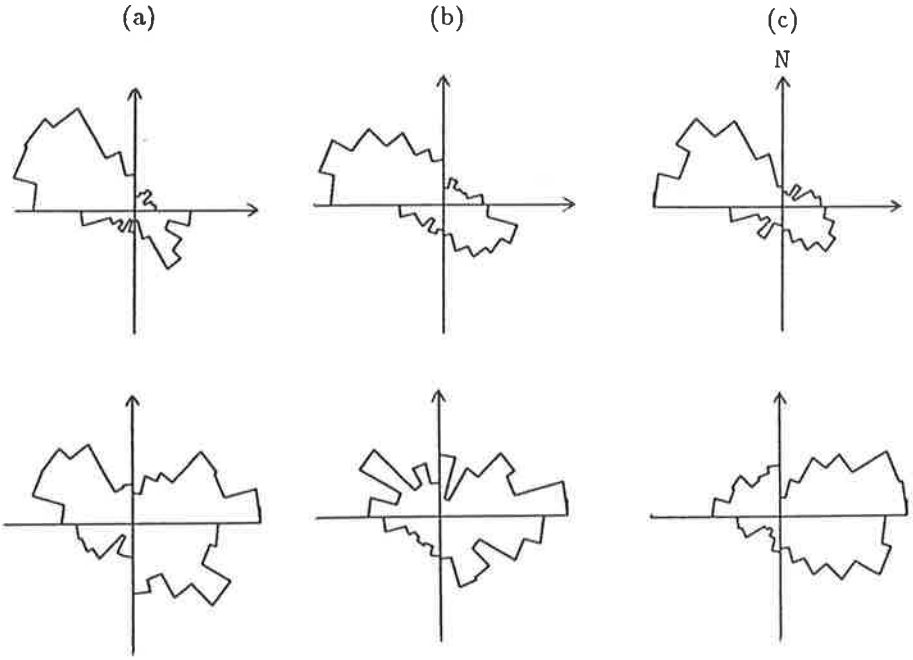

Figure 5.11. Propagation azimuths from 1982-1989 data, grouped according to period. The top row shows data from the λ630 nm emission, the bottom row shows data from the λ558 nm emission.
(a) 0-60 min (b) 60-120 min (c) 120+ min

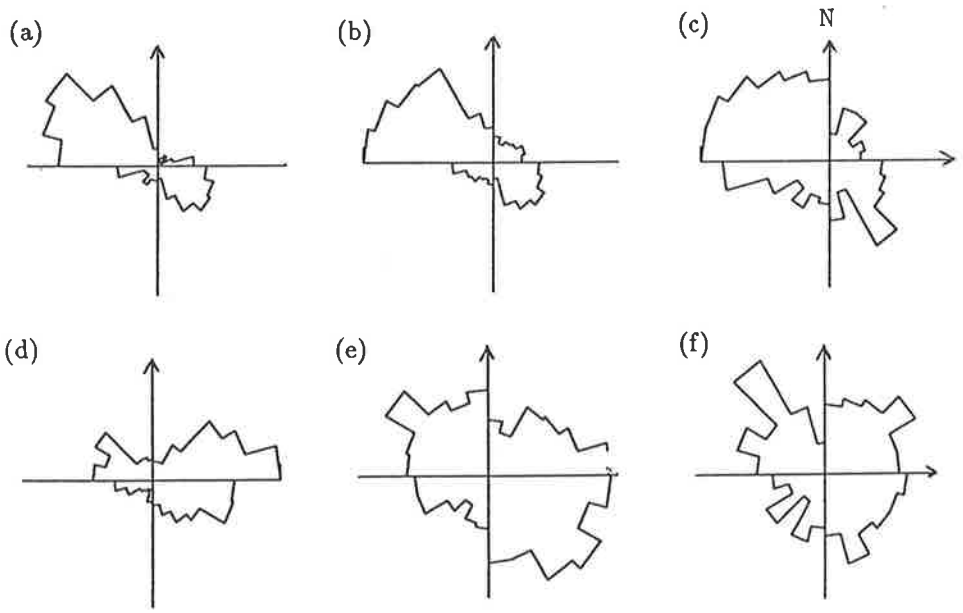

Figure 5.12. Propagation azimuths from 1982-1989 data, grouped according to trace speed. The top row shows data from the λ630 nm emission, the bottom row shows data from the λ558 nm emission.
(a) 0-200 ms^{-1} (b) 200-400 ms^{-1} (c) 400+ ms^{-1}
(d) 0-100 ms^{-1} (e) 100-200 ms^{-1} (f) 200+ ms^{-1}

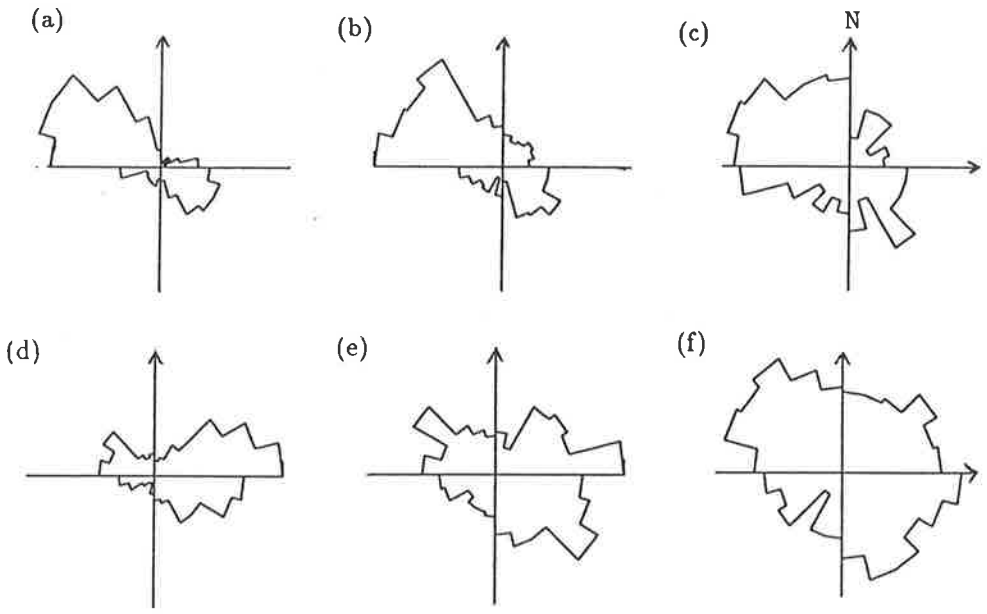

Figure 5.13. Propagation azimuths from 1982-1989 data, grouped according to wavelength. The top row shows data from the λ630 nm emission, the bottom row shows data from the λ558 nm emission.
(a) 0-200 km (b) 200-400 km (c) 400+ km
(d) 0-30 km (e) 30-60 km (f) 60+ km

5.5.3 Wavelength dependence

Waves from all years were grouped according to wavelength in the ranges 0-200 km, 200-400 km, and 400+ km, for those in the λ630 nm emission, and 0-30 km, 30-60 km, and 60+ km for those in the λ558 nm emission. Figure 5.13 shows a stronger polarisation at low wavelengths, becoming more isotropic at large wavelengths, similar to the trends in figure 5.12. This is consistent with the association of high speeds with larger-scale waves.

5.6 Comparison of propagation azimuths with other observations

Observations of gravity waves in the E and F regions were collated and summarised in tables 5.1 and 5.2. In particular, the forward direction of wave propagation and the sources and wind filtering effects suggested by the authors, were listed.

5.6.1 F region

In the F region (table 5.1) both MS and LS TIDs were observed. In general, LS TIDs propagated equatorward, and sources in the auroral region were suggested (Hunsucker and Tveten, 1967; Elkins and Slack, 1969; Davis and DaRosa, 1969; Hajkowicz and Hunsucker, 1987; Williams et al., 1988). 52% of south-eastward TIDs observed by Hunsucker and Tveten were preceded by auroral disturbances, measured at College, Alaska. Williams et al. (1988) reported two occasions on which propagating waves were observed following the onset of magnetospheric electric field fluctuations of the same periodicity. The LS waves observed in the λ630 nm emission by this author follow the general trend of predominantly equatorward propagation. The preference for north-westward rather than northward propagation is discussed in the following chapter.

Many observations have been made of MS TIDs in the F region (Davies and Jones, 1971; Bertin et al., 1975; Evans et al., 1983; Mercier, 1986; Waldock and Jones, 1987; Crowley et al, 1987; Ogawa et al., 1987) and are frequently attributed to tropospheric sources, since waves generated in the auroral zones are, theoretically, dissipated before reaching mid and low latitudes (where most observations are made). However, using reverse ray tracing, Bertin et al. (1975) located probable source regions in the vicinity of the auroral oval, for two out of nine retraced TIDs. The high-latitude observations of Crowley et al. (1987) show the behaviour of waves varying markedly with geomagnetic activity. During quiet periods, low-speed waves are observed with and antiwindward diurnally-rotating propagation azimuth. During active periods, waves of high speeds are observed propagating equatorward and east to southward. Crowley et al. suggest precipitation in the South Atlantic Anomaly and at mid-latitudes as a possible source. The high-latitude observations of Ogawa et al. (1987) show a decrease in wave activity with increasing K-index, which they point out may be an effect of the observing technique. An estimate of the wave activity observed by this author in the λ630 nm emission was made by calculating the mean number of waves per observing period for a range of K_p intervals. The result showed constant mean number of waves for $K_p = 1$

Table 5.1. Collation of F region observations of TIDs, listing the predominant direction of propagation, and the sources and/or wind filtering effects suggested by the authors.

Authors	Technique and assumed height	Location and date	Propagation direction	Suggested sources, wind effects
Hunsucker and Tveten (1967)	HF backscatter F region	Boulder, Colorado Nov-Dec, 1963, day	SE	52% from Alaska preceded by auroral events
Elkins and Slack (1969)	satellite scintillations F region	near Massachusetts May 67-April 68	140°-180°(E from N)	auroral zone
Davis and Da Rosa (1969)	columnar e^- content from Faraday rotation	US network near 35°N Feb 67 - Nov 68	160-200° (E from N) diurnal rotation	evening sector of electrojet
Hajkowicz and Hunsucker (1987)	ionosonde, riometer network, F region	S and N hemispheres Nov 1979	equatorward in both hemispheres	auroral source of large long. extent
Williams et al. (1988)	HF Doppler network	UK, near 53°N 2°W Oct 1985	S when mag. active, no preferred dirn when mag. quiet	correlation with periodicity in auroral activity

Continued overpage.

Table 5.1 continued

Authors	Technique and assumed height	Location Date	Propagation direction	Suggested sources, wind effects
Munro (1958)	5.8 MHz radar F region	near Sydney 1948-57	NE (winter, day) NW (winter, night) SE-SW (summer)	seasonal, diurnal change in azimuth
Davies and Jones (1971)	3.3, 4, 5.1 MHz radar 200-280 km	Boulder, Colorado June 67-June 68, sunset	S (winter) via W to N (summer)	no relation to mag./solar data
Bertin et al. (1975)	Faraday rotation, 250 km	UK network ~50°N 3°W Jan 1972	sector from SW to SE (winter)	met., auroral sources
Evans et al. (1983)	differential Doppler from satellite signals	Millstone Hill 43°N Jan 71 - Mar 73	mainly southward	seasonal, diurnal filtering, no inc. with K_p
Mercier (1986)	radio-interferometry 220 km	Nancay 47°N 2°E 1980-83, winter, day	SE	Ireland depression, wind filtering
Waldock and Jones (1987)	HF Doppler radar, 240 km	Leicester UK 52°N 2°W 1972-1975	source azimuths of 240-360°	tropospheric origin range < 1500 km
Crowley et al. (1987)	HF Doppler network 180-240 km	Antarctic Peninsula 1977	diurnal antiwindwd (mag. quiet) 280-30°,70-160° (mag. active)	variation in speed with mag. activity
Ogawa et al. (1987)	differential Doppler from satellite signals	Syowa, Antarctica 69°S 40°E Mar 85 - Jan 86	mainly equatorward	seasonal,diurnal variation, no increase with K-index

to 7, ie. no change in gravity wave activity with K_p. However, the calculation is biased, since a maximum of three waves per night are selected, so that excessive activity may b unaccounted for.

The frequency with which MS TIDs in the F region are observed to propagate equatorward, suggests that an auroral source may be contributing to some observations.

5.6.2 D and E regions

Both optical and radar observations of gravity waves in the D and E regions were collated (table 5.2). A wide range of propagation azimuths were reported and tropospheric and stratospheric sources were frequently suggested. Polarisation of propagation directions was generally attributed to seasonally and diurnally-varying wind filtering effects and/or localisation of source regions. The only (geographically) high-latitude observations presented here (Clairemidi et al., 1985) show some correlation with auroral activity, but from observations at Saskatoon and Calgary, which are at similar geomagnetic latitudes ($\sim$60°), no such correlation was reported.

Comparison of propagation azimuths with the λ558 nm results presented by this author, are not meaningful if the presumed sources are tropospheric, and therefore location dependent. No investigation of seasonal variation was possible, as nightglow observations were not possible over summer, with the extended daylight hours. The data were examined for changes in azimuths around equinox, but no identifiable trend was found. Investigation of diurnal variations was also limited, in this case by experimental constraints which allowed a maximum of 10 h continuous observation.

Table 5.2. Collation of D and E region observations of gravity waves, listing the predominant direction of propagation, and the sources and/or wind filtering effects suggested by the authors.

Authors	Technique and assumed height	Location Date	Propagation direction	Suggested sources, wind effects
Sinno et al. (1964)	1.85 MHz pulsed sounder E_s region	Japan, ~36°N 140°E May 61- May 62, May 63	SW drift	instability in wind shear
Freund and Jacka (1979)	λ558 nm airglow, 95 km	Adelaide, 35°S 138°E 1973	no preference indicated	tropo. fronts low pressure trough
Gavrilov and Shved (1982)	λ558 nm airglow, 100 km	Ashkhabad, 38°N 1964-1967	SSE (winter) N (summer)	jet stream, fronts, mtns. seasonal wind filtering
Meek and Manson (1983)	λ558 nm airglow, 95 km	Saskatoon, 52°N 107°W Dec 80, Mar 81	$\gtrsim$ 90° from wind directions	
Clairemidi et al. (1985)	OH airglow, 80-100 km	Sodankyla 67°N 26°E Dec 81- Jan 82	2 examples, SE/NW and SW/NE wavefronts	often coincided with active aurora
Ebel et al. (1987)	MF radar, 60-110 km	Saskatoon 1979-1983	E/W,N/S (T=1-6 h) N/S (T<1 h)	oro. source, jet stream seasonal wind filtering
Vincent and Fritts (1987)	MF partial reflection radar, 60-100 km	Adelaide, 35°S 138°E Nov 83 - Dec 84	~S (winter, T=1-8 h) NNW (winter, T=8-24 h) SSE (summer, T=1-24 h)	seasonal wind filtering
Manson and Meek (1988)	MF radar (Gravnet) 60-120 km	Saskatoon 1983-1985	dominantly S, some E/W below 100 km during summer/winter	seasonal and height dependence due to wind filtering
Cogger et al. (1988)	OH, λ558 nm emission, 85, 95 km	Calgary, 51°N 114°W 1985-1987	fewer in SE sector	Rocky Mtns, wind filtering

Chapter 6

Discussion

The polarisation of wave propagation azimuths shown in Chapter 5 suggests two possibilities (or a combination of both): either a wind filtering mechanism is acting to remove waves propagating in certain directions, or else two or more distinct sources of waves (possibly thermospheric and tropospheric) are contributing to the waves observed in the thermosphere. These possibilities are discussed below. The paucity of data from southern high-latitude regions and especially from the lower thermosphere makes it difficult to assess the factors affecting wave propagation in this region. Therefore the following discussion is intended as a qualitative description of possible interpretations of the results; no clearcut explanation was found.

Propagation azimuths are referred to in geographic (gg.) coordinates, unless geomagnetic (gm.) coordinates are explicitly specified.

6.1 Thermospheric wind effects

The effect of a background wind on a propagating gravity wave is to Doppler shift its frequency and phase speed in the wind reference frame, with respect to the ground-based observations. In the presence of a vertical wind shear, the wave ray path is refracted towards the vertical or horizontal, and the wave may be either reflected, or

absorbed at a critical level. If waves are generated omni-directionally (ie. propagate away from a source in all directions) the observed effect of a vertical wind shear is a reduction in the number of waves propagating in a direction parallel or antiparallel to the mean wind. If waves are not generated omni-directionally, but propagate away from the source over a narrow range of azimuths, the only observable effect is a possible reduction in the number of waves.

Horizontal shears in the mean wind cause an analogous refraction of propagating waves, the effect being a rotation of the wave propagation azimuths about the vertical axis of the wind shear. This may not be observable in an omni-directional wave field, but if the waves are generated with a narrow range of propagation azimuths, the observed effect is a refraction of propagation direction towards that of the mean wind. To be a noticeable effect, the horizontal shears must be large.

The discussion in this section focusses on an interpretation of the observed azimuth distributions, considered firstly as the result of filtering of an initially omni-directional wave field by vertical wind shears, and secondly as essentially mono-directional waves refracted by horizontal wind shears. It is assumed that waves of period greater than about 20 min are removed most effectively in a direction parallel with the mean wind and less effectively in the antiparallel direction (as suggested by results of simulations by Hines and Reddy, 1967, revised in Hines et al., 1974, p598-604).

It has been suggested that filtering by vertical wind shears has significant effect on the azimuthal spectrum of waves propagating through the lower and middle atmosphere (eg. Gavrilov and Shved, 1982). The effect is difficult to assess in the thermosphere because of the wind's variability. The University College London (UCL) general circulation model (Rees and Fuller-Rowell, 1988) was used to simulate thermospheric winds for the following discussion. The atmosphere is divided into 15 pressure levels, each equivalent to one scale height, starting at 80 km altitude. A variable cross-polar cap potential and intensity of auroral particle precipitation were used to specify the geomagnetic power input. Separate simulations were available for positive and negative IMF B_y component; $B_y < 0$ simulations have been found to match more closely with

interferometric measurements of winds in the λ630 nm emission (Conde, 1990) and so were used here.

Figure 6.1 shows wind patterns for the winter solstice at the latitude and longitude of Mawson for conditions of low and high solar activity and quiet, moderate, and disturbed geomagnetic conditions. Pressure levels 7 and 11 correspond approximately to the altitudes 127 km and 212 km, and are associated with the λ558 nm and λ630 nm emission heights for the purpose of the discussion. However, in assigning a height to the pressure levels, the model took no account of changes in the exospheric temperature between simulations, so that they may be inaccurate. The limitations of the model are illustrated by the observations of Jones and Jacka (1987), who measured winds and temperatures in the λ558 nm emission over Mawson. The measured winds showed good qualitative agreement with winds at 120 km predicted by an earlier version of the model; the model overestimated the magnitudes by a factor of two. Measured temperatures were compared with the US Standard Atmosphere, to infer the height of the emission layer. However, the measured winds show good quantitative agreement with the more recent model winds at pressure level 7, but the measured temperatures were more typical of the model at level 6 (for the appropriate simulation).

Consider first the λ558 nm emission height. To produce the azimuth distributions of figure 5.9 through filtering, winds from 15 to 01 UT should be north, west, and southward during low solar activity, and northeast and south-westward during high solar activity. The model winds at and below level 7 show no such variation with solar cycle; rather the winds show the increasing effect of the magnetospherically-driven convection pattern with increasing geomagnetic activity. The wind direction during certain periods is consistent with the filtering direction inferred from the observations (eg. winds during low solar and high geomagnetic activity are consistent with 1987 observations), but in general there is no relationship. Of course, if the waves are generated in the troposphere, strato-mesospheric winds must also be considered, but these are predominantly eastward during winter (Andrews et al., 1987, p225). Mesospheric tidal amplitudes are comparable with mean winds over Mawson (Phillips and Vincent, 1987). The meridional component is generally stronger than the zonal component, which may

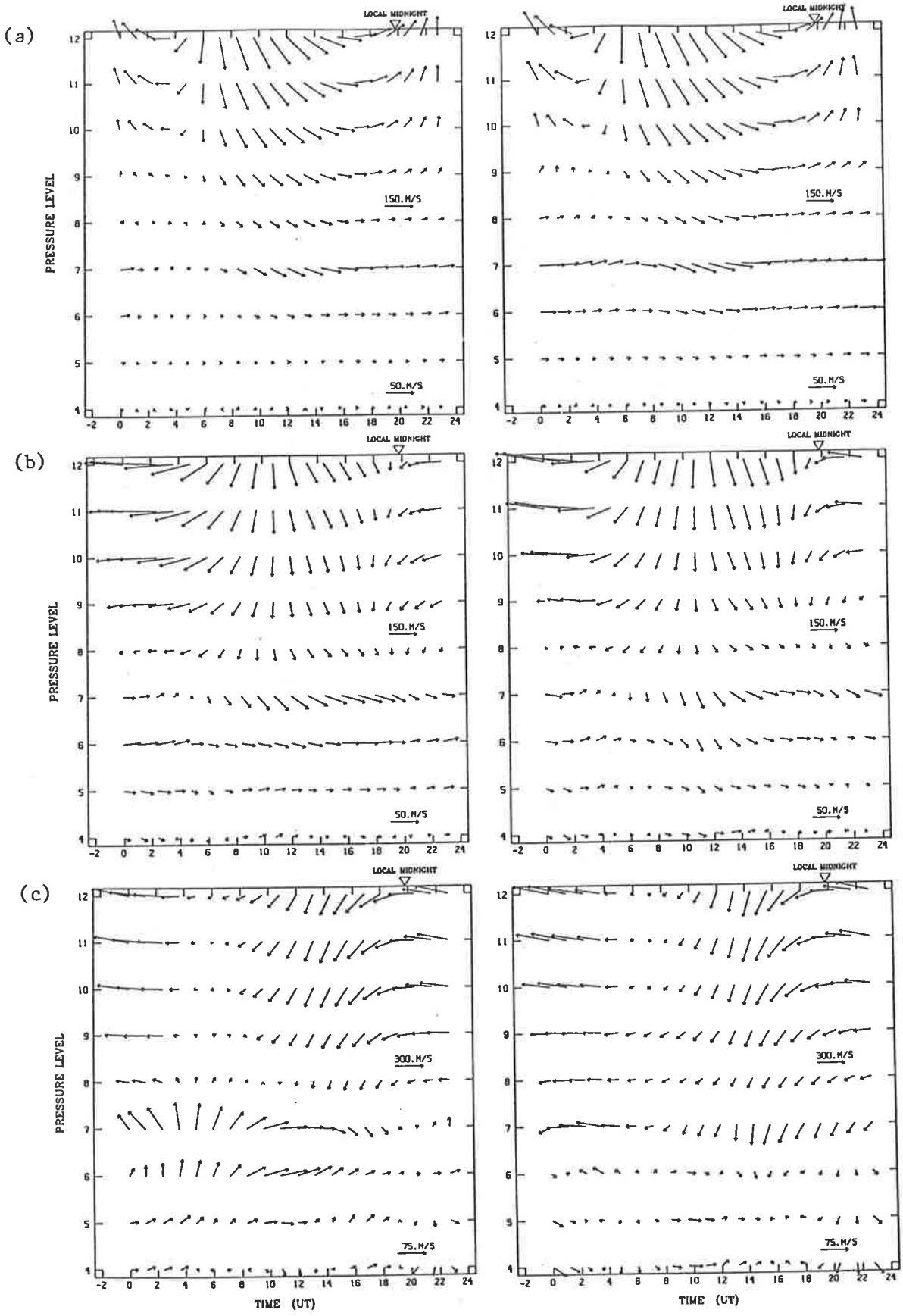

Figure 6.1. Time-altitude profiles of thermospheric winds for geomagnetic conditions which are (a) quiet (b) moderate (c) disturbed. Conditions of low solar activity are represented in the profiles on the left and of high solar activity on the right. Winds are derived from the the UCL model (Rees and Fuller-Rowell, 1988) for the latitude and longitude of Mawson, and for winter solstice. Northwards is vertical and eastwards is to the right. Note that the winds scale changes between levels 7 and 8.

cause some critical layer filtering in the north-south direction. However, the amplitudes are relatively small ($\sim$15ms^{-1} seasonally averaged) and are not known to exhibit solar-cycle variations.

Consider next the winds at the height of the λ630 nm emission layer. In general, the model predicts winds at level 11 which are approximately three times greater than those at level 7 (note the change in scale between levels 7 and 8 in figure 6.1). However, again the wind varies in such a way that it is not always consistent with filtering of waves (spanning the sector from north to southwest) as illustrated in figure 5.8. Possibly more significant, since waves at this height travel relatively large horizontal distances, is the effect of horizontal refraction. Figure 6.2 shows the spatial distribution of modelled winds over the southern polar region, at 20.4 UT, which is close to the middle of the typical observing period. Winds corresponding to quiet, moderate, and disturbed conditions are shown. During quiet periods, the wind is basically antisunward, with little shear. During moderate and disturbed periods, an increasingly strong convection cell develops (to the east of Mawson for this UT time). Waves passing through this region would be refracted towards the wind direction, which changes with longitude from northwest to southwest. This is mentioned in context in the following section.

This representation of the winds over the polar region is a simplified treatment of a complex situation. Figure 6.1 illustrates that the wind has significant altitude and UT dependence; figure 6.2 shows large spatial variations, and the determination of wave propagation through the wind field is non-trivial. An appropriate treatment is through reverse ray tracing of observed waves using an appropriate thermospheric wind model and a multilayer approximation. Work on this is planned.

6.2 Sources of waves in the λ630 nm emission

As discussed in section 5.1, waves in the λ630 nm emission display the characteristics of LS gravity waves. LS TIDs observed in the F region are thought to be generated during

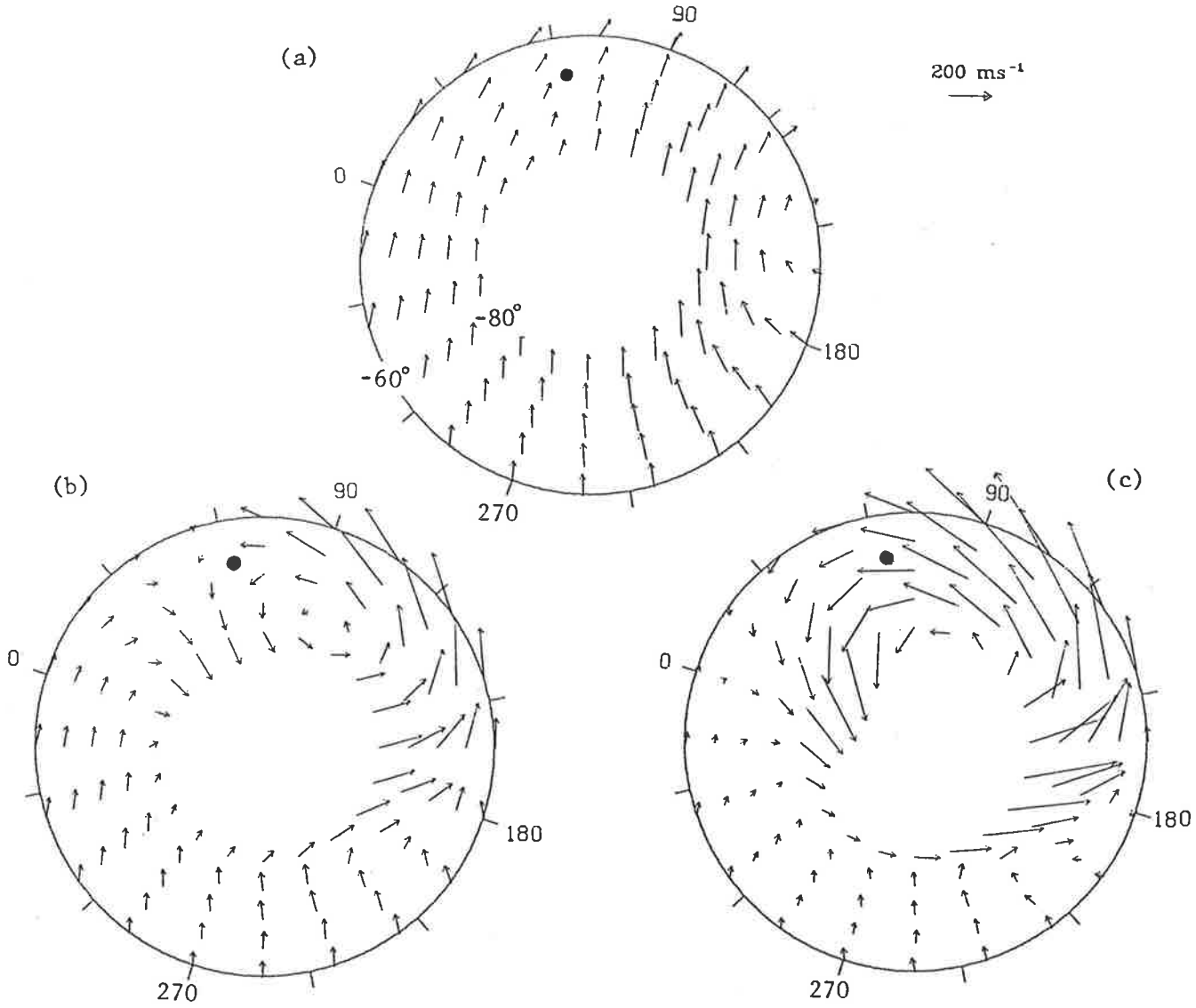

Figure 6.2. Spatial distributions of winds over the polar region for geomagnetic conditions which are (a) quiet (b) moderate (c) disturbed. Solar activity is high in all cases. Wind fields are derived from the UCL model at 20.4 UT (which is close to Mawson local midnight), pressure level 11 (around 210 km altitude), and during winter solstice. Geographic coordinates are used; north is radially outwards and east is clockwise. Vectors are given from latitudes -60 ° to -80 °; longitude is marked. The position of Mawson is indicated by the dot.

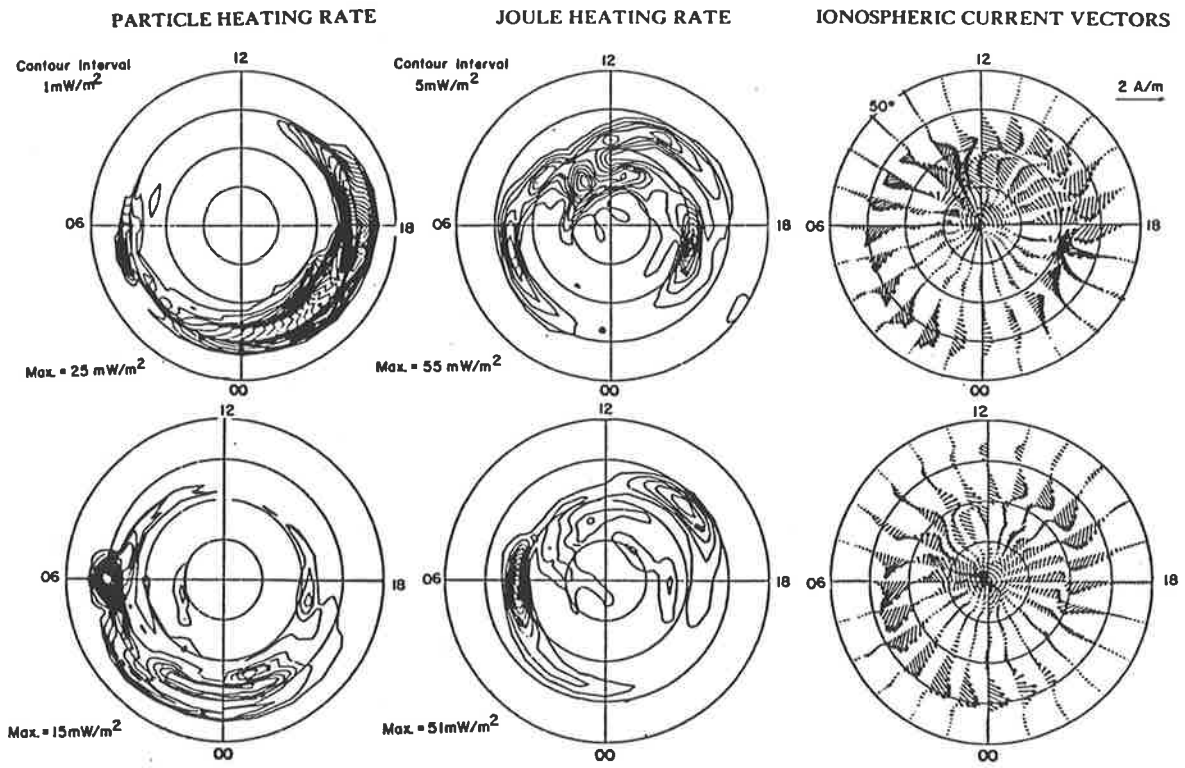

Figure 6.3. Distributions of integrated particle and Joule heating rates, and ionospheric current over the polar region during substorm activity (from Ahn et al., 1989). The images have been mirror reversed to represent southern hemisphere coordinates (in magnetic latitude-time).

magnetic substorms (eg. Hajkowicz and Hunsucker, 1987; Testud, 1970). Chimonas and Hines (1970) modelled gravity waves launched by a disturbed auroral current, represented as a 2-dimensional line source; they found that both Joule heating and Lorentz forcing produced gravity waves with cylindrical wavefronts propagating away from the source. Simulations of substorm disturbances of auroral currents by Richmond and Matsushita (1975), showed gravity waves propagating poleward and equatorward away from the source. An example of the distributions of particle and Joule heating and ionospheric current vectors in the polar region during substorm activity, is shown in figure 6.3, taken from Ahn et al. (1989). The diagrams have been mirror reversed to represent southern hemisphere coordinates. The heating and current distributions are closely aligned along magnetic east-west, extending thousands of kilometres, and covering about 5° of latitude. These characteristics are represented, in simplified form, in the model and simulations of Chimonas and Hines (1970) and Richmond and Matsushita (1975). Therefore it is likely that the disturbances shown in figure 6.3 generate gravity

waves with effectively cylindrical wavefronts aligned along gm. east-west, propagating towards gm. north and south.

At Mawson, gm. north is approximately 45° west of gg. north. Therefore, the average alignment of the auroral electrojet is gg. northeast-southwest, and would be expected to generate waves travelling towards the northwest and southeast. Referring to figure 5.8, this is approximately the situation observed in the λ630 nm emission. The tendency towards somewhat more westward propagation may be attributable to refraction of the wavefronts by horizontal shears in the mean wind, as discussed in section 6.1. The preference for propagation towards northwest rather than southeast may be explained in terms of the nighttime location of the auroral oval mainly over or poleward of Mawson (Bond and Jacka, 1960, 1962; Akasofu, 1978). During periods of high geomagnetic activity, the auroral oval expands over and possibly equatorward of Mawson. However, as low-frequency waves propagate at low elevation angles (calculated from the dispersion relationship to be less than 20° in most cases), few south-eastward waves are expected to reach the height of the λ630 nm emission layer before passing over Mawson.

Periods of increased activity in the electrojets, caused by geomagnetic substorms, are present throughout the solar cycle, with increased intensity and frequency during solar cycle maxima. Therefore the LS waves described above should be present during all phases of the solar cycle, but possibly with greater frequency during solar cycle maxima. The results confirm the continuous presence of these waves, but with only a small increase in the (relative) number during solar cycle maxima. However, the analysis selected (a maximum of) three periodicities per night, with no comparison of the relative power of waves selected, from night to night, so that excessive activity is not properly represented.

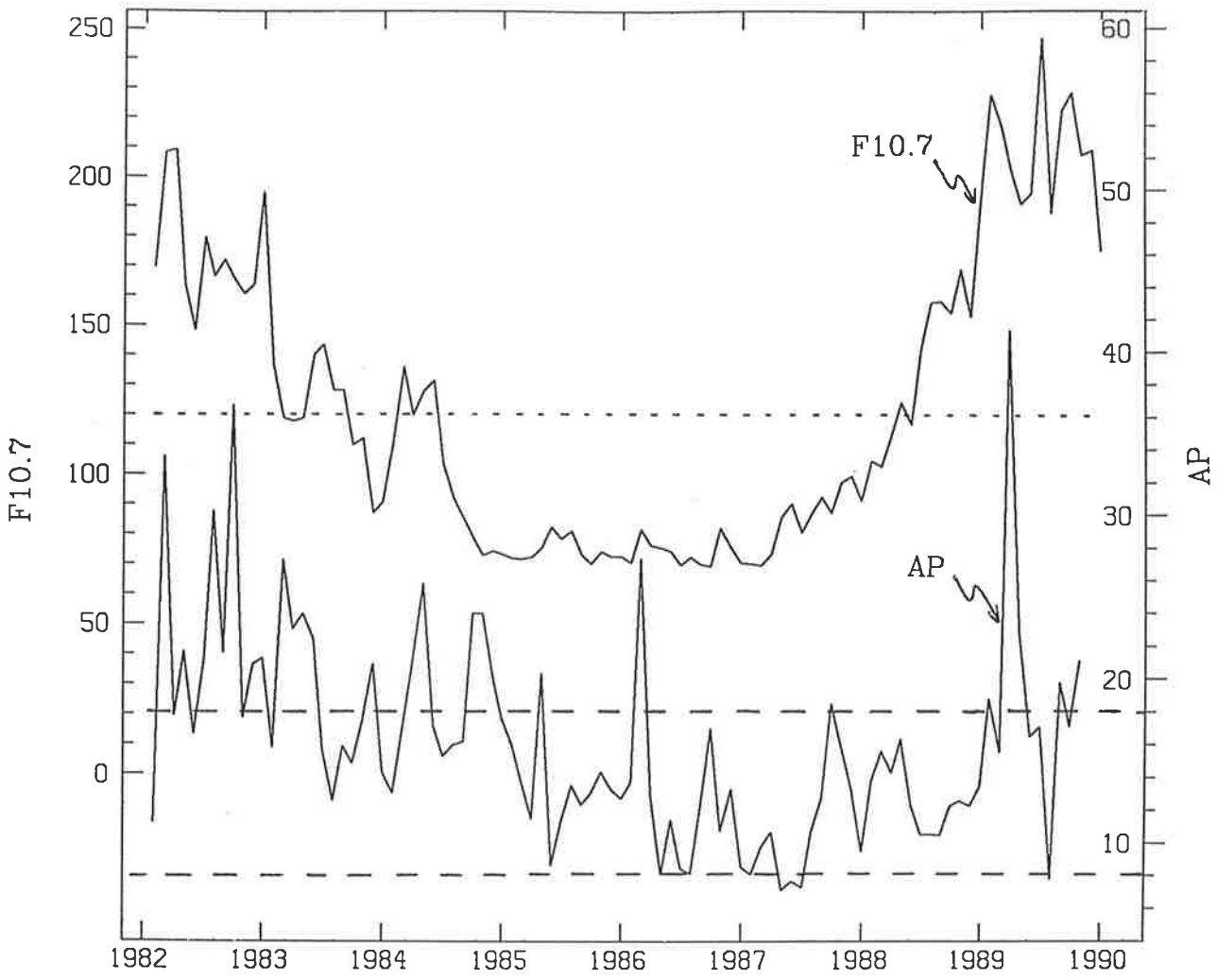

Figure 6.4. Monthly averages of F10.7 cm solar flux and A_p from 1982 to 1990. High and low F10.7 cm categories are divided by a dotted line. High, medium, and low A_p categories are divided by dashed lines.

6.3 Sources of waves in the λ558 nm emission

The λ558 nm distributions show apparent solar-cycle dependence. In the following sections the data are grouped according to levels of solar activity as measured by the daily F10.7 cm solar flux index. The data were then subdivided according to levels of geomagnetic activity, as measured by the daily A_p index. Monthly averages of F10.7 cm solar flux and A_p index from 1982 to 1990 are shown in figure 6.4 for reference. Figure 6.5 shows the results of grouping the λ558 nm data using two levels of solar flux, F10.7<120 and F10.7>120, and three A_p categories, A_p =0-8, A_p =8-18, and A_p >18. The λ630 nm results were grouped in the same way and are presented here for completeness (figure 6.6) although they show little variation.

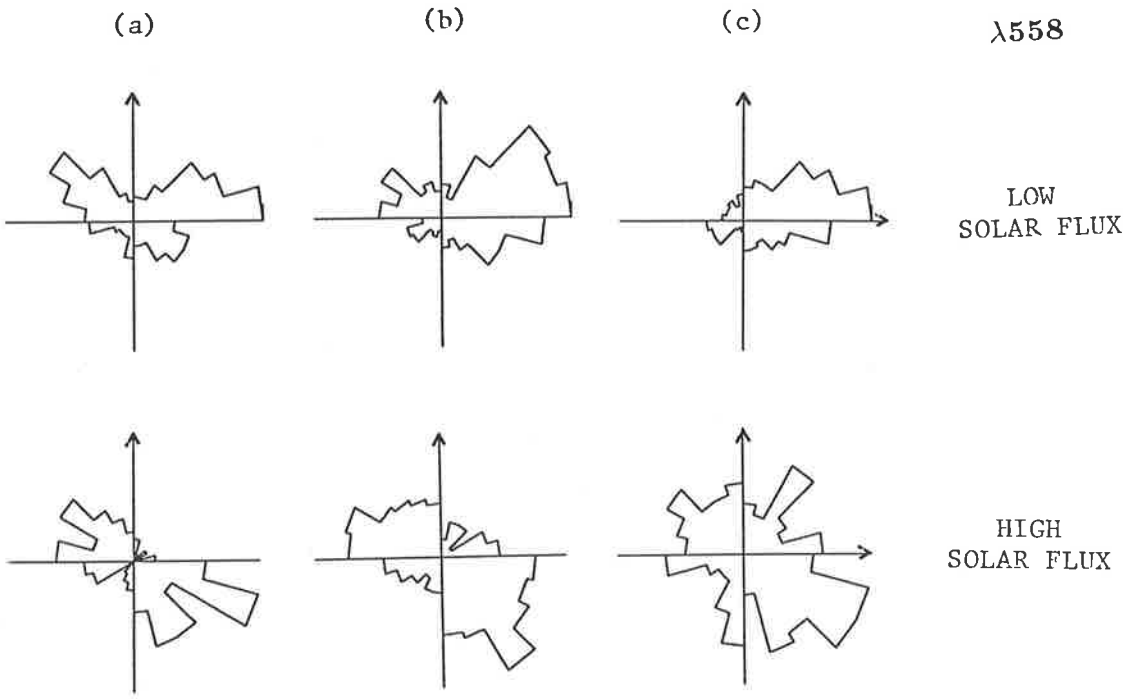

Figure 6.5. Azimuth distributions showing λ558 nm data grouped according to levels of solar activity at the time of observation: low, F10.7<120 (top line) and high, F10.7>120 (bottom line). These are then subdivided according to level of geomagnetic activity: (a) A_p 0-8 (b) A_p 8-18 (c) A_p 18+

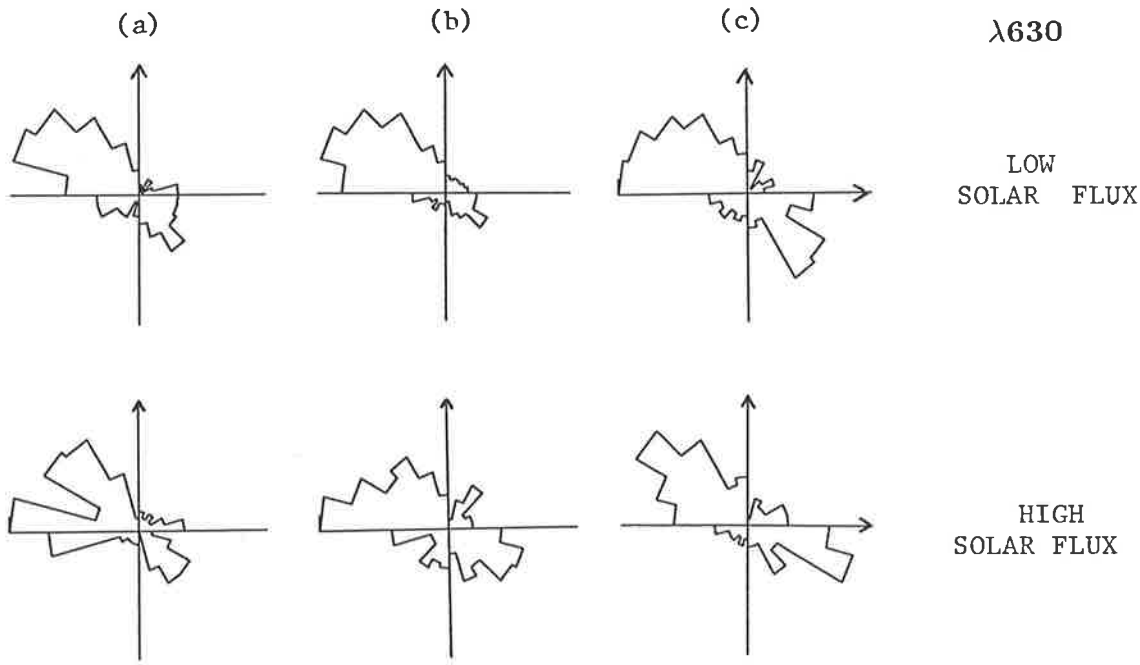

Figure 6.6. As for figure 6.5, showing λ630 nm data.

It is suggested, and discussed further in the following sections, that during high solar activity, aurorally generated waves dominate the λ558 nm observations; that during low solar activity waves generated in the troposphere dominate, but aurorally-generated waves become noticeable when the λ558 nm emission layer and the auroral electrojet are close in altitude. The adjectives 'tropospheric' and 'thermospheric' will be used to mean 'waves presumed to be generated in troposphere' and 'waves presumed to be generated in the thermosphere, ie. the auroral electrojet', respectively.

6.3.1 The auroral electrojet as a source region

During periods of high solar activity, the distributions of waves in the λ558 nm emission resembles those in the λ630 nm emission, showing waves propagating predominantly towards the northwest and southeast. The similarity in azimuth distributions suggests that most waves observed in the λ558 nm emission during high solar activity are generated by the same source, presumed now to be the auroral electrojet. A larger proportion of waves in the λ558 nm emission are observed propagating towards south-east as compared with those in the λ630 nm emission. The λ558 nm emission layer is much closer in altitude to the source region, so that any expansion of the auroral oval to positions equatorward of Mawson would enable south-eastward propagating waves to pass through and be observed in the λ558 nm emission region. They may not reach the λ630 nm emission height before passing over Mawson because of the relatively low elevation angle at which the waves propagate (calculated from the dispersion diagram to be $<30°$ for most waves in the λ558 nm emission).

The distributions from the periods of low solar activity show waves propagating towards east (gm. southeast). It is difficult to explain how these could arise from aurorally generated waves in the manner described in section 6.2. It is possible that they are produced by localised source regions, but there is no obvious reason why source regions should lie predominantly west (gm. northwest) of Mawson during low solar activity. However, if localised source regions are producing these effects, a more positive identifi-

cation of the source region may be obtained by analysing each night's data in 3-hourly intervals and grouping the results according to the A_p index for each 3 h interval. This would reveal any temporal change in propagation azimuth as Mawson rotates past the source region. (It would also allow more accurate determination of correlation between azimuth and A_p). This was not attempted by the author because of time constraints. However, unpublished work by D.Y.Wang shows no significant change in azimuths when 1982 data was analysed in pre and post midnight sections.

6.3.2 Tropospheric sources

During periods of low solar activity, the azimuth distributions are polarised towards the east to northeast. This change in polarisation suggests that possibly waves from a different source are dominating the distributions. Likely tropospheric source(s) are considered.

Regions of strong wind shear (in which the Richardson number is below the critical level of 0.25) are frequently suggested as sources of tropospheric gravity waves, but can be difficult to trace. Using microbarograph, radar, and aircraft records, Hooke and Hardy (1975) and Reed and Hardy (1972) observed gravity waves which they suggested were generated by upper tropospheric shear flow. They found gravity waves propagating below and within the shear region, in the direction of the mean wind, with phase speeds of about 50 ms^{-1}(close to the speed of the wind in the middle of the shear layer). The critical level is the supposed generation region. However, the theory of gravity waves generated by shear instabilities is not well understood. McIntyre and Weissman (1978) suggested that a non-linear treatment of the theory is necessary to show waves radiating away from regions of strong instability.

A widespread feature of the Antarctic troposphere is the strong katabatic wind, ie. down-slope wind over the ice-cap. Figure 6.7 shows the mean annual windflow over Mawson from ground level to approximately 15 km, compiled from 28 years' data by Streten (1990). The ground-level katabatic wind is directed towards the northwest,

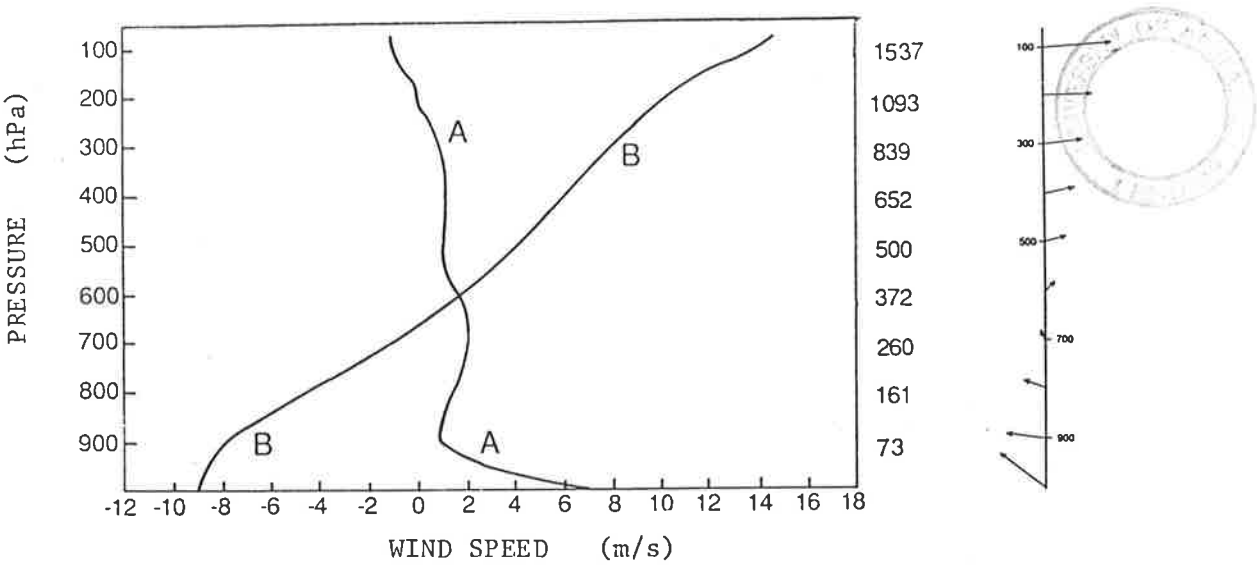

Figure 6.7. Annual averages of tropospheric and lower stratospheric wind measurements above Mawson (from Streten, 1990). The left scale indicates pressure levels and on the right are corresponding mean heights (decameters). A = north/south component, B = east/west component. Vector velocities are shown on the right at 100 hPa intervals. North is vertical, east is to the right.

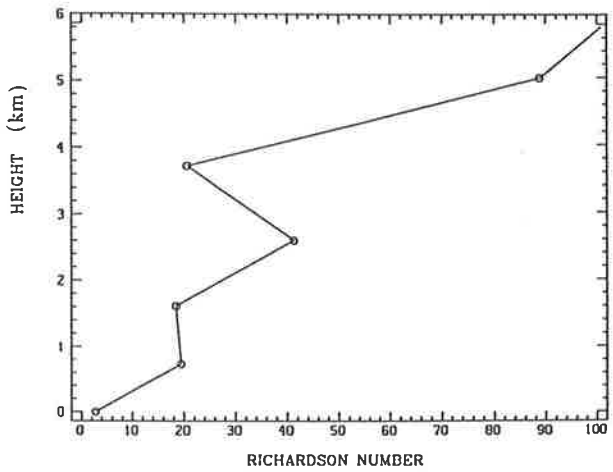

Figure 6.8. Altitude profile of the Richardson number from 0 to 6 km estimated from the wind profiles of figure 6.7, and temperature profiles presented in Streten (1990).

turning towards the east above about 5 km. The wind speed decreases rapidly between the surface and 1 to 2 km altitude, so that the region of wind shear from 0 to 1 km is a likely source of gravity waves. The Richardson number, from 0 to 6 km altitude, was estimated from the winds in figure 6.7 and from mean monthly temperature profiles (Streten, 1990); the results are presented in figure 6.8. The Richardson number is high in all regions, dropping to approximately 2 in the region from 0 to 1 km, which is not sufficiently small to indicate shear instability. However, these calculations were made

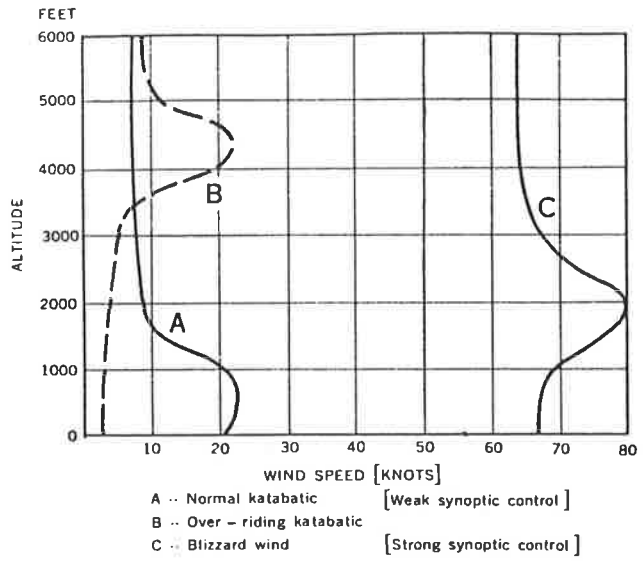

Figure 6.9. Typical wind profiles for katabatic and blizzard conditions at Mawson (from Streten, 1963).

for annual means; winter wind speeds are greater than those in summer, and short time-scale fluctuations can be significantly greater than the mean. "Strong gusts are a feature of turbulent katabatic flow..." and gusts exceeding 30 ms^{-1} are frequently recorded at Mawson (Streten, 1990). Figure 6.9 indicates that the vertical extent of large shears is around 300 to 500 m for both katabatic and blizzard conditions. A gust speed of 30 ms^{-1} decreasing over 500 m to 10 ms^{-1} (close to the profile values of figure 6.7), has an associated Richardson number of around 0.15. Given that this is still a macroscopic estimation, it seems likely that katabatic gusts produce gravity waves through shear instability. The wind speeds involved are of the order of the true phase speeds calculated for the λ558 nm data.

Figure 6.10 shows typical winter anemomograph records of wind speed and direction at Mawson, giving an indication of the frequency with which such gusts occur, in particular, around 7 pm (figure 6.10a), and 8:45 pm and 11:30 pm (figure 6.10b). Since a large surrounding area (say 1000 km radius) constitutes the possible source region for katabatic-generated waves, the frequency of occurrence may be sufficient to produce the amount of wave activity observed.

The propagation azimuth of such waves will be in the direction of wind shear. This is towards the northwest during steady flow, but may vary significantly during gusts, and onset and cessation of the katabatic wind. Above the katabatic, the wind direction rotates to the east, forming the winter eastward circumpolar vortex in the upper

(a)

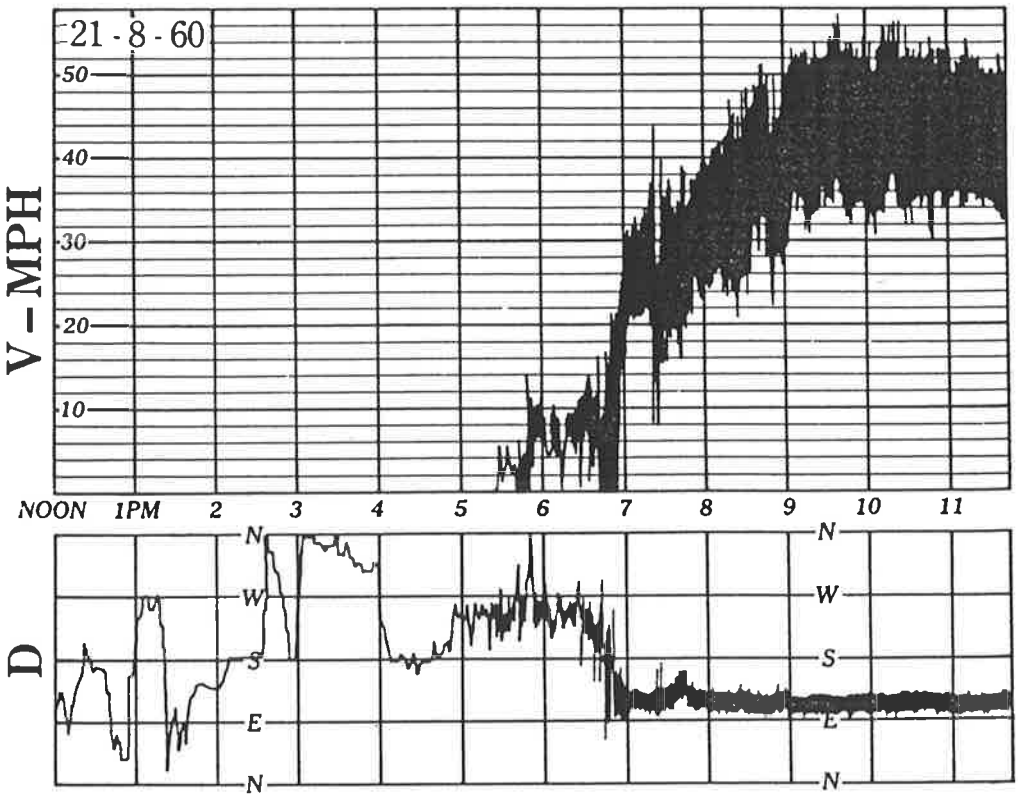

(b)

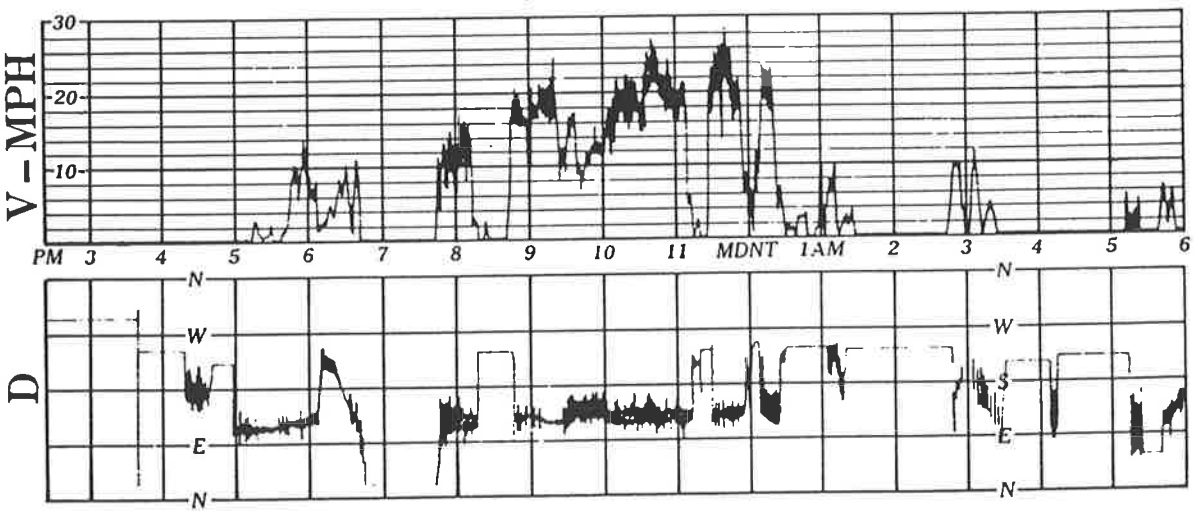

Figure 6.10. Anemomograph records of wind speed and direction at Mawson (from Streten, 1963). (a) Typical winter katabatic onset (b) Fluctuations in katabatic wind

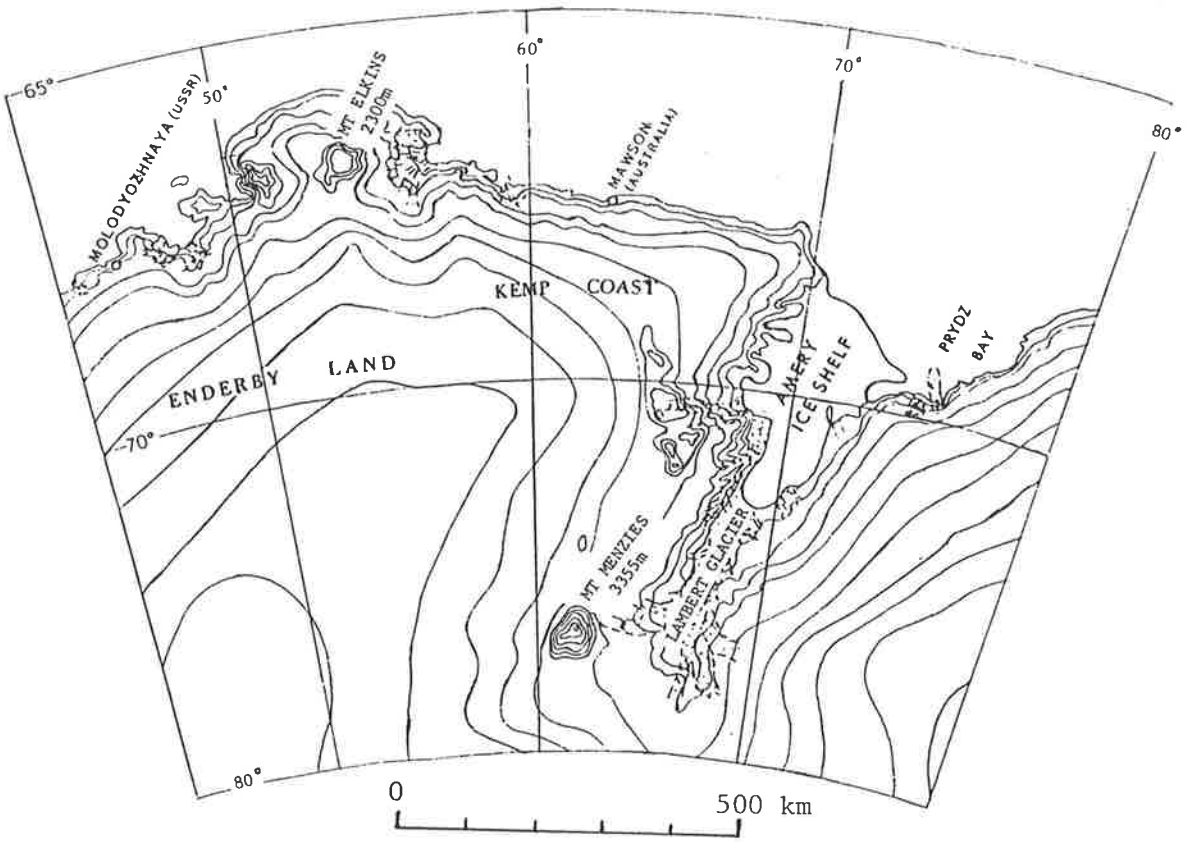

Figure 6.11. The general topography around Mawson. Possible wave-producing features are Mt Menzies to the south and Mt Elkins to the west.

troposphere and lower stratosphere (Schwerdtfeger, 1984, p120-125). The degree of refraction towards the east experienced by a wave propagating up into the vortex region, is dependent on the time taken to propagate through. For low propagation angles, longer propagation times are expected, and there may be significant refraction. This seems a plausible explanation for the north-eastward to eastward waves observed during low solar activity. Again, ray-tracing through a suitable model atmosphere is required for a quantitative confirmation.

Waves may also be generated in the troposphere by wind flow over mountains (orography). Modelling by Schoeberl (1985) showed that in some cases they are able to propagate up to the mesosphere. In the presence of a constant wind, orography produces standing waves (ie zero phase velocity) which are not detectable with a cross-correlation technique. However, waves with non-zero phase speed may be generated during periods of non-constant wind, or gusts (as suggested in Gossard and Hooke, 1975, p359). The topography around Mawson is shown in figure 6.11. Features which

are likely to produce mountain waves are Mt Elkins, about 400 km west of Mawson, and Mt Menzies and adjacent mountains along the Lambert Glacier, 400-650 km south of Mawson. However, orographically generated waves may be reflected by rapid wind reversals above the generation region, which constitute a critical layer for standing waves (Clark and Peltier, 1984; Balsley and Carter, 1989) thus reducing the number of mountain waves propagating into the stratosphere above Mawson.

6.3.3 Discussion of the model

Several questions arise concerning this interpretation of the results. Firstly, if the troposphere is a rich source of gravity waves observed in the lower thermosphere during low solar activity, why are they not observed during years of high solar activity? A possible explanation lies in the increase in thermospheric temperature with increasing solar activity. Hines and Reddy (1967, revised in Hines et al., 1974, pp598-604) calculated the percentage energy transmission of waves with a range of periods and speeds, through regions of strong wind and temperature gradients. Temperature profiles were chosen to represent mesospheric and thermospheric conditions. They found that decreased transmission, purely due to temperature gradients, became significant only in the mesospheric temperature structure when the condition for total reflection was approached, ie. $\Omega/k_x \gtrsim \omega_b c/\omega_a$ (section 2.3.2). Mohanakumar (1985) presented evidence which suggested that there is a significant increase in mesospheric temperatures (maximising around 65-70 km) during high solar activity, and especially over Antarctica. The inclusion of wind shears in the simulation resulted in lower, and anisotropic, transmission. Dartt et al. (1983) presented data showing eastward winds at 90 km during winter which were stronger during solar maximum than minimum. However, the difference did not appear large enough to produce the effects observed here.

A second question arises, namely, why are few 'thermospheric' waves observed in the λ558 nm emission during periods of low solar activity? The following discussion suggests that 'thermospheric' waves are present but dominated by the number and amplitude of the 'tropospheric' waves, and are observable only when the altitude of the λ558 nm

emission layer is close to that of the (auroral) source of waves. If the emission layer is below the source, only waves with a downward component of propagation will pass through the emission layer. These will be of relatively small amplitude, since amplitude decreases exponentially with decreasing height.

The height of the λ558 nm emission layer is dependent on the altitude versus concentration profiles of the atmospheric species associated with $O(^1S)$ excitation and quenching, and on the energy spectra of auroral electrons.

The MSIS-86 thermospheric temperature and composition model of Hedin (1988) was used to obtain profiles of the major species involved in $O(^1S)$ λ558 nm emission (O, O_2, N_2), during low activity (F10.7 = 70, A_p = 4) and high activity (F10.7 = 200, A_p = 20). Differences in the density profiles were not significant below about 200 km. However, the region of interest is close to the lower limit of the model (85 km) and data on which it is based are very sparse between 90 and 150 km (140 km is the lowest altitude for which O data is available), so the model predictions may not be representative.

Energy spectra of auroral particles have large temporal and spatial variations, but on the whole, a hardening of the spectra occurs with increasing geomagnetic activity (eg. Hardy et al., 1985; Vallance Jones, 1974, p75-79). Increasing the mean energy of the electron spectra results in a narrower and lower emission layer. Figure 6.12 shows calculated profiles of λ558 nm emission decreasing with increasing electron energy (Banks et al., 1974). Although these profiles take no account of indirect $O(^1S)$ excitation mechanisms, the general downward trend is representative. This is evidenced by the extensive observations of Störmer (1955) (referred to in Vallance Jones, 1974, p45) which show the mean height of lower borders of auroral arcs decreasing from 114 km for weak aurorae to 95 km for very strong aurorae.

Tidal and solar-cycle effects on the λ558 nm airglow intensity (Takahashi et al, 1984) may also be important, but their relevence is not clear.

The height of the gravity wave source region may vary with geomagnetic activity.

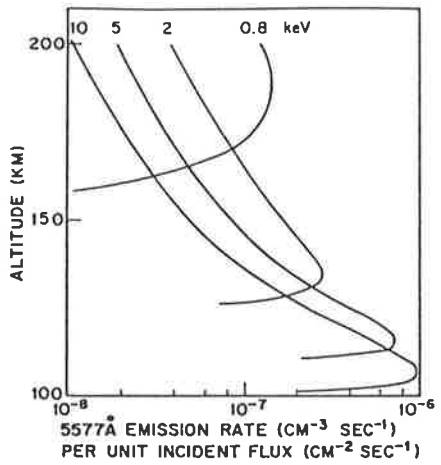

Figure 6.12. Computed profiles of the λ558 nm emission, showing a decrease in height of maximum emission as the energy of the Gaussian (monoenergetic) electron spectrum increases (from Banks et al., 1974).

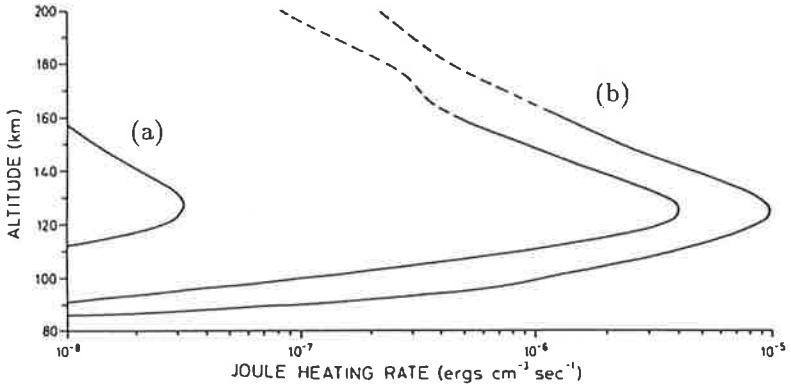

Figure 6.13. Altitude profiles of Joule heating rate obtained from electron density measurements during periods of (a) small and (b) large variations in the geomagnetic H component (adapted from Banks, 1977).

Thiele et al. (1981) obtained altitude profiles of Pederson conductivity under different geophysical conditions. The altitude of maximum conductivity varied from 120 km (no electrojet activity) to 136 km (-450 nT negative bay). They suggested that since the amount of Joule heating is determined by the Pederson conductivity, the altitude of maximum Joule heating increases with Pederson conductivity (that is, increasing E-layer ionisation). However, calculations of Joule heating using data from the Chatanika incoherent-scatter radar (Banks, 1977) showed only a small change in the altitude of maximum heating (125-130 km) from periods of zero to large variations in the geomagnetic H component (figure 6.13).

The discussion above indicates that the general effect of increased geomagnetic activity is a decrease in the height of the λ558 nm emission layer, and either no change, or some increase in the height of the source region, ie. a net increase in separation of the λ558 nm

emission and source regions. Therefore, if the altitudes of the λ558 nm emission layer and the source region are closest during periods of low geomagnetic activity, an increase in the observed number of 'thermospheric' waves might be expected in the low A_p category. This is what is observed (figure 6.5) - the λ558 nm distributions for moderate and high A_p are characteristic of 'tropospheric' waves, but the distributions for low A_p shows distinct gg. northwest and southeast lobes characteristic of 'thermospheric' waves.

The same argument indicates a net decrease in the separation of the λ630 nm emission layer and the auroral source region during high geomagnetic activity. The λ630 nm distributions show a small increase in the number of waves propagating south-eastward during high A_p . This may not be significant, but it is consistent with the model - if there is a net decrease in the separation of the λ630 nm emission layer and the source region with high A_p , south-eastward propagating waves may be able to reach the emission layer before passing over Mawson.

No marked changes with A_p are evident in the corresponding distributions for high solar activity.

The arguments above rely rather heavily on the relative altitude of the gravity-wave source region and the emission regions at which they are observed, and their changes with geomagnetic activity. Unfortunately, no further supportive evidence can be offered, as simultaneous measurements of these parameters are scarce. However, Brekke and Rino (1978) suggested that the altitude of the westward electrojet is 10 km lower than that of the eastward electrojet (at 130 km) during its most intense period. Therefore the corresponding Joule heating regions will be separated in height. A higher time-resolved analysis of the data from 1984 to 1987, as mentioned earlier, may show a change in waves propagation azimuth (in the λ558 nm emission) as Mawson moves from under the eastward to the westward electrojet.

The model also relies on an increased reflection of 'tropospheric' waves during periods of high solar activity. Until these assumptions can be confirmed or rejected, this interpretation of the data can only be speculative.

Chapter 7

Conclusions and Suggestions for Further Work

Observations of nighttime intensity variations in the $O(^1D)$ λ630 nm and $O(^1S)$ λ558 nm thermospheric emissions recorded by the author in 1987, have been analysed using the cross-spectral technique to extract information on periodic structure in the data. Periodicities satisfying certain criteria were attributed to propagating gravity waves. Periods, speeds, and wavelengths evaluated from the λ630 nm data were characteristic of large-scale waves, and those evaluated from the λ558 nm data were characteristic of medium-scale waves. They showed a similar spread of scales when compared with data collated from other observations in the F, E and D regions.

Data from 1982 to 1989 were also examined. Period and speed distributions showed no significant variation from year to year, and the propagation azimuths of waves in the λ630 nm emission were consistently polarised towards the northwest quadrant. It was suggested that the majority of these waves were generated in the auroral electrojet, propagating away equatorward and poleward. The propagation azimuths of waves in the λ558 nm emission varied in a manner indicative of a solar-cycle dependency. λ558 nm data from all years were grouped according to F10.7 cm and A_p indices. The interpretation of the resulting azimuth distributions was that the source of most waves observed in the λ558 nm emission during low solar activity is tropospheric, whereas during high solar activity, it is thermospheric, presumed to be the auroral electrojet. Variation in the azimuth distributions was discussed in terms of variation of the relative heights of the λ558 nm emission layer and the auroral electrojet.

In order to assess the interpretation put forward in Chapter 6, waves must be reverse-ray-traced from the λ630 nm emission height to the lower thermosphere, and possibly to the troposphere, and from the λ558 nm emission height to the troposphere. If wind shears associated with the katabatic wind are producing waves which propagate to the thermosphere, reverse ray tracing will not necessarily locate any particular source region, as katabatic winds are present throughout much of east Antarctica (Schwerdtfeger, 1984). However, it may confirm that waves are able to penetrate the middle atmosphere without reflection and critical level absorption, and may give some indication of their propagation azimuths immediately after generation. One might expect that ray tracing from the λ630 nm emission height to the approximate height of the auroral electrojet may show a preponderance of possible launching points in the auroral zone. Attempts to trace waves in the λ558 nm emission to an auroral source would not be useful because of the uncertainty in the relative heights of the λ558 nm emission layer and the auroral electrojet.

The amount of data available is sufficient to obtain a statistically significant result; the difficulty lies with obtaining information on wind fields in the region of the ray paths. Winds have a significant effect, not only by changing the value of the intrinsic wave parameters (possibly causing reflection or critical level absorption), but also by advecting the wave packet, and in strong horizontal shears, by refracting the wavefronts. This latter effect may be important in Antarctica, with the circumpolar vortex in the middle atmosphere, and magnetospherically-driven convection cells in the thermosphere.

Observational wind data for southern high latitudes is scarce, and since good spatial coverage is required in this situation, an appropriate wind model is necessary. The UCL model of Rees and Fuller-Rowell (1988) covers altitudes from around 90 km to the exosphere, and shows general agreement in large scale features, with wind observations at Mawson (Conde, 1990). Fleming et al. (1988) presented a mean climatology from 0 to 120 km (to be used in the next COSPAR reference atmosphere) which may be used in tracing waves to the troposphere.

Frequent observations of seasonal and diurnal variations in gravity wave activity sug-

gest that the current project could be profitably extended in this direction. Summer observations of the oxygen emissions are not technically possible with the photometer, but the maximum observing period has been extended, so that longer coverage (up to 17 h) is possible over winter. The analysis should be extended to allow dynamic spectral analysis (rather than a single spectral analysis of a whole night's data). This would show the development of waves throughout the night, and may give some indication of diurnal trends. For example, a change in the distribution of propagation azimuth during the night may indicate a localised source region in the auroral electrojet, whose relative position changes as the station rotates past the source region. Alternatively, it may indicate a diurnal filtering effect caused by diurnal wind changes.

The photometer is currently operating in the configuration described in Chapter 3, with the addition of two filters having peak transmission at λ589.1 nm, intended for observation of the sodium doublet, and at λ601.8 nm, intended for observation of nearby aurorally-excited spectral features. It is anticipated that contributions from the sodium airglow emission in the records from the first filter, may be isolated by suitable manipulation of the two sets of records. The problem of 'suitable manipulation' is by no means straightforward; however, if this is accomplished, any variations in the intensity of the sodium emission may then be analysed for wave motions.

Sodium airglow originates from a height region centred on 85 to 90 km, so that analysis of this sort may provide useful information by showing whether the waves attributed to tropospheric sources in this work appear in the sodium emission as expected, particularly during periods of high solar activity, when the mesopause region appears to reflect such waves (according to the model discussed herein). Further, if the wave activity in the sodium and λ558 nm emissions appear to be related, it may be possible to evaluate vertical wave numbers, allowing an independent test of the applicability of the gravity wave dispersion relation to the observations.

Bibliography

Abreu, V.J., Yee, J.H, Solomon, S.C., and Dalgarno, A. (1986). The quenching rate of $O(^1D)$ by $O(^3P)$. *Planetary and Space Science* **11**:1143

Ahn, B-H., Kroehl, H.W., Kamide, Y., Gorney, D.G., Akasofu, S-I., and Kan, J.R. (1989). The auroral energy deposition over the polar ionosphere during substorms. *Planetary and Space Science* **37**:239-252

Akasofu, S-I. (1978). Recent progress in Antarctic auroral studies. *AGU Antarctic Research Series* **29**:157-199

Andrews, D.G., Holton, J.R., and Leovy, C.B. (1987). Middle atmosphere dynamics. Academic Press, Orlando, Florida.

Armstrong, E.B. (1982). The association of visible airglow features with a gravity wave. *Journal of Atmospheric and Terrestrial Physics* **44**:325-336

Balsley, B.B. and Carter, D.A. (1989). Mountain waves in the tropical Pacific atmosphere: A comparison of vertical wind fluctuations over Pohnpei and Christmas Island. *Journal of the Atmospheric Sciences* **46**:2698-2715

Banks, P.M. (1977). Observations of Joule and particle heating in the auroral zone. *Journal of Atmospheric and Terrestrial Physics* **39**:179-193

Banks, P.M., Chappell, C.R., and Nagy, A.F. (1974). A new model for the interaction of auroral electrons with the atmosphere: Spectral degradation, backscatter, optical emission, and ionization. *Journal of Geophysical Research* **79**:1459-1470

Båth, M. (1974). Spectral analysis in geophysics. Elsevier Scientific Pub. Co., Amsterdam

Beer, T. (1974). Atmospheric waves. Adam Hilger Ltd, London

Bendat, J.S. and Piersol A.G. (1971). Random data: analysis and measurement procedures. John Wiley & Sons, New York

Bertin, F., Testud, J., Kersley, l. (1975). Medium-scale gravity waves in the ionospheric F-region and their possible origin in weather disturbances. *Planetary and Space Science* **23**:493-507

Bertin, F., Kofman, W., Lejeune, G. (1983). Observations of gravity waves in the auroral zone. *Radio Science* **18**:1059-1065

Bevington, P.R. (1969). Data reduction and error analysis for the physical sciences. McGraw-Hill Book Co., New York

Beynon, W.J.G. (1948). Evidence of horizontal motion in region F_2 ionization. *Nature* **162**:887

Blumen, W. and Hart, J.E. (1988). Airborne Doppler lidar wind measurements of waves in the lee of Mt Shasta. *Journal of the Atmospheric Sciences* **45**:1571-1583

Bond, F.R. and Jacka, F. (1960). Distribution of auroras in the southern hemisphere. *Australian Journal of Physics* **13**:610-612

Bond, F.R. and Jacka, F. (1962). Distribution of auroras in the southern hemisphere. II. Nightly probability of overhead aurora. *Australian Journal of Physics* **15**:261-272

Booker, J.R. and Bretherton, F.P. (1967). The critical layer for internal gravity waves in a shear flow. *Journal of Fluid Mechanics* **27**:513-539

Born, M. and Wolf, E. (1970). Principles of optics. Permagon Press, Oxford.

Bracewell, R.N. (1978). The Fourier transform and its applications. McGraw-Hill Book Co., Tokyo

Brekke, A. (1979). On the relative importance of Joule heating and the Lorentz force in generating gravity waves and infrasound waves in the auroral electrojets. *Journal of Atmospheric and Terrestrial Physics* **41**:475-479

Brekke, A. and Rino, C.L. (1978). High-resolution altitude profiles of the auroral zone energy dissipation due to ionospheric currents. *Journal of Geophysical Research* **83**:2517-2524

Bretherton, F.P. (1966). The propagation of internal waves in a shear flow. *Quarterly Journal of the Royal Meteorological Society* **92**:466-480

Chamberlain, J.W. (1961). Physics of the aurora and airglow. Academic Press, New York

Chan, K.L. and Villard, O.G. (1962). Observations of large-scale traveling ionospheric disturbances by spaced-path high-frequency instantaneous-frequency measurements. *Journal of Geophysical Research* **67**:973-988

Chandra, S., Krankowsky, K., Lämmerzahl, P., and Spencer, N.W. (1979). Auroral origin of medium scale gravity waves in neutral composition and temperature. *Journal of Geophysical Research* **84**:1891-1897

Chimonas, G. and Hines, C.O. (1970). Atmospheric gravity waves launched by auroral currents. *Planetary and Space Science* **18**:565-582

Clairemidi, J., Hersé, M., and Moreels, G. (1985). Bi-dimensional observations of waves near the mesopause at auroral latitudes. *Planetary and Space Science* **33**:1013-1022

Clark, T.L. and Peltier, W.R. (1984). Critical level reflection and the resonant growth of nonlinear mountain waves. *Journal of the Atmospheric Sciences* **41**:3122-3134

Cogger, L.L., Elphinstone, R.D., and Giers, D.H. (1988). Wave characteristics obtained from OH rotational temperatures and λ557.7 nm airglow intensities. *Journal of Atmospheric and Terrestrial Physics* **50**:943-949

Conde, M.G. (1990). Spectroscopic observations of the λ630 nm thermospheric emission from Mawson, Antarctica, under daylight, twilight and night-time observing conditions. Ph.D. Thesis to be submitted. Adelaide University.

Cowling, D.H., Webb, H.D., and Yeh, K.C. (1971). Group rays of internal gravity waves in a wind-stratified atmosphere. *Journal of Geophysical Research* **76**:213-220

Crowley, G., Jones, T.B., and Dudeney, J.R. (1987). Comparison of short period TID morphologies in Antarctica during geomagnetically quiet and active intervals. *Journal of Atmospheric and Terrestrial Physics* **49**:1155-1162

Crowley, G. and Williams, P.J.S. (1987). Observations of the source and propagation of atmospheric gravity waves. *Nature* **328**:231-233

Dartt, D., Nastrom, G., and Belmont, A. (1983). Seasonal and solar cycle wind variations, 80-100 km. *Journal of Atmospheric and Terrestrial Physics* **45**:707-718

Davies, K. and Baker, D.M. (1965). Ionospheric effects observed around the time of the Alaskan earthquake. *Journal of Geophysical Research* **70**:2251-2253

Davies, K. and Jones, J.E. (1971). Three dimensional observations of travelling ionospheric disturbances. *Journal of Atmospheric and Terrestrial Physics* **33**:39-46

Davis, M.J. and DaRosa, A.V. (1969). Travelling ionospheric disturbances originating in the auroral oval during polar substorms. *Journal of Geophysical Research* **74**:5721-5735

Davis, M.J. and DaRosa, A.V. (1970). Possible detection of atmospheric gravity waves generated by the solar eclipse. *Nature* **226**:1123

Eather, R.H. and Reasoner, D.L. (1969). Spectrophotometry of faint light sources with a tilting-filter photometer. *Applied Optics* **8**:227-242

Ebel, A., Manson, A.H., and Meek, C.E. (1987). Short period fluctuations of the horizontal wind measured in the upper middle atmosphere and possible relationships to internal gravity waves. *Journal of Atmospheric and Terrestrial Physics* **49**:385-401

Elkins, T.J. and Slack, F.F. (1969). Observations of traveling ionospheric disturbances using stationary satellites. *Journal of Atmospheric and Terrestrial Physics* **31**:421-439

Evans, J.V., Holt, J.M., and Wand, R.H. (1983). A differential-Doppler study of traveling ionospheric disturbances from Millstone Hill. *Radio Science* **18**:435-451

Fleming, E.L., Chandra, S., Schoeberl, M.R., and Barnett, J.J. (1988). Monthly mean global climatology of temperature, wind, geopotential height, and pressure for 0-120 km. *NASA Technical Memorandum 100697*

Forsyth, R.J. and Wraight, P.C. (1987). A survey of research on nightglow variability. *Planetary and Space Science* **35**:1449-1461

Francis, S.H. (1974). A theory of medium-scale traveling ionospheric disturbances. *Journal of Geophysical Research* **79**:5245-5260

Francis, S.H. (1975). Global propagation of atmospheric gravity waves: A review. *Journal of Atmospheric and Terrestrial Physics* **37**:1011-1054

Freund, J.T. and Jacka, F. (1979). Structure in the λ557.7 nm [OI] airglow. *Journal of Atmospheric and Terrestrial Physics* **41**:25-31

Fritts, D.C. (1984). Gravity wave saturation in the middle atmosphere: A review of theory and observations. *Reviews of Geophysics and Space Physics* **22**:275

Fritts, D.C. (1985). A numerical study of gravity wave saturation: Non-linear and multiple wave effects. *Journal of the Atmospheric Sciences* **42**:2043-2058

Fritts, D.C. (1989). A review of gravity wave saturation processes, effects, and variability in the middle atmosphere. *Pure and Applied Geophysics* **130**:343-371

Fritts, D.C., and Rastogi, R.K. (1985). Convective and dynamical instabilities due to gravity wave motions in the lower and middle atmosphere: Theory and observations. *Radio Science* **20**:1247-1277

Gattinger, R.L., Harris, F.R., and Vallance Jones, A. (1985). The height, spectrum and mechanism of the type-B red aurora and its bearing on the excitation of $O(^1S)$ in aurora. *Planetary and Space Science* **33**:207-221

Gavrilov, N.M. and Shved, G.M. (1982). Study of internal gravity waves in the lower thermosphere from observations of the nocturnal sky airglow [OI] λ557.7 nm in Ashkhabad. *Annales de Geophysique* **38**:789-803

Gavrilov, N.M., Karmov, K.A., Mordvintsev, M.Y., and Semenov, V.K (1978). *Geomagnetism and Aeronomy* **18**:248

Georges, T.M. (1967a). Evidence for the influence of atmospheric waves on ionospheric motions. *Journal of Geophysical Research* **72**:422-425

Georges, T.M. (1967b). Ionospheric effects of atmospheric waves. ESSA technical report IER 57 - ISTA 54, US Government Printing Office, Washington DC.

Georges, T.M. (1968). HF Doppler studies of traveling ionospheric disturbances. *Journal of Atmospheric and Terrestrial Physics* **30**:735-746

Gerdjikova, M.G. and Shepherd, G.G. (1987). Evaluation of auroral λ557.7 nm excitation processes using Intercosmos Bulgaria 1300 satellite measurements. *Journal of Geophysical Research* **92**:3367-3374

Gossard, E.E. (1962). Vertical flux of energy into the lower ionosphere from internal gravity waves generated in the troposphere. *Journal of Geophysical Research* **67**:745-757

Gossard, E.E. and Hooke, W.H. (1975). Waves in the atmosphere. Elsevier Scientific Publ. Co., Amsterdam

Greenhow, J.S. and Neufeld, E.L. (1959). Measurement of turbulence in the 80 to 100 km region from the radio echo observations of meteors. *Journal of Geophysical Research* **64**:2129-2133

Groves, G.V. (1985). A global reference atmosphere from 18 to 80 km. Technical Report AFGL-TR-85-0129. Air Force Geophysics. Hascom Air Force Base. Massachusetts.

Groves, G.V. (1987). Modeling of atmospheric structure. Technical Report AFGL-TR-87-0226. Air Force Geophysics. Hascom Air Force Base. Massachusetts.

Gulledge, I.S., Packer, D.M., Tilford, S.G., and Vanderslice, J.T. (1968). Intensity profiles of the 6300 Å and 5577 Å OI lines in the night airglow. *Journal of Geophysical Research* **73**:5535-5545

Hajkowicz, L.A. and Hunsucker, R.D. (1987). A simultaneous observation of large scale periodic TIDs in both hemispheres following an onset of auroral disturbances. *Planetary and Space Science* **35**:785-791

Hardy, D.A., Gussenhoven, M.S., and Holeman, E. (1985). A statistical model of auroral electron precipitation. *Journal of Geophysical Research* **90**:4229-4248

Hays, P.B., Rusch, D.W., Roble, R.G., and Walker, J.C.G. (1978). The *OI* (6300 Å) airglow. *Reviews of Geophysics and Space Physics* **16**:225-232

Hedin, A.E. (1988). The atmospheric model in the region 90 to 2000 km. *Advances in Space Research* **8**:9-26

Heisler, L.H. (1958). Anomalies ionosonde records due to travelling ionospheric disturbances. *Australian Journal of Physics* **11**:79-90

Henriksen, K. and Egeland, A. (1988). The interpretation of the auroral green line: A historic preamble and the present state of knowledge. *EOS* **69**:721

Hickey, M.P. and Cole, K.D. (1988). A numerical model for gravity wave dissipation in the thermosphere. *Journal of Atmospheric and Terrestrial Physics* **50**:689-697

Hines, C.O. (1955). Hydromagnetic resonance in ionospheric waves. *Journal of Atmospheric and Terrestrial Physics* **7**:14-30

Hines, C.O. (1959). An interpretation of certain ionospheric motions in terms of atmospheric waves. *Journal of Geophysical Research* **64**:2210-2211

Hines, C.O. (1960). Internal atmospheric gravity waves at ionospheric heights. *Canadian Journal of Physics* **38**:1441-1481

Hines, C.O. (1967). On the nature of traveling ionospheric disturbances launched by low-altitude nuclear explosions. *Journal of Geophysical Research* **72**:1877-1882

Hines, C.O. (1968). Some consequences of gravity wave critical layers in the upper atmosphere. *Journal of Atmospheric and Terrestrial Physics* **30**:837-843

Hines, C.O. (1974). Propagation velocities and speeds in ionospheric waves: A review. *Journal of Atmospheric and Terrestrial Physics* **36**:1179-1204

Hines, C.O. and Hooke, W.H. (1970). Discussion of ionisation effects on the propagation of acoustic-gravity waves in the ionosphere. *Journal of Geophysical Research* **75**:2563-2568

Hines, C.O. and Reddy, C.A. (1967). On the propagation of atmospheric gravity waves through regions of wind shear. *Journal of Geophysical Research* **72**:1015-1034

Hines, C.O. and Tarasick, D.W. (1987). On the detection and utilization of gravity waves in airglow studies. *Planetary and Space Science* **35**:851-866

Hines, C.O. and Colleagues (1974). The upper atmosphere in motion. A selection of papers with annotation. American Geophysical Union, Washington.

Hodges, J.R. (1967). Generation of turbulence in the upper atmosphere by internal gravity waves. *Journal of Geophysical Research* **72**:3455-3458

Hodges, J.R. (1969). Eddy diffusion coefficients due to instabilities in internal gravity waves. *Journal of Geophysical Research* **74**:4087-4090

Hooke, W.H. and Hardy, K.R. (1975). Further study of the atmospheric gravity waves over the eastern seabord on 18 March 1969. *Journal of Applied Meteorology* **14**:31-38

Hunsucker, R.D. (1977). Estimate of the relative importance of Joule heating and the Lorentz force in generating atmospheric gravity waves from the auroral electrojet. *Journal of Geophysical Research* **82**:4826-4829

Hunsucker, R.D. (1982). Atmospheric gravity waves generated in the high-latitude ionosphere - A review. *Reviews of Geophysics and Space Physics* **20**:293-315

Hunsucker, R.D. and Tveten, L.H. (1967). Large traveling ionospheric disturbances observed at midlatitudes utilizing the high resolution HF backscatter technique. *Journal of Atmospheric and Terrestrial Physics* **29**:909-916

Ismail, S. and Cogger, L.L. (1982). Temporal variations of polar cap OI 5577 Å airglow. *Planetary and Space Science* **30**:865-873

Jacka, F. (1984). Application of Fabry-Perot spectrometers for measurement of upper atmosphere temperatures and winds. *Middle Atmosphere Program Handbook* **13**:19-40

Jacob, P. (1985). Manifestations of atmospheric gravity waves in the airglow at 95 km. Ph.D. thesis, University of Adelaide.

Jenkins, G.M. and Watts, D.G. (1969). Spectral analysis and its applications. Holden Day, San Francisco.

Jones, N. and Jacka, F. (1987). Dynamics of the thermosphere over Mawson, Antarctica. IV. The lower thermosphere. *ANARE Research Notes* **48**:138-147

Kellog, W.W. and Schilling, G.F. (1951). A proposed model of the circulation in the upper stratosphere. *Journal of Meteorology* **8**:222-230

Knudsen, W.C. (1969). Neutral atmosphere wave generation by the auroral electrojet. *Journal of Geophysical Research* **74**:4191-4192

Kochanski, A. (1964). Atmospheric motions from sodium cloud drifts. *Journal of Geophysical Research* **69**:3651-3662

Koop, C.G. (1981). A preliminary investigation of internal gravity waves with a steady shearing motion. *Journal of Fluid Mechanics* **113**:347-386

Koop, C.G. and McGee, B. (1986). Measurements of internal gravity waves in a continuously stratified shear flow. *Journal of Fluid Mechanics* **172**:453-480

Krassovsky, V.I., Potapov, B.P., Semenov, A.I., Shagaev, M.V., Shefov, N.N., Sobolev, V.G., and Toroshelidze, T.I. (1977). Internal gravity waves near the mesopause and the hydroxyl emission. *Annales de Geophysique* **33**:347-356

Lamb, H. (1945). Hydrodynamics. New York Dover Publications

Lighthill, J. (1978). Waves in fluids. Cambridge University Press, Cambridge

Liller, W. and Whipple, F.L. (1954). High altitude winds by meteor train photography. From Rocket exploration of the upper atmosphere. *A special supplement to Journal of Atmospheric and Terrestrial Physics* **1**:112-130

Lindzen, R.S. (1981). Turbulence and stress owing to gravity wave and tidal breakdown. *Journal of Geophysical Research* **86**:9707-9714

Luhmann, J.G. (1980). Atmospheric pressure and velocity fluctuations near the auroral electrojet. *Journal of Geophysical Research* **85**:1749-1756

Manring, E., Bedinger, J.F., Pettit, and Moore, C.B. (1959). Some wind determinations in the upper atmosphere using artificially generated sodium clouds. *Journal of Geophysical Research* **64**:587-591

Manson, A.H. and Meek, C.E. (1988). Gravity wave propagation characteristics (60-120 km) as determined by the Saskatoon MF radar (Gravnet) system: 1983-85 at 52°N, 107°W. *Journal of the Atmospheric Sciences* **45**:932-946

Manson, A.H., Meek, C.E., Massebeuf, M., Fellous, J.L., Elford, W.G., Vincent, R.A., Craig, R.L., Roper, R.G., Avery, S., Balsley, B.B., Fraser, G.J., Smith, M.J., Clarke, R.R, Kato, S., Tsuda, T., and Ebel, A. (1985). Mean winds of the upper middle atmosphere (60-110 km); A global distribution from radar systems (MF, meteor, VHF) *Middle Atmosphere Program Handbook* **16**:239-268

Martyn, D.F. (1950). Cellular atmospheric waves in the ionosphere and troposphere. *Proceedings of the Royal Society, London* **A201**:216-233

Mayr, H.G., Harris, I., Varosi, F., and Herrero, F.A. (1984). Global excitation of wave phenomena in a dissipative multiconstituent medium. 1. Transfer function of the earth's thermosphere. *Journal of Geophysical Research* **89**:10 929-10 959

McEwan, M.J. and Phillips, L.F. (1975). Chemistry of the atmosphere. Edward Arnold Ltd. London.

McIntyre, M.E. and Weissman, M.A. (1978). On radiating instabilities and resonant overreflection. *Journal of the Atmospheric Sciences* **35**:1190-1196

Meek, C.E. and Manson, A.H. (1983). Measurements of the structure and drift velocities of airglow (λ557.7 nm) irregularities: Saskatoon (52°N, 107°W), Canada. *Journal of Atmospheric and Terrestrial Physics* **45**:203-212

Meek, C.E., Reid, I.M., and Manson, A.H. (1985). Observations of mesospheric wind velocities 1. Gravity wave horizontal scales and phase velocities determined from spaced wind observations. *Radio Science* **20**:1363-1382

Meier, R.R. (1987). Thermospheric aurora and airglow. *Reviews of Geophysics* **25**:471-477

Mercier, C. (1986). Observations of atmospheric gravity waves by radio-interferometry. *Journal of Atmospheric and Terrestrial Physics* **48**:605-624

Meriwether, J.W. (1979). Measurement of weak airglow emissions with a programmable scanning spectrometer. *Planetary and Space Science* **27**:1221-1232

Midgeley, J.E. and Liemohn, H.B. (1966). Gravity waves in a realistic atmosphere. *Journal of Geophysical Research* **71**:3729-3748

Minzer, R.A., Champion, K.S.W., and Pond, H.L. (1959). The ARDC model atmosphere, 1959. Air Force Surveys in Geophysics No. 115. Air Force Cambridge Research Center. Massachusetts.

Misawa, K. and Takeuchi, I. (1977). Ground observation of the O_2 $(0-1)$ atmospheric band at 8645 Å and the $[OI]$ 5577 Å line. *Journal of Geophysical Research* **82**:2410-2412

Misawa, K., Takeuchi, I., Kato, Y., and Aoyama, I. (1984). Generation of intensity covariations of the oxygen green and red lines in the nightglow. *Annales Geophysicae* **2**:77-82

Mohanakumar, K. (1985). An investigation on the influence of solar cycle on mesospheric temperature. *Planetary and Space Science* **33**:795-805

Moreels, G. and Herse, M. (1977). Photographic evidence of waves around the 85 km level. *Planetary and Space Science* **25**:265-273

Mullen, E.G., Silverman, S.M., and Korff, D.F. (1977). Nightglow (557.7 nm of OI) in the central polar cap. *Planetary and Space Science* **25**:23-38

Munro, G.H. (1948). Short period changes in the F region of the ionosphere. *Nature* **162**:886-887

Munro, G.H. (1950). Travelling disturbances in the ionosphere. *Proceedings of the Royal Society* **A202**:208

Munro, G.H. (1958). Travelling ionospheric disturbances in the F region. *Australian Journal of Physics* **11**:91-112

Myrabø, H.K., Deehr, C.S., Viereck, R., and Henrikson, K. (1987). Polar mesopause gravity wave activity in the sodium and hydroxyl night airglow. *Journal of Geophysical Research* **92**:2527-2534

Nakamura, R. and Oguti, T. (1987). Drifts of auroral structures and magnetospheric electric fields. *Journal of Geophysical Research* **92**:11,241-11,247

Newton, G.P., Pelz, D.T., and Volland, H. (1969). Direct in situ measurements of wave propagation in the neutral atmosphere. *Journal of Geophysical Research* **74**:183-196

Ogawa, T., Igarashi, K., Aikyo, K., and Maeno, H. (1987). NNSS satellite observations of medium-scale traveling ionospheric disturbances at southern high-latitudes. *Journal of Geomagnetism and Geoelectricity* **39**:709-721

Parkinson, T.D. and Zipf, E.C. (1970). Energy transfer from $N_2(A^3\Sigma_\mu^+)$ as a source of $O(^1S)$ in the aurora. *Planetary and Space Science* **18**:895-900

Phillips, A. and Vincent, R.A. (1987). Winds in the middle atmosphere at Mawson, Antarctica: II. Tides. *ANARE Research Notes* **48**:93-106

Pitteway, M.L.V. and Hines, C.O. (1963). The viscous damping of atmospheric gravity waves. *Canadian Journal of Physics* **41**:1935-1948

Pitteway, M.L.V. and Hines, C.O. (1965). The reflection and ducting of atmospheric acoustic-gravity waves. *Canadian Journal of Physics* **43**:2222-2243

Potter, W.E., Kayser, D.C., and Mauersberger, K. (1976). Direct measurements of neutral wave characteristics in the thermosphere. *Journal of Geophysical Research* **81**:5002-5012

Reed, R.J. and Hardy, K.R. (1972). A case study of persistent, intense, clear air turbulence in an upper level frontal zone. *Journal of Applied Meteorology* **11**:541-549

Rees, D. and Fuller-Rowell, T.J. (1988). The CIRA theoretical thermosphere model. *Advances in Space Research* **8**:27-106

Rees, M.H. (1984). Excitation of $O(^1S)$ and emission of 5577 Å radiation in aurorae. *Planetary and Space Science* **32**:373-378

Rees, M.H. and Roble, R.G. (1986). Excitation of $O(^1D)$ atoms in aurorae and emission of the [OI] 6300-Å line. *Canadian Journal of Physics* **64**:1608-1613

Reid, I.M. (1986). Gravity wave motions in the upper middle atmosphere (60-110 km). *Journal of Atmospheric and Terrestrial Physics* **48**:1057-1072

Richmond, A.D. (1978a). The nature of gravity wave ducting in the thermosphere. *Journal of Geophysical Research* **83**:1385-1389

Richmond, A.D. (1978b). Gravity wave generation, propagation and dissipation in the thermosphere. *Journal of Geophysical Research* **83**:4131-4145

Richmond, A.D. and Matsushita, S. (1975). Thermospheric response to a magnetic substorm. *Journal of Geophysical Research* **80**:2839-2850

Rosenberg, N.W. and Edwards, H.D. (1964). Observations of ionospheric wind patterns through the night. *Journal of Geophysical Research* **69**:2819-2826

Schoeberl, M.R. (1985). The penetration of mountain waves into the middle atmosphere. *Journal of the Atmospheric Sciences* **42**:2856-2864

Schwerdtfeger, W. (1984). Weather and climate of the Antarctic. Elsevier, New York.

Scmidtke, G., Stasek, G., Wita, C., Seidl, P., and Baker, K.D. (1985). Rocket-borne EUV-visible emission measurements. *Journal of Atmospheric and Terrestrial Physics* **47**:147-158

Sharp, W.E., Rees, M.H., and Stewart, A.I. (1979). Coordinated rocket and satellite measurements of an auroral event. 2. The rocket observations and analysis. *Journal of Geophysical Research* **84**:1977-1985

Sharp, W.E., Ortland, D., and Cageao, R. (1983). Concerning sources of $O(^1D)$ in aurora: Electron impact and dissociative recombination. *Journal of Geophysical Research* **88**:3229-3232

Singleton, R.C. (1969). An algorithm for computing the mixed radix fast Fourier transform. *IEEE Transactions* **3**:1969

Sinno, K., Ouchi, C., and Nemoto, C. (1964). Structure and movement of E_s detected by Loran observations. *Journal of the Radio Research Laboratories, Japan* **11**:45-61

Solomon, S.C., Hays, P., and Abreu, V.J. (1988). The auroral 6300 Å emission: Observations and modelling. *Journal of Geophysical Research* **93**:9867-9882

Somsikov, V.M. (1987). A spherical model of wave generation in the atmosphere by the solar terminator. *Journal of Atmospheric and Terrestrial Physics* **49**:433-438

Störmer, C. (1955). The polar aurora. Clarendon Press, Oxford.

Streten, N.A. (1963). Some observations of Antarctic katabatic winds. *Australian Meteorological Magazine* **42**:1-23

Streten, N.A. (1990). A review of the climate of Mawson - a representative strong wind site in east Antarctica. *Antarctic Science* **2**:79-89

Takahashi, H., Batista, P.P, Sahai, Y., and Clemesha, B.R. (1985). Atmospheric wave propagation in the mesopause region observed by the $OH(8,3)$ band, $Na\ D$, $O_2\ A(8645\ \mathring{A})$ band and OI 5577 Å nightglow emissions. *Planetary and Space Science* **33**:381-384

Takahashi, H., Sahai, Y., Batista, P.P. (1984). Tidal and solar cycle effects on the OI λ557.7 nm, NaD, and OH(8,3) airglow emissions observed at 23°S. *Planetary and Space Science* **32**:897-902

Taylor, M.J. and Hapgood, M.A. (1988). Identification of a thunderstorm as a source of short period gravity waves in the upper atmospheric nightglow emissions. *Planetary and Space Science* **36**:975-985

Tedd, B.L. and Morgan, M.G. (1985). TID observations at spaced geographic locations. *Journal of Geophysical Research* **90**:12 307-12 319

Testud, J. (1970). Gravity waves generated during magnetic substorms. *Journal of Atmospheric and Terrestrial Physics* **32**:1793-1805

Thiele, B., Boström, R., Dumbs, A., Grossmann, K.U., Kranowsky, D., Lämmerzahl, P., Marklund, G., Neske, E., Schmidkte, G., Wilhelm, K. (1981). In situ measurements of heating parameters in the auroral electrojet. *Planetary and Space Science* **29**:455-468

Thomas, L., Greer, R.G.H., and Dickinson, P.H.G. (1979). The excitation of the λ557.7 nm line and Herzberg bands in the nightglow. *Planetary and Space Science* **27**:925-931

Thomas, R.J. (1981). Analyses of atomic oxygen, the green lines, and Herzberg bands in the lower thermosphere. *Journal of Geophysical Research* **86**:206-210

Torr, M.R. and Torr, D.G. (1982). The role of metastable species in the thermosphere. *Reviews of Geophysics and Space Physics* **20**:91-144

US Standard Atmosphere, 1976. US Government Printer. Washington

Vallance Jones, A. (1974). Aurora. D. Reidel Publ. Co., Dordrecht.

Vallance Jones, A., Meier, R.R., and Shefov, N.N. (1985). Atmospheric quantal emissions: A review of recent results. *Journal of Atmospheric and Terrestrial Physics* **47**:623-642

Viereck, R.A. and Deehr, C.S. (1989). On the interaction between gravity waves and the *OH* Meinel (6-2) and the O_2 atmospheric (0-1) bands in the polar night airglow. *Journal of Geophysical Research* **94**:5397-5404

Vincent, R.A. (1984). Gravity wave motions in the mesosphere. *Journal of Atmospheric and Terrestrial Physics* **46**:119-128

Vincent, R.A. and Fritts, D.C. (1987). A climatology of gravity wave motions in the mesosphere region at Adelaide, Australia. *Journal of the Atmospheric Sciences* **44**:748-760

Vincent, R.A. and Reid, I.M. (1983). HF Doppler measurements of mesospheric gravity wave momentum fluxes. *Journal of the Atmospheric Sciences* **40**:1321-1333

Volland, H. (1969). The upper atmosphere as a multiple refractive medium for neutral air motions. *Journal of Atmospheric and Terrestrial Physics* **31**:491-514

Waldock, J.A. and Jones, T.B. (1987). Source regions of medium scale travelling ionospheric disturbances observed at mid-latitudes. *Journal of Atmospheric and Terrestrial Physics* **49**:105-114

Weinstock, J. (1976). Non-linear theory of acoustic gravity waves 1. Saturation and enhanced diffusion. *Journal of Geophysical Research* **81**:633-652

Weinstock, J. (1978). Theory of the interaction of gravity waves with O_2 airglow. *Journal of Geophysical Research* **83**:5175-5185

Weinstock, J. (1982). Non-linear theory of gravity waves: Momentum deposition, generalized Rayleigh friction, and diffusion. *Journal of the Atmospheric Sciences* **39**:1698-1710

Williams, P.J.S., Crowley, G., Schlegel, K., Virdi, T.S., McCrea, I., Watkins, G., Wade, N., Hargreaves, J.K., Lachlan-Cope, T., Muller, H., Baldwin, J.E., Warner, P., van Eyken, A.P., Hapgood, M.A., and Rodger, A.S. (1988). The generation and propagation of atmospheric gravity waves observed during the Worldwide Atmospheric Gravity-wave Study (WAGS). *Journal of Atmospheric and Terrestrial Physics* **50**:323-338

Witt, G. (1962). Height, structure and displacement of noctilucent clouds. *Tellus* **14**:1

Witt, G., Stegman, J., Solheim, B.H., and Llewellyn, E.J. (1979). A measurement of the O_2 atmospheric band and the OI (^1S) green line in the nightglow. *Planetary and Space Science* **27**:341-350

Zimmerman, S.P. and Champion, K.S.W. (1963). Transport processes in the upper thermosphere. *Journal of Geophysical Research* **68**:3049-3056